

D-6

For  
① Gas dynamics  
② Aerodynamics  
③ Heat transfer  
(wind tunnel)  
④ Reynolds number  
(new data)

SC-4204(TR)  
Special Category - AERODYNAMICS

EXPERIMENTAL PRESSURE DISTRIBUTIONS AND FORCE  
COEFFICIENTS ON BLOCK FORMS FOR VARYING MACH  
NUMBER, REYNOLDS NUMBER, AND YAW ANGLE

by

Dorris M. Hankins, 5112

January 1959

Reproduced From  
Best Available Copy

DISTRIBUTION STATEMENT A  
Approved for Public Release  
Distribution Unlimited

20011015 123

**Sandia Corporation**  
CONTRACTORS FOR U.S. ATOMIC ENERGY COMMISSION

ALBUQUERQUE • NEW MEXICO

Printed in USA. Price \$2.75. Available from the Office of  
Technical Services, Department of Commerce,  
Washington 25, D.C.

#### **LEGAL NOTICE**

This report was prepared as an account of Government sponsored work. Neither the United States, nor the Commission, nor any person acting on behalf of the Commission:

A. Makes any warranty or representation, express or implied, with respect to the accuracy, completeness, or usefulness of the information contained in this report, or that the use of any information, apparatus, method, or process disclosed in this report may not infringe privately owned rights; or

B. Assumes any liabilities with respect to the use of, or for damages resulting from the use of any information, apparatus, method, or process disclosed in this report.

As used in the above, "person acting on behalf of the Commission" includes any employee or contractor of the Commission to the extent that such employee or contractor prepares, handles or distributes, or provides access to, any information pursuant to his employment or contract with the Commission.

SC -4204(TR)  
Special Category - AERODYNAMICS

EXPERIMENTAL PRESSURE DISTRIBUTIONS AND FORCE  
COEFFICIENTS ON BLOCK FORMS FOR VARYING MACH  
NUMBER, REYNOLDS NUMBER, AND YAW ANGLE

by

Dorris M. Hankins, 5112

January 1959

ABSTRACT

Wind tunnel tests were performed to determine pressure distributions and normal force coefficients on three block forms on mounting planes. The dimension ratios of the blocks were 1:1:1, 1:1:2, and 1:1:4. Results are given for variation in Mach number from 0.066 to 0.8, in Reynolds number from  $0.28 \times 10^6$  to  $4 \times 10^6$ , and in yaw angle from 0 to 90 degrees. Results show a Reynolds number independence over the range examined. Windward face force coefficients for a given block form are approximately proportional to the ratio of impact to dynamic pressure. Pressure distribution and resultant coefficients are affected by mounting planes.

## ACKNOWLEDGMENTS

The wind tunnel tests reported herein were designed and performed before the author became affiliated with the project. Credit for this work belongs to L. J. Vortman and B. L. Tucker, Division 5112, who were project engineers for the two test series, and to R. L. Black, Division 5142, who was test engineer for both test series and who coordinated the data reduction.

## TABLE OF CONTENTS

	<u>Page</u>
ABSTRACT	1
ACKNOWLEDGMENTS	2
SYMBOLS	10
CH I -- INTRODUCTION	11
Objectives	11
Theory	11
CH II -- PROCEDURE	13
Cooperative Wind Tunnel Series	13
Models	13
Instrumentation	13
Data	14
University of Wichita Series	14
Models and Instrumentation	14
Data	18
Data Reduction	18
CH III -- RESULTS AND DISCUSSION	21
Accuracy	21
Velocity Profiles	22
Boundary Layer	22
Velocity Distribution	23
General	23
Comparison of Data from Tunnels	24
Reynolds Number Effect	24
Mach Number Effect	25
Compressible Flow Corrections	27

## TABLE OF CONTENTS (cont)

	<u>Page</u>
Effects of Yaw Angle	29
Sample Pressure Distributions	29
Contour Maps	30
Comparison of $C_N$ Versus Yaw Angle for Various Models and Mach Numbers	30
Resultant Force and Drag Coefficients Versus Yaw Angle	32
Comparison of Mounting Effects on the Models in the University of Wichita Tests	33
Depth Effect for 1 x 4 Model	34
Pressure Profiles on Mountings	34
Comparison with Other Experiments	36
Effects of Mounting on Force Coefficients	37
Cube and Prism Tests	38
State University of Iowa Tests on Block Forms	38
Pressure Distribution for a Flat Plate	39
CH IV -- CONCLUSIONS AND RECOMMENDATIONS	41
Conclusions	41
Recommendations	43
APPENDIX	115

## LIST OF ILLUSTRATIONS

	<u>Page</u>
Fig. 1 -- Sketch of mounting plate showing house installations and extension plane	45
Fig. 2 -- Plate with extension ( $H_B$ block installed)	46
Fig. 3 -- Orifice locations on block forms, developed views	47
Fig. 4 -- Surface orifice locations on plate shown with $H_A$ block yawed	48
Fig. 5 -- Ground plane with yawhead installed on disk	49
Fig. 6 -- Surface orifice locations on ground plane shown with $H_A$ block yawed	50
Fig. 7 -- CWT boundary layer profiles on plate mounting	51
Fig. 8 -- Boundary layer profiles in the UW tunnel	52
Fig. 9 -- Mach number distribution forward of CWT plate center without model installed	53
Fig. 10 -- Mach number distribution to the right of CWT plate center without model installed	54
Fig. 11 -- Pressure distribution forward of plate center without model installed in the UW tunnel	55
Fig. 12 -- Pressure distribution on the ground plane forward of center of rotation without model installed in the UW tunnel	55
Fig. 13 -- Comparison of normal force coefficients for $H_C P$ at $M = 0.2$ obtained in two wind tunnels	56
Fig. 14 -- Variations of normal force coefficient with Reynolds number	57
Fig. 15 -- Variation of normal force coefficient with Reynolds number for $H_A P$ at $M = 0.4$ , $\psi = 45^\circ$	57
Fig. 16 -- Normal force coefficient on $H_A$ front face at zero yaw versus Mach number at constant Reynolds number	59
Fig. 17 -- Normal force coefficient on $H_A$ front face at zero yaw versus Mach number for various Reynolds numbers	60

# LIST OF ILLUSTRATIONS (cont)

	<u>Page</u>
Fig. 18 -- Normal force coefficient on square face in the windward direction, $\psi = 90^\circ$	61
Fig. 19 -- Normal force coefficient on $H_B$ front face at zero yaw versus Mach number (various Reynolds numbers)	62
Fig. 20 -- Normal force coefficient on $H_C$ front face at zero yaw versus Mach number (various Reynolds numbers)	63
Fig. 21 -- Variation of $H_{CP}$ front face normal force coefficient with Mach number, yaw angle as a parameter	64
Fig. 22 -- Front face vertical centerline pressure profiles at $M = 0.2$ and $M = 0.8$ , block form as a parameter, Reynolds number is constant, $\psi = 0^\circ$	65
Fig. 23 -- Front face vertical centerline pressure profiles for $H_A$ and $H_C$ , Mach number as a parameter, Reynolds number is constant, $\psi = 0^\circ$	66
Fig. 24 -- Normal force coefficient on back face at zero yaw versus Mach number for all models (mixed Reynolds numbers)	67
Fig. 25 -- Normal force coefficient averaged for left and right ends at zero yaw versus Mach number for $H_A$ and $H_C$ (mixed Reynolds numbers)	68
Fig. 26 -- Normal force coefficient on square face in leeward position, $\psi = 90^\circ$	69
Fig. 27 -- Horizontal centerline pressure distribution on face parallel to wind, for each model at $\psi = 90^\circ$ , Mach number as parameter	70
Fig. 28 -- Resultant force coefficient versus Mach number at zero yaw, block form and mounting as parameters	71
Fig. 29 -- Resultant force coefficient versus Mach number, $\psi = 90^\circ$ , block form as parameter	72
Fig. 30 -- Resultant force coefficient versus Mach number calculated from theoretical impact pressures (based on $M = 0.4$ experimental values), block form as a parameter, $\psi = 0^\circ$	73
Fig. 31 -- Resultant force coefficient versus Mach number calculated from theoretical impact pressures (based on $M = 0.4$ experimental values), block form as a parameter, $\psi = 90^\circ$	74
Fig. 32 -- Normal force coefficient on the front face based on impact pressure versus Mach number, block form with plate mounting as a parameter, $\psi = 0^\circ$	75



# LIST OF ILLUSTRATIONS (cont)

	<u>Page</u>
Fig. 33 -- Vertical and horizontal centerline pressure distributions corrected for compressibility effects on $H_A$ block, Mach number as a parameter	76
Fig. 34 -- Horizontal centerline pressure distribution on $H_A$ block at $M = 0.4$ , yaw angle as a parameter	77
Fig. 35 -- Horizontal centerline pressure distribution on $H_C$ block at $M = 0.4$ , yaw angle as a parameter	78
Fig. 36 -- Variation of panel normal force coefficients with yaw angle for $H_AP$ and $H_CP$ models at $M = 0.4$	79
Fig. 37 -- Variation of panel normal force coefficients with yaw angle for $H_BP$ and $H_CP$ models at $M = 0.4$	80
Fig. 38 -- Variation of panel normal force coefficients with yaw angle for $H_CP$ model at $M = 0.4$ and $M = 0.8$	81
Fig. 39 -- Right angle components of resultant force on $H_AP$ model versus yaw angle for $M = 0.4$	82
Fig. 40 -- Right angle components of resultant force on $H_CP$ model versus yaw angle for $M = 0.4$	83
Fig. 41 -- Right angle components of resultant force on $H_CP$ model versus yaw angle for $M = 0.8$	84
Fig. 42 -- Resultant force coefficient versus yaw angle for $H_AP$ model at $M = 0.4$	85
Fig. 43 -- Moment coefficient versus yaw angle for $H_AP$ model at $M = 0.4$	85
Fig. 44 -- Resultant force coefficient versus yaw angle for $H_CP$ model at $M = 0.4$ and $M = 0.8$	86
Fig. 45 -- Moment coefficient versus yaw angle for $H_CP$ model at $M = 0.4$ and $M = 0.8$	87
Fig. 46 -- Drag coefficient, based on front face area, versus yaw angle for $H_AP$ model at $M = 0.4$	88
Fig. 47 -- Drag coefficient, based on projected windward area, versus yaw angle for $H_AP$ model at $M = 0.4$	88
Fig. 48 -- Drag coefficient, based on front face area, versus yaw angle for $H_CP$ model at $M = 0.4$ and $M = 0.8$	89

# LIST OF ILLUSTRATIONS (cont)

	<u>Page</u>
Fig. 49 -- Drag coefficient, based on projected windward area, versus yaw angle for $H_C P$ model at $M = 0.4$ and $M = 0.8$	90
Fig. 50 -- Vertical centerline pressure distribution on $H_A$ block in UW tunnel, at $M \approx 0.2$ , mounting as parameter, $\psi = 0^\circ$	91
Fig. 51 -- Vertical centerline pressure distribution on $H_B$ block in UW tunnel, at $M \approx 0.2$ , mounting as parameter, $\psi = 0^\circ$	92
Fig. 52 -- Vertical centerline pressure distribution on $H_C$ block in UW tunnel at $M \approx 0.2$ , mounting as parameter, $\psi = 0^\circ$	93
Fig. 53 -- Variation of panel normal force coefficient with yaw angle for $H_A$ block at $M \approx 0.2$ , mounting as parameter	94
Fig. 54 -- Variation of panel normal force coefficient with yaw angle for $H_B$ block at $M \approx 0.2$ , mounting as parameter	95
Fig. 55 -- Variation of panel normal force coefficient with yaw angle for $H_C$ block at $M \approx 0.2$ , mounting as parameter	96
Fig. 56 -- Variation of panel normal force coefficient with yaw angle for $H_B G$ model at 100 and 150 mph	97
Fig. 57 -- Vertical centerline pressure distribution on wall ( $W_C$ ) and $H_C$ block at $M \approx 0.2$ , mounting as a parameter	98
Fig. 58 -- Pressure distribution on mounting plate forward of $H_A$ block in CWT test at $M = 0.4$ , tunnel pressure as parameter	99
Fig. 59 -- Pressure distribution on mounting plate behind $H_A$ block in CWT test at $M = 0.4$ , tunnel pressure as parameter	99
Fig. 60 -- Pressure distribution on mounting plate to the right of $H_A$ block in CWT test at $M = 0.4$ , tunnel pressure as parameter	100
Fig. 61 -- Pressure distribution on mounting plate forward of $H_A$ block in CWT test, Mach number as parameter	101
Fig. 62 -- Pressure distribution on mounting plate to the right of the $H_A$ block in CWT test, Mach number as parameter	102
Fig. 63 -- Pressure distribution on mounting plate behind the $H_A$ block in CWT test, Mach number as parameter	102
Fig. 64 -- Pressure distribution on mounting plate forward of $H_A$ block in CWT test at $M = 0.4$ , mounting as parameter	103
Fig. 65 -- Pressure distribution on mounting plate forward of $H_A$ block in CWT test at $M = 0.4$ , mounting as parameter	103

## LIST OF ILLUSTRATIONS (cont)

	<u>Page</u>
Fig. 66 -- Pressure distribution on mounting plate forward of $H_A$ block in CWT test at $M = 0.8$ , mounting as parameter	104
Fig. 67 -- Pressure distribution on mounting plate to right of $H_A$ block in CWT tests at $M = 0.8$ , mounting as parameter	105
Fig. 68 -- Pressure distribution on mounting plate forward of $H_A$ block in CWT and UW tunnel at $M = 0.2$ , mounting as a parameter	105
Fig. 69 -- Pressure distribution on mounting plate forward of block in UW tunnel at $M \approx 0.2$ , block form as parameter	106
Fig. 70 -- Pressure distribution on mounting plate to right of block at $M \approx 0.2$ , $\psi = 90^\circ$ , block form as parameter	106
Fig. 71 -- Pressure distribution on ground plane forward of block in UW tunnel at $M \approx 0.2$ , block form as parameter, $\psi = 0^\circ$	107
Fig. 72 -- Pressure distribution on ground plane forward of block in UW tunnel at $M \approx 0.2$ , block form as parameter, $\psi = 90^\circ$	108
Fig. 73 -- Pressure distribution on ground plane to right of block in UW tunnel at $M \approx 0.2$ , block form as parameter, $\psi = 90^\circ$	109
Fig. 74 -- Pressure distribution on mounting forward of $H_C$ and $W_C$ in UW tunnel at $M \approx 0.2$ , model as parameter	110
Fig. 75 -- Variation of panel normal force coefficient with yaw angle on square base prism (1:1:3.07) in NBS test, mounting as parameter (data from Reference 4).	111
Fig. 76 -- Variation of panel normal force coefficient with yaw angle on cube and square base prism (1:1:2.47) in Denmark test (data from Reference 5).	112
Fig. 77 -- Comparison of horizontal centerline pressure distribution on the mounted cube with the theoretical and experimental distributions for a flat plate.	113

## LIST OF SYMBOLS

$C_D$	Drag coefficient = $\frac{\text{Force in windward direction}}{\text{Area} \times \text{dynamic pressure}}$
$C_M$	Moment coefficient = $\frac{C_N \times \text{horizontal distance from center of pressure to center of face}}{\text{Width of face}}$
$C_N$	Normal force coefficient on a panel = $\frac{\text{Force normal to face}}{\text{Area of face} \times \text{dynamic pressure}}$
$C_R$	Resultant force coefficient on block = $\frac{\text{Resultant force}}{\text{Area of front} \times \text{dynamic pressure}}$
$\frac{\Delta P}{q}$	Pressure coefficient = $\frac{\text{Local pressure minus freestream static pressure}}{\text{Freestream dynamic pressure}}$
G	Ground plane mounting
$H_A$	Block form with dimension ratios of 1:1:1
$H_B$	Block form with dimension ratios of 1:1:2
$H_C$	Block form with dimension ratios of 1:1:4
M	Mach number
P	Plate mounting
$P_X$	Extension plane added to plate mounting
q	Dynamic pressure, $1/2\rho\gamma^2$
q'	Impact pressure, stagnation minus static pressure
$R_e$	Reynolds number based on block height
$W_C$	Wall with dimension ratio of 1:4
$\psi$	Yaw angle = angle between tunnel center line and perpendicular to house front
'	Prime used to denote coefficients based on impact pressure

Sample combination of symbols:

$H_A P_X$  (1:1:1 block mounted on the plate with the extension plane added)

## CH I -- INTRODUCTION

### Objectives

Wind tunnel tests at 25 miles per hour had been made on block forms at the State University of Iowa.\* Division 5112 of Sandia Corporation, hoping to apply the results to blast loading, proposed an extension of these SUI tests which would investigate other orientations and the effects of openings in some shapes. However, applicability of low-velocity wind tunnel data to blast loading was challenged in two areas: the application of steady-state data to the transient immediately following the diffraction phase of blast loading, and the application of low-velocity, low Reynolds number data to the high-velocity, high Reynolds number situation existing even at the later pseudo-steady-state phase of blast loading. Divisions 5112 and 5142 designed a wind tunnel test program to answer the second challenge; the first is under study in a separate project.

Specifically, the wind tunnel tests of block forms were made to determine the effect of subsonic Mach number and Reynolds number on external pressure distributions and drag coefficients throughout a complete range of yaw angles. It was also desired to determine the dependence of such effects on the length of block forms with common square cross sections. The velocity range available was from Mach 0.066 to 0.8. The corresponding Reynolds number range was from  $2.85 \times 10^5$  to  $4.0 \times 10^6$ .

### Theory

Square, flat plates showed no Reynolds number effect from  $10^3$  to  $10^7$ , the highest value given by Hoerner.† Since, like flat plates, block forms have separation points defined by their

---

\* Ning Chien, Yin Feng, Hung-Ju Wang, and Tien-To Siao, Wind-Tunnel Studies of Pressure Distribution on Elementary Building Forms, Iowa Institute of Hydraulic Research, State University of Iowa, 1951.

† Sighard F. Hoerner, Aerodynamic Drag, Published by Author, Midland Park, New Jersey, 1951.

shape, they were expected to be insensitive to Reynolds number throughout the same range. Whether the orientation of such blocks would affect their Reynolds number independence was open to question. Reynolds numbers of interest for blast loading extended to  $2.8 \times 10^8$ , a value higher than either the values available for the building form tests or those published for square flat plates. However, there is no reason to believe that the Reynolds number would become critical for bluff bodies as it does for spheres and cylinders where the separation point is free to move.

Compressibility effects would be expected to affect the value of drag coefficients definitely as velocity is increased to Mach 0.8. However, it should be possible to assess such effects to a reasonable degree of accuracy by considering the ratio of impact to dynamic pressure. Hoerner predicted that the drag of bluff bodies at high subsonic Mach numbers could be found by multiplying the low velocity, windward face, force coefficient by the ratio of impact to dynamic pressure and combining this value with the low-velocity force coefficient for the back face.

## CH II -- PROCEDURE

For this project, two different wind tunnels with about the same test section size (7 x 10 ft and 8-1/2 x 12 ft) were chosen in order to cover the desired velocity range and to check the reproducibility of results at a common velocity.

### Cooperative Wind Tunnel Series

The first test series was performed in August 1954 at the Southern California Cooperative Wind Tunnel (CWT), Pasadena, California. This facility is a variable density tunnel which allows either the Mach number or the Reynolds number to be varied while the other is kept constant. The tunnel provides a Mach number range from 0.2 to 0.8 and a Reynolds number range from  $1.3 \times 10^6$  to  $7.8 \times 10^6$  per foot.

#### Models

The models tested were flat-topped block forms with dimension ratios of 1:1:1, 1:1:2, and 1:1:4, and with a unit dimension of six inches. They were constructed of 3/8-inch brass plate with one set of end panels which fitted all three models.

The mounting designed for the tests was a 42-inch-diameter plate 0.45 inch thick (Figures 1 and 2). The edge was a half-wedge of which the plate top formed the sharp leading edge. The plate was supported approximately ten inches above the tunnel floor by four columns, while a hollow fifth column at the center carried pressure tubes. The supporting columns were secured to a yaw turntable in the tunnel test section so that the complete installation could be rotated through the yaw range. An extension plane which increased the mounting length by 18 inches was attached to the trailing edge of the plate at zero yaw to check the adequacy of the leeward mounting. To be adequate, the mounting should extend leeward to the distance that the wake affects the pressures on the model. Blocks were mounted at the center of the plate.

#### Instrumentation

An array of 165 external pressure ports was evenly distributed over the cube, while 20 additional ports were used on the front face of the two larger blocks (Figure 3). Two pressure-port lines, at right angles to one another, were so placed in the mounting plate that at zero yaw

one line with ten ports extended forward of the front face on the tunnel centerline, and the other line with six ports extended to the right of the right end vertical centerline. These ports rotated counterclockwise with the installation, so that at 90 degrees yaw they were to the rear and right of the model (looking downstream). Figure 4 shows the location of mounting-surface pressure ports.

### Data

The pressure ports were connected to 100-tube manometer boards from which data were recorded by photography. Recordings were made of the readings for each pressure port on each block plus reference pressures. The combination of parameters for which distributions were obtained is given in Table I, Part A.

A boundary layer survey was taken with a pressure rake, instead of a model, installed on the plate nine inches aft of the center of rotation for the range of test velocities.

A pressure distribution on the plate surface for the velocity range was obtained without having the model installed. Plate pressure distributions were taken at selected Mach numbers with only the cube installed on the plate at 0 and 90 degrees yaw, and on the plate plus extension at 0 degree yaw. Only one plate port was connected for the remainder of the runs.

### University of Wichita Series

The test series in the University of Wichita (UW) wind tunnel was performed in January 1955. This atmospheric tunnel was used at velocities of approximately 50, 100, and 150 miles per hour, with corresponding Reynolds numbers of  $5.68 \times 10^5$ ,  $1.09 \times 10^6$ , and  $1.66 \times 10^6$  per foot.

### Models and Instrumentation

Models and mountings used in the CWT series were tested at lower velocities in the Wichita tunnel. A wall, 6 x 24 x 0.25 inches, containing only vertical centerline pressure ports on the front and back, was added to the test.

In addition to the plate and plate plus extension, a separate and more extensive ground plane was used throughout the complete test range to further evaluate the effects of mounting. A mounting was needed to give the results of an infinite ground plane. The ground plane was supported twenty-five inches above the tunnel floor, extended from wall to wall in the test section, and had an over-all length of twelve feet. A thirty-inch circular disk, centered four



TABLE I

## Part A

## CWT DATA POINTS

Code for Yaw Angle Ranges

- a.  $0^{\circ}$ - $90^{\circ}$  at  $5^{\circ}$  intervals  
 b.  $0^{\circ}$ - $90^{\circ}$  at  $15^{\circ}$  intervals  
 c.  $0^{\circ}$ - $45^{\circ}$  at  $5^{\circ}$  intervals +  $90^{\circ}$   
 d.  $0^{\circ}$ - $45^{\circ}$  at  $15^{\circ}$  intervals

<u>Model</u>	<u>Mach Number</u>	<u>Reynolds Number</u>	<u>Yaw Angle</u>
$H_A^P$	0.2	$6.6 \times 10^5$	d
	0.2	$2.0 \times 10^6$	c
	0.3	$2.9 \times 10^6$	d
	0.4	$1.0 \times 10^6$	c
	0.4	$1.3 \times 10^6$	d*
	0.4	$2.0 \times 10^6$	d*
	0.4	$3.8 \times 10^6$	c
	0.65	$1.9 \times 10^6$	d
	0.8	$1.6 \times 10^6$	c
$H_B^P$	0.2	$6.6 \times 10^5$	75° and 90°
	0.2	$2.0 \times 10^6$	a
	0.4	$9.3 \times 10^5$	a
	0.4	$1.8 \times 10^5$	b
	0.4	$2.0 \times 10^6$	b**
	0.4	$1.8 \times 10^6$	a
	0.65	$2.0 \times 10^6$	b
	0.8	$1.6 \times 10^6$	a
$H_C^P$	0.2	$6.6 \times 10^5$	b
	0.2	$2.0 \times 10^6$	a
	0.4	$1.0 \times 10^6$	a
	0.4	$1.3 \times 10^6$	b
	0.4	$2.0 \times 10^6$	b*
	0.4	$3.8 \times 10^6$	a
	0.65	$2.0 \times 10^6$	b
	0.8	$6.6 \times 10^5$	a***

---

\*  $15^{\circ}$  missing

\*\*  $75^{\circ}$  missing

\*\*\*  $5^{\circ}$  and  $10^{\circ}$  missing

<u>Model</u>	<u>Mach Number</u>	<u>Reynolds Number</u>	<u>Yaw Angle</u>
$H_A^P X$	0.20	$7.3 \times 10^5$	$0^\circ$
	0.20	$2.0 \times 10^6$	$0^\circ$
	0.25	$2.0 \times 10^6$	$0^\circ$
	0.30	$1.0 \times 10^6$	$0^\circ$
	0.30	$2.8 \times 10^6$	$0^\circ$
	0.35	$2.0 \times 10^6$	$0^\circ$
	0.40	$1.4 \times 10^6$	$0^\circ$
	0.40	$2.0 \times 10^6$	$0^\circ$
	0.40	$3.8 \times 10^6$	$0^\circ$
	0.43	$4.0 \times 10^6$	$0^\circ$
	0.45	$1.1 \times 10^6$	$0^\circ$
	0.45	$1.5 \times 10^6$	$0^\circ$
	0.45	$2.0 \times 10^6$	$0^\circ$
	0.50	$1.7 \times 10^6$	$0^\circ$
	0.50	$2.0 \times 10^6$	$0^\circ$
	0.60	$1.7 \times 10^6$	$0^\circ$
	0.60	$2.0 \times 10^6$	$0^\circ$
	0.65	$2.1 \times 10^6$	$0^\circ$
	0.70	$1.7 \times 10^6$	$0^\circ$
	0.7	$1.9 \times 10^6$	$0^\circ$
	0.8	$1.7 \times 10^6$	$0^\circ$
$H_B^P X$	0.2	$6.8 \times 10^5$	$0^\circ$
	0.4	$1.3 \times 10^6$	$0^\circ$
	0.65	$2.0 \times 10^6$	$0^\circ$
$H_C^P X$	0.2	$6.9 \times 10^5$	$0^\circ$
	0.2	$2.0 \times 10^6$	$0^\circ$
	0.4	$1.0 \times 10^6$	$0^\circ$
	0.4	$1.1 \times 10^6$	$0^\circ$
	0.4	$1.9 \times 10^6$	$0^\circ$
	0.4	$3.9 \times 10^6$	$0^\circ$
	0.65	$2.0 \times 10^6$	$0^\circ$
	0.80	$1.7 \times 10^6$	$0^\circ$

#### Part B

#### UW DATA POINTS

(Includes only points for which data were tabulated)

<u>Model</u>	<u>Velocity (mph)</u>	<u>Reynolds Number</u>	<u>Yaw Angle</u>
$H_A^P$	100	$5.4 \times 10^5$	d
	150	$8.32 \times 10^5$	d
$H_B^P$	100	$5.47 \times 10^5$	b
	150	$8.32 \times 10^5$	b
$H_C^P$	100	$5.47 \times 10^5$	b
	150	$8.32 \times 10^5$	b

<u>Model</u>	<u>Velocity (mph)</u>	<u>Reynolds Number</u>	<u>Yaw Angle</u>
$H_A^P X$	50	$2.84 \times 10^5$	$0^\circ$
	100	$5.47 \times 10^5$	$0^\circ$
	150	$8.32 \times 10^5$	$0^\circ$
$H_B^P X$	50		
	100	$5.47 \times 10^5$	$0^\circ$
	150	$8.32 \times 10^5$	$0^\circ$
$H_C^P X$	100	$5.47 \times 10^5$	$0^\circ$
	150	$8.32 \times 10^5$	$0^\circ$
$H_A^G$	50	$2.86 \times 10^6$	d
	100	$5.52 \times 10^6$	d*
	150	$8.31 \times 10^6$	d
$H_B^G$	50	$2.86 \times 10^6$	b
	100	$5.52 \times 10^6$	b
	150	$8.31 \times 10^6$	b
$H_C^G$	50	$2.86 \times 10^6$	b
	100	$5.52 \times 10^6$	b
	150	$8.31 \times 10^6$	b
$W_C^P$	50	$2.84 \times 10^6$	$0^\circ$
	100	$5.47 \times 10^6$	$0^\circ$
	150	$8.32 \times 10^6$	$0^\circ$
$W_C^G$	50	$2.86 \times 10^6$	$0^\circ$
	100	$5.52 \times 10^6$	$0^\circ$
	150	$8.31 \times 10^6$	$0^\circ$

\*  $90^\circ$  added

feet from the leading edge of the plane, provided a rotatable model mount on which models were centered. The ground plane was constructed of plywood; the disk was constructed of aluminum and fit into an aluminum mounting ring (Figure 5). The leading edge of the plane was a half-round nose piece with 3/8-inch radius.

Sixteen surface pressure ports were included on the ground plane. Ten ports were forward of the disk along the tunnel centerline for all yaw angles, while six ports in the disk rotated with the disk. Figure 6 shows the location of the surface pressure ports.

### Data

Data were recorded in the same manner as in the CWT series, except that pressure values had to be taken in two parts because only one 100-tube manometer board was available. A model with 100 tubes connected was tested throughout the prescribed angle range at three velocities. The remainder of the ports were then connected, and the process was repeated. The combination of parameters for which pressure distributions were obtained is given in Table I, Part B.

Boundary layer surveys were taken on both plate and ground plane mountings with a pressure rake installed, in place of a model, nine inches aft of the center of rotation for each of the test velocities. Mounting surface pressures were obtained at the three velocities without the models installed. For all runs with models installed, surface pressures were obtained on the ground plane and on the plate surface along the pressure port line extending from the front face centerline.

Difficulties inherent in the yaw table rotation and in the method of angle calibration caused errors in the yaw angle settings for the plate estimated to be as large as 4 degrees at some settings.

### Data Reduction

The pressure data films were read by the testing agencies, and data were tabulated in form of pressure coefficients

$$\frac{\Delta p}{q} = \frac{(\text{local pressure minus free-stream static pressure})}{(\text{free-stream dynamic pressure})}$$

for each pressure port on each run. A blockage correction which included both solid and wake blockage factors was applied to the CWT data. The UW wind tunnel staff considered blockage to be negligible and ignored it.

The volume of data precluded complete reduction. Furthermore, complete tabulation of the data obtained at 50 mph at Wichita proved unfeasible because of inaccuracy.

Selected data in the form of pressure coefficients from both test series were reduced at the University of Wichita. The reduction of the University of Wichita data was completed in July 1955, and the CWT reduction was completed in September 1956. Pressure distributions were presented in graphic form; the normal force coefficients for each panel, and the resultant horizontal force coefficient with its angle of action for the block, were presented in tabular form.

To obtain a normal force coefficient, the pressure coefficients for each vertical row of pressure ports were plotted, and the area under each resulting curve was found by means of a planimeter. The resulting sectional coefficients for each row were plotted against the horizontal coordinate of the row; the curve was again integrated. The resulting area, divided by the panel areas, yielded the normal force coefficient for the panel. The horizontal coordinate of the center of pressure was also determined by this process, since the line planimeter used yields area and moment of area simultaneously. The other coordinate of the center of pressure was found by reversing the plotting sequence. Because finding the second coordinate of the center of pressure doubled the amount of work involved, this step was eliminated for many of the runs. The resultant force coefficients, based on front or end panel area, were found by considering the normal panel force coefficient as acting through the center of gravity. Therefore, only the horizontal translational force is represented by the resultant, since turning moments are ignored. However, the angle of action of the resultant was found and was later used by Sandia to determine the windward component of the resultant force. The tabulated centers of pressure were used by Sandia to find horizontal turning moments.

At an advanced state of reduction it was realized that the pressure curves on the windward panel were being faired to pass through a zero value of pressure coefficient at the free edges rather than allowing complete change to negative value on the adjoining panel to take place on the windward face. For the sake of consistency, the method of fairing in use was continued. Additional work was done at Sandia to assess the error caused by such fairing. The closest pressure port to the edge was a half-inch from the edge, so the exact pressure distribution near the edge could not be correctly determined.

Pressure contour plots were prepared for selected runs to illustrate the variations of pressure patterns with salient effects under study.

The values of normal force coefficients for panels, and resultant force coefficients with their angle of action, were used by the author in further analysis.

### CH III -- RESULTS AND DISCUSSION

#### Accuracy

Data were presented by the testing agencies without an accuracy analysis. It was evident from a study of the data and normal force coefficients that an over-all statement of accuracy was impractical. The scatter of data on various plots presented showed the relative accuracy from situation to situation. The accuracy of pressure data on windward faces seemed to be better than for faces on which pressures were negative, possibly because less flow stability in areas of separation resulted in the pressure data obtained being time dependent.

Lower test velocities showed greater percentages of data scatter than did higher velocities. The data from the 50-mph tests of the UW series and from the CWT series at Mach 0.2 and Reynolds number  $0.66 \times 10^6$  were too erratic to be considered reliable. Both of these sets of data showed a definite lack of symmetry at zero yaw, whereas the nature of the test would dictate symmetry.

Because yaw angles could not be set very accurately in the Wichita tunnel, part of the lack of accuracy in their data may be attributed to inaccurate angle settings.

Windward-face pressure distributions were faired through a zero value of pressure coefficient at the edges of the face, and both end and front values of normal force coefficients were affected by this fairing. Because horizontal distributions on the ends should have been faired to the edge at essentially a constant value, the absolute magnitude of the normal coefficient was too low. The maximum difference on ends caused by the different fairing was about 2.5 percent, and the difference for all models should be of the same order.

The difference in fairing on the front face depended on model size. The 1:1:1 windward face was influenced most, since a larger percentage of the area was affected. It was impossible to assess the difference precisely, for the exact pressure distribution at the edge was unknown. The closest pressure port to the edge was at half an inch, a position where pressures are significantly positive. The curve must be faired from this positive value to the negative value of the adjoining face with no intermediate guide points. The exact point of separation, and consequently the pressure distribution, was no doubt dependent to some extent on the sharpness of the edge. A comparison of the plots of windward-face pressures faired to the negative and

to the zero values at the edge suggested that the order of difference was approximately 4 percent for all windward 1:1:1 faces. The difference for the 1:1:4 face model was about 1.5 percent.

No attempt was made to assess differences in fairing for angles other than 0 or 90 degrees because of the greater difficulty in determining a "correct" fairing. Inaccuracy of fairing is greater at yaw angles such as 15 or 75 degrees on faces where pressure changes are very rapid near the model leading edge. Here there are few data points to guide fairing. In these situations, the value at the edge is not known. Consequently, there is a greater variation in normal force coefficients from different integrations at these angles than at zero yaw.

Since the normal force coefficients were obtained by a double integration using a planimeter, inconsistencies were unavoidable, especially since a number of people worked on the data reduction. Two reductions of the same data might vary as much as 3 percent for zero yaw, although they were usually within 1 percent.

## Velocity Profiles

### Boundary Layer

Figure 7 gives the boundary layer conditions existing on the plate mounting 9 inches aft of the plate center during the CWT tests. In (a) boundary layers at the high and low test Mach numbers at a tunnel wind-off\* pressure of 0.7 atmospheres are compared; it is seen that the higher Mach number gives a slightly thicker boundary layer. In (b) two Mach numbers are shown with the tunnel operating at a pressure of 3 atmospheres; the boundary layer for the lower Mach number is slightly thicker. The same Mach number is presented for two different tunnel pressures in (c), and very little difference can be seen in boundary layer. In (d) the Mach number and tunnel pressures are adjusted to give approximately the same Reynolds number, and more difference is shown than for a constant Mach number. The difference is similar to that shown in (b) for a constant pressure and varying Mach number. Note, too, that the velocity has reached 0.99 of the free stream value in less than 1.25 inches of height in all situations, usually between 0.75 and 1.0 inch.

Figure 8 compares the boundary layer profiles on the plate and ground plane mountings nine inches aft of the center of rotation for the three velocities used in the UW tests. The

---

\*Tests were run with constant mass operation; therefore, the tunnel pressures given are wind-off pressure. Static pressure varies from wind-off pressure as Mach number is increased.

difference in the boundary layer thickness for the two mountings is not as prominent as is their difference in profile. Velocity reaches 0.99 (approximately equivalent to 0.98 of free stream  $q$ ) of free stream between 1.25 and 1.5 inches above the mounting at 50 mph. The plate profiles at 100 and 150 mph show velocities reaching 0.99 of free stream at a height of about 1.1 inches. Boundary layer thicknesses on the ground plane are less than 1 inch for these higher velocities.

A comparison of the boundary-layer thickness on the plate in each of the two tunnels at approximately the same Mach number and tunnel pressure shows a thickness in the UW tunnel of about 1.1 inches compared to 0.9 inch for CWT.

#### Velocity Distribution on Mounting Surface

In the CWT series, no separation at the leading edge of the plate was evident for Mach numbers lower than 0.6, but separation was quite pronounced at Mach 0.6 and 0.8. This is shown in Figure 9, which gives plate surface profiles with only the rake installed. Where separation occurs, it is seen that reattachment occurs within a few inches. Figure 10 gives the Mach number distribution to the right of the center of the plate, looking downstream. In both Figures 9 and 10 it appears that the results at Mach 0.8 are influenced by the extension plane, while results at Mach 0.2 are influenced by the static pressure of the tunnel.

Pressure distributions on the plate and ground plane mounting surfaces for the UW series are shown in Figures 11 and 12, respectively, for each of the three test velocities. The leading edge separation for either mounting is greater than for a comparable velocity in the CWT but less than for the high velocities in the CWT. Reattachment occurs early and the flow is quite smooth at the model position.

#### **General**

The effects of Mach number, Reynolds number, yaw angle, and model size being investigated here are not necessarily the same for all faces of a block form; therefore, data are more meaningful and interesting if presented, at least in part, in the form of sample distributions and normal force coefficients on separate faces. Throughout the discussion the various faces will be distinguished by their zero yaw designation regardless of the orientation. Yaw angles are positive as the model is turned counterclockwise (looking on a plan view).

Because of the large number of parameters involved in the investigation, it was often necessary to combine two or more parameters. In particular, the effects of house size and mounting were often dealt with in conjunction with other parameters.



Reynolds numbers are based on the model height and therefore do not vary with orientation or model.

Although less than two-thirds of the raw data obtained has been reduced, this quantity is still too large to be presented satisfactorily in this report. Therefore, only representative data are presented, especially for orientations other than normal incidence.

### Comparison of Data from Tunnels

Since two different wind tunnels were used in the test, data were compared to determine if there was any consistent difference for which compensation could be made by a correction factor. Figure 13 presents the normal force coefficient for each face at all angles of yaw for the  $H_C$  model. The curve has been faired for an average of both sets of data. The figure shows no consistent difference on the front or ends, although there is significant difference at certain points. The coefficients on the back are, however, consistently lower for the UW data than for the CWT data, but no correction for a single face is felt justified. These comparisons have been made for the plate mounting since no ground plane was used in the CWT series. Since both Reynolds number and Mach number approach the same value, difference in data cannot be attributed to either of these parameters.

### Reynolds Number Effect

The range of Reynolds number variation, while not large, should be sufficient to show a trend if any exists. For presentation of the results of the Reynolds number study, the largest block form ( $H_C$ ) has been chosen at Mach number 0.4. The data supported the assumption that if a Reynolds number effect exists, it will be prevalent on the  $H_C$  block. Mach 0.4 was the only number with sufficient variation for the study.

Figure 14 gives the variation of normal force coefficient with Reynolds number for each face at various yaw angles. The  $H_C P_X$  model combination is shown for zero yaw merely because there are more data for it than for the  $H_C P$ . For some combinations of block face and angle, the values of  $C_N$  for various Reynolds numbers are significantly different. However, the inconsistency of such differences hinders their being attributed to a change in Reynolds number. Inaccuracy of  $C_N$  on faces which have steep pressure gradients is greater than for those which have more nearly constant values. This contributes to variations with Reynolds number at such angles. As a further indication of the inaccuracy that  $C_N$  contributes,

it is pointed out in the figure for zero yaw that the right- and left-end coefficients should be identical, and at  $45^\circ$  for  $H_A$  model (Figure 15) the front and left coefficients and right and back coefficients should have the same values. The difference in the two negative faces of  $H_A$  for  $45^\circ$  at a Reynolds number of  $1.34 \times 10^6$  is of the same order as the largest variations of  $C_N$  with Reynolds number (variation of 0.5 to 0.7 in  $C_N$ ). The angles given for this data vary from  $44.98^\circ$  to  $45.01^\circ$ . Therefore, unless there is an unknown error in angle calibration, the difference must be attributed to the inherent inaccuracies of the data and data reduction.

It is concluded that for the Reynolds number range from  $10^6$  to  $4 \times 10^6$  there is no interpretable Reynolds number effect.

### Mach Number Effect

The first study of Mach number effect was of the windward-face normal-force coefficient. Figure 16 gives the variation of the  $H_A$  front-face normal-force coefficient with Mach number at zero yaw. The plate and plate-plus-extension mountings are shown at a constant Reynolds number of about  $2 \times 10^6$  ( $M = 0.8$  is at  $1.66 \times 10^6$ ). It appears that the coefficients are independent of the mounting. In Figure 17 other Reynolds number data points have been added to the data presented in Figure 16. Data shown here for Mach numbers below 0.200 are from the UW series. The points at  $M = 0.133$ ,  $C_N = 0.735$ , and 0.802 appear to be in error since the pressure coefficients at the face center were 0.93 and 1.03, respectively, rather than stagnation pressure which existed for all other situations. The  $M = 0.066$  point is not considered reliable.

Figure 18 shows an interesting agreement of force coefficients for all models with the  $1 \times 1$  face in a windward position. Figures 19 and 20 give the unyawed front-face normal-force coefficients versus Mach number for the  $H_B$  and  $H_C$  forms, respectively. Similar to the  $H_A$  block, the front faces of the larger forms are not influenced by addition of the leeward mounting extension ( $P$  vs  $P_X$ ). Figure 21 shows the variation of  $H_C$  front-face normal-force coefficient with Mach number and yaw angle (from  $0^\circ$  to  $75^\circ$ ).

To show other effects of Mach number and model size on the front-face pressures at zero yaw, sample vertical centerline distributions are presented. Figure 22 shows the effect of house breadth on the front-face vertical centerline pressure distribution at zero yaw for Mach numbers of 0.2 and 0.8. For the square face at  $M = 0.2$ , the pressure is essentially the stagnation value from the base to the center; from this point the pressure decreases as the top is approached. The negative top face pressure at the farthest forward station is

assumed to extend to the front edge; therefore, the front value at the top edge is negative and equal to the top value. For both  $H_B$  and  $H_C$  models, the pressure distributions have a definite "dip" at about a quarter of the height and are indicative of a vortex formed in front of these blocks. Probably the vortex is a result of friction on the mounting and is related to boundary layer and model width. Pressure distribution over the entire face, and consequently the front-face normal-force coefficient, is affected by this vortex. The value of  $C_N$  is not that which would have been obtained with a twin model (no ground mounting).

Figure 23 is presented to show how Mach number affects the front-face pressure distributions for the  $H_A$  and  $H_C$  houses. For all Mach numbers the center of the cube is essentially at stagnation pressure. The "dip" starts to appear on the  $H_A$  block between Mach numbers 0.4 and 0.65, indicating possibly that at higher Mach numbers there is a vortex forward of the cube, or some other boundary layer influence. On the  $H_C$ , the "dip" is a little more pronounced at higher Mach numbers, but the primary effect of increasing Mach number is to increase all pressures. As expected, addition of the extension plane to the plate has no discernible effect on the "dip." The front-face center point is at stagnation pressure for the  $H_A$  model, but a stagnation pressure is not reached above the base on the other models.

Figure 24 gives the variation of the back-face normal-force coefficient with Mach number for the three models on each of two mountings at zero yaw. These sets of data are more difficult to interpret than are the front-face data. The  $H_A$  model shows no effect of the extension plane except at  $M = 0.8$  (Figure 24). It may be concluded that  $C_N$  for the back of the  $H_A$  model is independent of Mach number, at least with an extension plane. The  $H_B$  model appears to be independent of Mach number for a plate mounting, but data from the extension-plate mounting seem inconsistent with  $H_A$  and  $H_C$ . The plate-mounted  $H_C$  model exhibits greater negative pressures with increasing Mach number. Addition of an extension creates greater negative back pressure than exists with only the plate. The vortex forward of the model probably influences the pressure on the back. However, it is not possible to assess this effect at present.

Figure 25 gives the variation at zero yaw of the end-face normal-force coefficients with Mach number for  $H_A$  and  $H_C$ . Values of the coefficients for both ends are averaged in order to eliminate, as much as possible, errors of orientation or data reduction. Trends here are not well defined, although, for the cube, there seems to be a lessening of negative pressure on the end with increasing Mach number. For  $H_A$  the influence of the extension plane appears greatest at  $M = 0.8$ . At lower Mach numbers the  $H_C$  model shows greater negative pressures on the ends with the extension than without it; this is consistent with the back-face results. Data are not conclusive, but it appears that the pressures with the extension plane become less

negative with increasing Mach number. For both back and ends, the difference between normal-force coefficients with and without extension planes becomes less with increasing Mach number on the  $H_C$  block. This is not the situation with the  $H_A$  model. It is believed that some of the inconsistencies noted can be attributed to inaccuracies of the coefficients since, as previously pointed out, the negative-pressure data are less accurate than the positive-pressure data. Vortex formation forward of the blocks may also influence end pressures.

Figure 26 gives the variation of the leeward face (originally an end face) normal-force coefficients with Mach number for all three models at  $90^\circ$  yaw. Results are not immediately explainable.  $H_A$  shows no effect of Mach number except at  $M = 0.8$  with the plate mounting;  $H_B$  shows a definitely increasing negative pressure with increasing Mach number, while  $H_C$  shows a tendency for decreasing negative pressures with increasing Mach number. In order to determine whether or not this change in slope of coefficient versus Mach number with house form is feasible, plots in Figure 27 compare the horizontal centerline pressures along the face parallel to the wind direction at various Mach numbers for each of the three models. Pressures are plotted from leading to trailing edge of the side (front face at  $90^\circ$  yaw). Pressures near the trailing edge show the same variation with Mach number for the  $H_B$  and  $H_C$  models as was evident in Figure 26.

Figure 28 presents resultant-force coefficients ( $C_{N \text{ front}}$  minus  $C_{N \text{ back}}$ ) for each of the unyawed models versus Mach numbers for both of the mountings. With the exception of  $M = 0.8$ , the  $H_A$  block is not influenced by the extension plane, and the resultant coefficient steadily increased with Mach numbers. The  $H_B$  block shows a greater increase of the resultant coefficient with Mach number for the plate mounting alone than for the plate plus extension. The  $H_C$  block shows less Mach number effect for either mounting at the lower than at the higher Mach numbers. For both the  $H_B$  and  $H_C$  block, the difference between the values for the two mountings becomes less with increasing Mach number.

Figure 29 shows the resultant force coefficient for ninety degrees yaw versus Mach number for each of the houses. As in Figure 28, the resultant is the combined windward- and leeward-face coefficients with no contribution from the side faces.

#### Compressible Flow Corrections

At high subsonic Mach numbers, the difference between the local and static pressure at the stagnation point is greater than the dynamic pressure ( $1/2 \rho v^2$ ). This difference between

stagnation and static pressure, impact pressure ( $q'$ ), is related to dynamic pressure for subsonic speeds by

$$\frac{q'}{\frac{1}{2}\rho v^2} = 1 + \frac{M^2}{4} + \frac{M^4}{40} + \dots \approx 1 + \frac{M^2}{4}. \quad (1)$$

Drag of bluff forms with flow entirely detached from the rear consists of two components: a positive front pressure (local minus static) which is proportional to impact pressure, and a negative base pressure assumed to be independent of Mach number in the subsonic field.\* The high Mach number drag coefficient of two-dimensional flat plates (or similar bodies having the same flow pattern) for which the drag coefficient components at low Mach numbers are known, can be found from

$$C_D = \left(1 + \frac{M^2}{4}\right) \times C_{N \text{ front}} - C_{N \text{ back}}. \quad (2)$$

at  $\psi = 0^\circ$

In order to apply this equation, values of  $C_{N \text{ front}}$  for low Mach number and  $C_{N \text{ back}}$  must be chosen. Since data for Mach numbers below 0.4 are quite scattered and sparse, the average values of  $C_N$  at Mach number 0.4 have been taken from the curves presented for front- and back-face normal coefficients versus Mach number for zero yaw. The zero Mach number coefficient for the front face was computed from these Mach 0.4 values, and the zero Mach number coefficient for the back was assumed to be the same value as for  $M = 0.4$ . The drag coefficient was calculated from

$$C_D = \left(1 + \frac{M^2}{4}\right) \times C_N (\text{front at } M = 0) - C_N (\text{back at } M = 0).$$

Drag coefficients obtained from this equation for the  $H_A$ ,  $H_B$ , and  $H_C$  block forms are given for both mountings in Figure 30. Comparison with Figure 28, which gives experimental results, shows what is considered to be good agreement. The difficulty encountered in calculating drag coefficients for high Mach numbers is the choice of the incompressible coefficients ( $C_N$  at  $M = 0$ ) in the absence of reliable low velocity data.

---

\*Sighard F. Hoerner, Aerodynamic Drag, Published by Author, Midland Park, New Jersey, 1951.

The curves presented in Figure 31, for a ninety-degree orientation, were computed by following the same procedure as was used for Figure 30. The agreement with Figure 29 is good for  $H_A$  and  $H_C$  but is not good for  $H_B$ , for which, it will be recalled, the leeward-face pressures showed great variation with Mach numbers.

The result of multiplying the front-face coefficients taken from the curves given in Figures 16, 19, and 20 by the ratio of dynamic pressure to impact pressure is given in Figure 32 for all three models from Mach numbers of 0.2 to 0.8. The curves do not have a constant value as predicted by the theory. However, the difference is about 6 percent for the  $H_A$  model which has the greatest variation.

Plots of vertical and horizontal centerline pressure distributions, based on impact pressures, on the windward face of  $H_A$  for several Mach numbers are shown in Figure 33. As would be expected, agreement is excellent at the stagnation points; however, it becomes poorer near the edges where pressure does not drop as rapidly for the higher Mach numbers as for the lower ones. Also, a vertical centerline dip, similar to that shown previously in Figure 23, is present for higher Mach numbers.

#### Effects of Yaw Angle

##### Sample Pressure Distributions

Figure 34 is presented to show how the horizontal centerline pressures on a cube change as the model is rotated. Probably the most notable effect is the increased negative pressure formed, because of the vortex, near the leading edge of the left end which is rotated into the wind as the cube is turned from 0 to 15 degrees yaw. The magnitude of the effect is sufficient to produce a negative drag component for the ends from 0 to 20 degrees,  $\pm 5$  degrees, yaw. This is evident on plots presented later. Comparison of minimum recorded pressure coefficients and normal force coefficients ( $C_N$ ) on the left end for small angles of yaw is given in Table II for  $M = 0.4$  and  $R_e \sim 4 \times 10^6$ . At these angles the minimum pressure present on any vertical face of the block is the minimum pressure for the left end.

TABLE II

<u>Yaw Angle</u>	<u>Minimum pressure Coefficient</u>	<u>Normal force Coefficient</u>
5°	-0.655	-0.580
10°	-1.000	-0.676
15°	-1.068	-0.534
20°	-0.687	-0.297

Pressure ports were not close enough to the edge to indicate the separation at the leading edge of the left end between 30 and 40 degrees yaw, although theory and experiment establish its existence.

The horizontal centerline pressure distribution for the  $H_C$  house is shown in Figure 35. The left face features are similar to those for  $H_A$ , since these faces are the same size and are oriented similarly. Table III gives information for the left end of the  $H_C$  house at  $M = 0.4$  and  $R_e \sim 4 \times 10^6$  similar to that given in Table II for the  $H_A$  model.

TABLE III

<u>Yaw Angle</u>	<u>Minimum Pressure Coefficient</u>	<u>Normal Force Coefficient</u>
5°	-0.56	-0.484
10°	-0.65	-0.592
15°	-0.84	-0.672
20°	-1.35	-0.599
25°	-0.84	-0.405

The effect of the greater length of the front face is seen by comparison with Figure 34. Pressure approaches the free stream value near the trailing edge of the front and back face at 90 degrees yaw. Values for the two pressure ports near the right edge of the front face are unavailable; therefore, the exact shape of the curve cannot be determined. The negative pressures on the right end decrease as the face is turned to become the leeward face.

#### Contour Maps

Selected contour maps, presented in Appendix A, give a complete picture of the variation of the entire pressure distributions with angle of yaw as well as indications of variations with Mach number and house breadth.

The variation of pressures on the top face and the peak negative values (which occur on the top face) can be seen from these contour maps and will not be discussed further.

#### Comparison of $C_N$ Versus Yaw Angle for Various Models and Mach Numbers

Previous figures have shown the effect of Mach numbers and house depth on the normal force coefficients of various faces at zero yaw. The influence of yaw angle is considered next. In the current series of plots, as in some subsequent series, curves have been faired through the data points, not because the data are of sufficient accuracy, but to increase clarity in areas where point density may cause confusion.

Figure 36 gives the variation of normal force coefficients with yaw angle for each vertical panel of the  $H_A$  and  $H_C$  models at a Mach number of 0.4 and a Reynolds number of  $3.8$  to  $3.9 \times 10^6$ . The  $H_A$  block was turned only through 45 degrees yaw. The dashed curves shown between 45 and 90 degrees were obtained from the data plotted for other faces (which is possible because of the symmetry of the cube). The inconsistent value for the left end of the  $H_C$  model at 40 degrees was carefully checked and compared to data for other Reynolds numbers. A sequence of contours was studied; the conclusion reached is that the value is in error.

The left-end face, which is the same size for both blocks and which is in the same relative position, does show a similarity for the two models. It is noticed, however, that the lowest negative pressure occurs at about 5 degrees greater yaw for the  $H_C$  than it does for the  $H_A$  model. The pressures on the right-end faces are of the same order of magnitude near zero yaw but vary greatly at angles greater than 45 degrees. This is to be expected, since on the  $H_C$  model the flow has much more time to reattach before reaching the right face which turns to become the leeward face at 90 degrees. The front face of the  $H_C$  presents much more area than does an end face, so that the large negative pressures in the vortex region near the leading edge at 75 to 80 degrees yaw (similar to low negative pressures on the left end at 10 to 15 degrees yaw) are overshadowed by the higher pressures aft of the vortex region; therefore,  $C_N$  does not become less negative than the 90-degree-yaw value.

Figure 37 compares the normal force coefficients for various faces of the  $H_B$  model with those of the  $H_C$  model over the complete yaw-angle range. The curve for  $H_C$  is repeated from Figure 36. There are data at only 15-degree intervals for the  $H_B$  model, so that trends are not as well defined as for the  $H_C$  model. Curves for the left and right faces are not faired because of an insufficient number of data points. The  $H_B$  house shows the same type of variation as does the  $H_C$ , but to a lesser extent.

Figure 38 compares the variation of normal force coefficients with yaw angle for two Mach numbers on the  $H_C$  block. These data indicate that the effect of Mach number is larger on windward faces than on sheltered faces.

Figures 36 and 38 give all four components of the resultant force acting on the body at each angle of yaw. Figures 39, 40, and 41 combine the four force components (given in the preceding figures) into two components which are at right angles to each other (one normal to the front and back faces, and the other normal to the end faces). The first of this series of plots is for the cube through a 45-degree-yaw range at a Mach number of 0.4. Here the negative drag component of the end faces is obvious. Figure 40 shows the two right-angle



components for  $H_C P$  at a Mach number of 0.4. Other Reynolds numbers have been added to again illustrate the lack of consistent Reynolds-number effect. The greatest contribution to the resultant forces by the ends is made at 75 degrees yaw. The front-back contribution changes slowly through the first 35 degrees of yaw; the change is fairly constant through the remainder of the yaw range. The 0.8 Mach number data shown in Figure 41 show no over-all variation from data shown in Figure 40. The variation of the front-back component is slightly more rapid near zero yaw, and magnitudes are different. Figures 40 and 41 show that the resultant force for the  $H_C P$  at 90 degrees yaw is less than that for the cube (0 degree in Figure 39), since the leeward face pressure of the  $H_C P$  is less negative than that of the  $H_A P$  (model length effect on leeward pressures).

### Resultant Force and Drag Coefficients Versus Yaw Angle

The next step in finding the resultant force coefficient is to combine the right-angle components, taking into consideration the difference in area of the different faces. The front-face area has been chosen as the normalizing area. The normal force coefficients which have been previously discussed and plotted do not necessarily act at the physical center of the face. Therefore, to completely describe the loading on the body, the coefficient of moment ( $C_M$ ) must also be included. These moment coefficients have been computed from

$$C_M = \frac{C_N \times \text{horizontal distance from center of pressure to center of face}}{\text{Width of face}}.$$

A positive moment appears clockwise when one looks on a plan view of the model.

Figure 42 gives the resultant force coefficients formed by combining the components of Figure 39 vectorially; Figure 43 gives moment coefficients versus yaw angle for the cube. Relatively small variation in resultant force coefficients is seen through the angle variation.

Figures 44 and 45 give data similar to those given in Figures 42 and 43 but, for the  $H_C P$  model at Mach numbers of 0.4 and 0.8 (left-right face components from Figures 40 and 41 are normalized to the front-face area before they are combined vectorially with the front-back components). From 0 to 60 degrees of yaw, the higher Mach number gives higher resultant force coefficients, while from 60 to 90 degrees the coefficients are similar. The moments show large variation only from 50 to 90 degrees. Figures 42 to 45 completely describe the horizontal loading on the models, but they do not consider vertical loading, which is not discussed.

The resultant coefficients given in Figures 42 and 44 are not necessarily in the direction of the wind; therefore, they cannot be termed drag coefficients. Components of  $C_R$  in the

wind-direction, drag coefficients, based on the area of the front face of the model, have been computed, as have the drag coefficients based on the projected windward area. For the sample models, these results are presented as Figures 46 to 49.

#### Comparison of Mounting Effects on the Models in the University of Wichita Tests

Figures 50, 51, and 52 give the zero-yaw vertical centerline distribution on the  $H_A$ ,  $H_B$ , and  $H_C$  blocks, respectively, with mounting as a parameter. Because of data density, only curves for the plate and ground-plane mountings are faired. The difference between plate and plate-plus-extension plane results on the front face is not significant for any house. The difference in data for the plate and ground-plane mountings becomes more significant as the house size is increased. On the top and back of the  $H_A G$  and  $H_A P_X$  models, results agree, while the  $H_A P$  model values are less negative. For the  $H_B$  block, the plate and plate-plus-extension pressures are similar, while the ground plane gives more negative pressures. The tendencies shown for the  $H_B$  block are amplified in the  $H_C$  results. A change in curvature of the pressure curve for the top panel with the ground-plane mounting is evident for all three models.

The next series of figures amplifies the comparison of ground-plane and plate-mounting results. In Figures 53, 54, and 55, normal force coefficients for both mountings are plotted against yaw angle for each of the three models. Curves are faired for  $H_i P$ 's, while data points are shown without fairing for  $H_i G$ 's. From a study of these figures some features, which might be expected if the plate mounting were insufficient, are evident. The smallest model shows the least difference between mountings. Windward faces show less effect than negative pressure faces. The small (1 x 1) windward face (left at 90 degrees) shows the least effect of the windward faces. For the  $H_C$  model all faces show the least effect at 90 degrees yaw. Since the wake may close sooner behind the  $H_C$  model at this velocity, the leeward extent of mounting may not need to be as great. The greatest effect on the  $H_B$  model appears on the ends at zero yaw. The negative dip which was prominent on the left end at 0 to 15 degrees yaw for the plate-mounted models is not evident for the models mounted on the ground plane. Perhaps low points are missed by the larger (15-degree) interval of yaw angle.

Somewhat larger magnitudes of error are present in the UW data than in the CWT data. This is evident from comparisons of normal force coefficients on two faces for which the values should be the same as a result of symmetrical loading.

The unassessed variation of normal force coefficients with mounting creates an uncertainty in the choice of values of coefficients in which confidence can be placed. This is especially true for the negative pressure faces of the two larger models.

The University of Wichita did not reduce data for 100-mph tests except for the  $H_B G$  configuration, since it was thought that the data were nearly the same as the 150-mph data. Comparison of 100- and 150-mph data for the one situation where both were reduced is shown in Figure 56. There is no consistent difference, even though the difference on the front at 0 and 90 degrees yaw and on the back at 90 degrees yaw is large.

#### Depth Effect for 1 x 4 Model

Only a vertical centerline was instrumented on the 1 x 4 wall in the Wichita tests, so the depth effect is presented as a pressure profile in Figure 57 with data for the  $H_C$  and  $W_C$ . Both mountings are included to illustrate that depth effect, which is of interest, is difficult to evaluate since it is influenced by the mounting variation.

#### Pressure Profiles on Mountings

Some idea of the variation of flow patterns around models with different mountings can be gained by a study of the pressure distributions on the mounting surfaces. Unfortunately, mounting-pressure data were obtained for only the  $H_A$  block in the CWT tests. It would be expected that if there was a mounting insufficiency, it would be more pronounced for the larger models, which approach closer to the mounting edge. It is unfortunate that the plate-plus-extension was not used at 90 degrees yaw as well as at zero yaw, so that the mounting profile difference could be determined for the situation in which the model extends nearer to the trailing edge. In the UW series, no surface pressures were obtained in the wake on the leeward side since only one line of pressures was obtained on the mounting. However, the information which was obtained is of sufficient interest to warrant study.

Figure 58 gives the variation of pressure coefficient with distance forward of the plate-mounted  $H_A$  model at a constant Mach number; the CWT operated at four different pressures which give a Reynolds number variation. Pressures are along the plate centerline forward of the front face at zero yaw. The coefficients for the tunnel pressure below one atmosphere are lower than the other coefficients. There is no clear distinction for any of the other three tunnel pressures. A stagnation condition exists at least an inch forward of the model for all tunnel pressures except 0.7 atmosphere. In this and in succeeding figures for the plate-mounted  $H_A$  block, there is a discontinuity which appears about five inches forward of the

model. The variation of the curves with atmospheric pressure is not of sufficient magnitude to be indicative of a Reynolds number influence on flow pattern. Figure 59 gives the distribution of pressure coefficients on the plate to the rear of the model for tunnel wind-off pressures of 3.0 and 0.7 atmospheres. Figure 60 is similar, except that the pressures were taken to the right (looking downstream) of the right-end face. No Reynolds number influence is evident to the rear, and it is insignificant to the side. The change in curvature on the side probably corresponds to the wake or separation line.

Figures 61 to 63 show how the flow pattern on the mounting-plate surface is affected by Mach number. Figure 61 indicates that a change in Mach number changes the magnitude of pressure but does not significantly alter the pattern in front of the model except for the separation which occurs at the leading edge for the higher, but not lower, Mach numbers in the range tested. As shown in Figure 9, separation is not dependent on the presence of a model. In Figure 62, to the side of the model, pressures inside the separation area are different for  $M = 0.8$  than for other Mach numbers, but outside the wake all Mach numbers show quantitatively the same pressures. Figure 63 indicates that there seems to be no Mach number effect to the rear of the model for values of 0.2 and 0.4, but 0.8 shows qualitative and quantitative differences. Longer wake apparently accompanies higher Mach numbers. Similarity of results at 0.2 and 0.4 probably indicates a threshold at Mach number greater than 0.4 and less than 0.8.

In Figures 64 to 67 the pressure distribution on the plate with extension plane is shown forward and to the side of the model for two Mach numbers. Pressure curves to the side with the extension do not match the plate curves for  $M = 0.8$ . It will be recalled that the addition of the extension plane to the plate mounting affected the distribution on the plate without the model installed (Figures 9 and 10).

Figure 68 compares pressure distribution forward of the  $H_A$  model on two different mountings in two different wind tunnels at a common velocity. At the port, three inches forward of the face, the Wichita tunnel gave lower pressures on both mountings; otherwise no tunnel effect is in evidence.

Figure 69 presents data which compare the distributions obtained with each of the three houses installed on the plate with the University of Wichita tunnel operating at  $M \approx 0.2$ . A decided dip in the distribution is apparent for the larger models, especially for the  $H_B$ . It is possible that lower values of pressure existed for the  $H_C$  than were recorded, due to the spacing of the pressure ports. This dip is a more pronounced form of the discontinuity noted for the  $H_A$  block, and it is indicative of the vortex being formed forward of the model. One

line of ports was to the right of the center of the plate at 90 degrees yaw. The distributions for this line (Figure 70) show a distinct difference for the largest house, which seems reasonable when it is considered that the flow has traveled four times as far as for the  $H_A$  and could have approached reattachment to the body.

Figure 71 gives the pressure distribution on the large ground plane in the UW tunnel at  $M \approx 0.2$ . The vortex disturbance, present in front of the models where a small disturbance was noted for the plate mounting, is much stronger for the ground plane. The magnitude of this disturbance seems to depend on the house frontal area. The leading edge separation does not appear to be influenced by model size, or even model presence, as shown by comparison of Figure 71 with Figure 12. At 90 degrees yaw the ports in the plywood ground plane are still along the tunnel centerline, while those in the rotating disk are to the side (right-angle line to flow direction). The distributions for these two lines are shown in Figures 72 and 73. Each model in this orientation presents the same size face to the wind, but the streamwise length varies. No great difference in distributions is noticed forward of the model. Figure 73 shows that body length has more influence to the side than forward, as would be expected. Comparison with Figure 70 shows that the ground plane creates a different flow situation to the side of the models than exists for the plate mounting. The large increase in negative pressure at the pressure port nearest the  $H_C$  model (ground-plane mounting shown in Figure 73) exists throughout the range of yaw angles. No explanation is offered for this situation.

Figure 74, which is similar to Figure 72, gives a house-depth effect; the effect in Figure 74 is for the large face turned windward. Comparison of the  $H_C$  and the  $W_C$  is made for both mountings. Pressures are plotted versus distance from the windward face. It is interesting to note that with the ground-plane mounting there is no depth effect, at least to the extent for which data are available, whereas with the plate mounting, a depth effect is noticed eight inches forward, and a difference between mountings with the same model is present eleven inches forward of the model.

#### Comparison With Other Experiments

The influence of a ground surface on the vertical pressure profile of a two-dimensional flat plate has been investigated by Nøkkentved.\* Four combinations were tested: model on

---

\*Chr. Nøkkentved, Variation of the Wind-Pressure Distribution on Sharp-Edged Bodies, Laboratorium for Byggestatik Danmarks Tekniske Hjskole, 1936.

tunnel floor, twin model freely exposed, twin model with leeward splitter plate, and twin model with splitter plane forward of the model. Both the forward-splitter plane and floor mounting produced "dips" in the vertical front-face profile with no stagnation pressure being recorded. The floor mounting gave a more pronounced dip, i. e., there was a lower pressure at the low point and more toe-out near the base. As would be expected, the floor mounting and leeward splitter plane greatly reduced the back-face pressures. The average pressures are given in Table IV. In the Danish tests it was concluded that the boundary layer thickness determines the shape of the windward vortex layer.

TABLE IV

<u>Mounting</u>	<u>Front Pressure Coefficient</u>	<u>Back Pressure Coefficient</u>
Freely exposed	0.77	-1.14
Front splitter plane	0.63	-1.02
Floor mounting	0.63	-0.37
Back splitter plane	0.72	-0.57

The profiles given in Reference 3 are similar in character to those found for the block forms in the CWT and UW tests, but the peak pressures recorded in the Danish tests were lower.

#### Effects of Mounting on Force Coefficients

A series of experiments were performed at the National Bureau of Standards to determine pressure distributions on a square-base prism (8 x 8 x 24.5 inches) at speeds up to 70 mph. Tests were run in a 10-foot diameter, cylindrical test section. The model was tested both on the tunnel floor and at the center of a platform. The platform extended across the tunnel, was two feet above the floor at the center, had a beveled leading edge, and extended five feet upstream.

Boundary-layer profiles showed a thick boundary layer on the floor, but a relatively thin one on the platform. The pressure coefficients given in the report were obtained by averaging results from velocities of 27.3, 40.9, 54.5, and 68.2 miles per hour. Reduced normal-force coefficients given are shown versus yaw angle in Figure 75 for both mountings. Lower pressures were obtained on the front face with the floor mounting than were obtained with the platform mounting, which is consistent with the thicker boundary layer. The difference due to mounting was insignificant on the back, but lower pressures were obtained on the ends at zero yaw for the floor mounting. Data tabulated in the reference show that, for the platform mounting, the front vertical centerline is at stagnation pressure from the base to about 75

percent of the height. This was not true in the case of the floor mounting for which the centerline pressures started decreasing below the center.

As in the comparison of UW plate and ground plane mountings, data from the study Wind Pressure on Structures\* showed a more negative pressure on the left face at 15 degrees than at zero yaw with the platform, while the floor mounting showed no decrease. The decrease of vertical centerline pressures below the center of the front face of the NBS floor-mounted model is similar to decreases shown for  $H_B$  and  $H_C$  houses on all mountings in the UW and CWT tests.

### Cube and Prism Tests

In another series of wind tunnel tests performed in Denmark,<sup>†</sup> a cube and square-base prism (1:1:2.47) were included. Models were mounted on a tunnel side wall and tested at 65.5 ft/sec to determine the pressure distributions. Unfortunately, no pressure ports were placed on the cube centerlines. Integrated values of the normal coefficient for both cube and prism given in the report are plotted versus yaw angle in Figure 76.

For the prism, the lowest row of horizontal pressures on the windward faces showed lower pressures than were shown for the horizontal centerline; this is consistent with the NBS prism mounted on the tunnel floor. Stagnation pressures were possibly never attained on the cube. Zero-yaw horizontal-line pressures on the ends become less negative toward the rear of the face, which is in opposition to the results obtained by other experiments studied. Tests, with and without sandpaper, were run on the prism ahead of the model. When sandpaper was used, the tendency for end pressures to decrease toward the rear was lessened, indicating that the decrease is caused by a boundary layer condition.

Comparing the prism coefficients with those given in Figure 75, it is apparent that while windward-face values compare well, negative pressure-face values are different. Values for the cube show reasonable agreement with those obtained in UW and CWT tests on the front, but back pressures are quite different.

### State University of Iowa Tests on Block Forms

Among the numerous building forms tested at the State University of Iowa<sup>‡</sup> were blocks similar to those tested in the UW and CW Tunnels. Pressures were obtained on block forms mounted on a 2-by-3-foot plate in a 4-by-6-foot tunnel that was operated at 25 feet per second.

\*High L. Dryden, and George C. Hill, Wind Pressure on Structures, Scientific Papers of the Bureau of Standards, No. 523, Washington, D.C.

†J. O. V. Irminger, and Chr. Nkkentved, Wind-Pressure on Buildings, Experimental Researches, Denmark, 1930.

‡Ning Chien, Yin Feng, Hung-Ju Wang, and Tien-To Siao, Wind-Tunnel Studies of Pressure Distribution on Elementary Building Forms, Iowa Institute of Hydraulic Research, State University of Iowa, 1951.

The cube was 4:4:4 inches; other models were correspondingly larger. Pressure data are given in the form of pressure contours at 0.1 intervals in  $\frac{\Delta p}{q}$  for each face at 0, 45, and 90 degrees yaw. Normal force coefficients were determined at Sandia by using a planimeter to integrate the SUI contours. Inaccuracies of reproductions from which values were obtained, together with difficulties encountered in averaging these values, contributed errors of at least 5 percent. Symmetry was forced where it should have been present. Pressure contours did not indicate stagnation pressure at the center of the cube at zero yaw; stagnation was obtained at this point in the Sandia tests.

In Table V the Iowa University data have been included with CWT and UW data for various mountings. Negative-pressure face coefficients for the Iowa data are consistently more negative. Table VI gives drag coefficients from various experiments for 0 and 90 degrees yaw. A study of these tables indicates that there still remains the problem of assessing the nature of differences obtained by different experimenters and of determining the correct low Mach number coefficients, even for the orientations which give the least complex pressure distributions.

The values of drag coefficient given for a related model, a freely exposed square flat plate, vary from reference to reference. For this relatively simple model, the coefficients found in a literature survey varied from 1.05 to 1.33, which is the same variation given for the cube in Table VI. The two drag components were not separated in the references used, so it is not known wherein the detailed differences lie.

#### Pressure Distribution for a Flat Plate

The theoretical pressure distribution on the windward side of a flat plate, calculated by the method given by Streeter,\* is shown in Figure 77. This theory gives a zero pressure coefficient at the edge. The experimental pressure distribution on the windward face of an infinite flat plate with no ground mounting† is also given in Figure 77. Since the center of the cube used in Sandia tests was at stagnation pressure, its horizontal centerline-pressure distribution, also shown in Figure 77, should most nearly correspond to that of the flat plate. Values shown are from CWT data at  $M = 0.2$ . Much lower negative pressures on the leeward side of a model without mounting evidently cause the front-face pressures to decrease more rapidly as the edge is approached than is possible on a ground-mounted model. It is interesting to note that there is a close correlation between theoretical values for a free flat-plate model and experimental values for a mounted cubical model.

\*Victor L. Streeter, Fluid Dynamics, McGraw-Hill Book Co., New York, 1948.

†A. Fage, and F. C. Johansen, On the Flow of Air Behind an Inclined Flat Plate of Infinite Span, Proc. Roy. Soc., A Vol. 116, London, 1927.



## CH IV -- CONCLUSIONS AND RECOMMENDATIONS

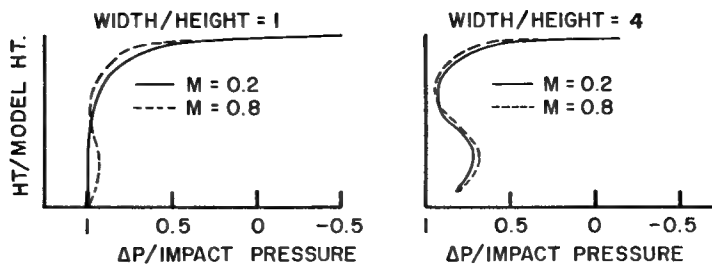
### Conclusions

6

Voluminous pressure data were obtained on three block forms for a range of Mach number (0.066 to 0.8), Reynolds number ( $0.28 \times 10^6$  to  $4 \times 10^6$ ), and yaw angle (0 to 90 degrees). Representative data are presented. The remainder of the data is available, some in reduced form and some as raw data. In spite of experimental difficulties which leave some of the values and effects obtained open to question, much information was gained from the experiments. The variation of normal force coefficients with Reynolds number and yaw angle has been established; variation with Mach number of windward-face normal-force coefficients is evaluated.

Among the values and effects left open to question by the tests are: the absolute value of normal force coefficients, the effect of Mach number on leeward face coefficients for blocks with width greater than height, model-depth effect on leeward-face coefficients, and the effect of the extent of ground mounting, including boundary layer influences. Large scatter in negative pressure data and unassessed ground mounting influences, which cannot be separated from the other factors, precluded analysis of the foregoing. A variation of mounting extent in the low Mach number tests affected pressure on larger models but did not affect the pressures on the cube. The forward mounting extent was not varied during the high Mach number tests, and leeward mounting variation was only partial. Thus we are left with the question: was the mounting large enough to contain the entire disturbed flow field? The data were insufficient to allow adequate analysis of the effects the mounting had on the data obtained.

Although windward-face coefficients show less variation within a test series and between results obtained by different researches than do negative pressure coefficients for other faces, application of the values obtained on the front face may be limited in some situations, by vortex formation forward of the bodies. Vortex formation is manifest in some of the vertical center-line profiles, as indicated in the following sketch. These profiles are influenced by Mach number, house width, and mounting extent.



A vortex appeared to form forward of the cube at high Mach numbers (0.65 to 0.8) and forward of models with width to height ratio greater than unity at all test Mach numbers. Since the boundary layer on the mounting is no doubt the determining factor in the vortex formation, the ratio of model height to boundary layer thickness may be the scaling factor appropriate for application to full scale situations. Although these forward vortices would be expected to influence leeward faces, negative pressure data was not of sufficient accuracy to allow analysis.

From the information gained in the tests, the following positive conclusions can be drawn:

1. Over the range of  $10^6$  to  $4 \times 10^6$  there is no significant effect of Reynolds number on loading of a block form or on surrounding flow characteristics.
2. Normal-force coefficients for an unyawed windward face vary with Mach number as the ratio of impact pressure to dynamic pressure.
3. Normal-force coefficients on the leeward face of a cube are independent of Mach number; this is consistent with compressible flow theory.
4. Variation of drag coefficient with Mach number for models oriented with the large face normal to the wind can be predicted theoretically from consideration of compressibility effects, as accurately as leeward-face force coefficients have been determined experimentally.
5. Force on a square face in the windward direction shows no block-depth effect up to a width depth ratio of 1:4.
6. Average experimental, windward horizontal-centerline pressure on a plate-mounted cube is greater than the experimental value for a free flat plate.

Significant among the applications of the foregoing conclusions is the fact that high subsonic Mach number drag coefficients for block forms with the large face windward can be obtained theoretically from incompressible, normal-force coefficients with sufficient accuracy for use in predicting steady-state drag coefficients for full-scale blast application. However, values for the incompressible normal-force coefficients are not well established.

## Recommendations

Since, for blast-loading predictions, models of interest will be on the ground surface, a study of the effects of mounting, rather than an attempt to eliminate such effects in wind tunnel tests, is in order. The influence of extensive ground mountings should be checked for Mach numbers higher than those included in the University of Wichita tests. A mounting of sufficient extent, to the rear and side of the model to assure the flow characteristics of an infinite plane, should be used to secure more reliable negative pressure force coefficients than have been obtained. The mounting should have good leading-edge characteristics to eliminate the possibility of a leading-edge separation bubble influencing the vortex formation forward of the model. Vortex formation forward of larger models should be studied further. Smoke or other indicators should be used to trace the entire flow pattern. The extent of the mounting forward of the model and the surface roughness should be varied to change the thickness and characteristics of the boundary layer and thus determine how boundary layer influences the vortex. Also, the influence of the forward vortex on the pressures on other block faces could be determined in this way. The size of the model might also be varied to change the ratio of boundary-layer thickness. An attempt should be made to correlate normal-force coefficients with the ratio of boundary-layer thickness to block height and the ratio of block height to block width. The foregoing experiments should then be correlated with a study of ground boundary-layer data from full-scale blast experiments to determine a method of applying wind-tunnel data to full-scale blast experiments, provided data are not masked by transient-drag phenomena.

It would be of interest to check the influence of mounting on the force coefficients of the side faces turned at a small angle into the wind.

In any future tests, pressure ports should be placed as close as is practicable to the leading-edge of the windward faces on a representative model. Pressures should be taken throughout the range of yaw angles to determine flow characteristics near the separation point.

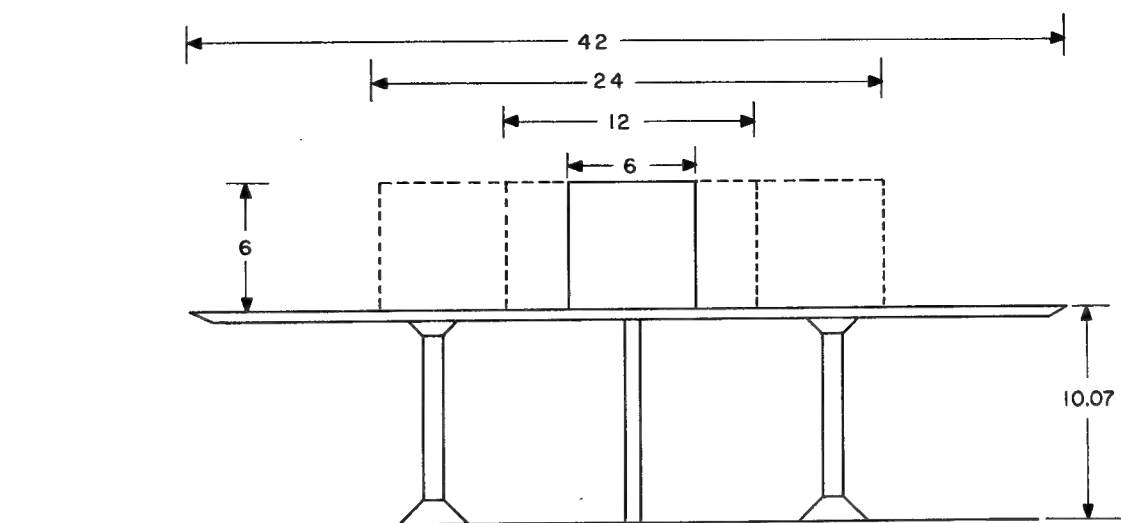
TABLE V  
Normal Force Coefficients

Iowa University Tests					CWT M = 0.2 (Plate)					Plate plus Extension
Yaw Angle*    0°        45°        90°					Yaw Angle*    0°        45°        90°					0°
H <sub>A</sub>	F	+0.74	+0.34	-0.80	H <sub>A</sub>	F	+0.791	+0.425		+0.806
	B	-0.59	-0.66	-0.80		B	-0.460	-0.468		-0.472
	L	-0.80	+0.34	+0.73		L	-0.558	+0.424		-0.619
	R	-0.80	-0.66	-0.58		R	-0.556	-0.434		-0.577
H <sub>B</sub>	F	+0.74	+0.40	-0.74	H <sub>B</sub>	F	+0.756	+0.414	-0.556	+0.743
	B	-0.63	-0.76	-0.74		B	-0.396	-0.532	-0.546	-0.531
	L	-0.66	+0.23	+0.72		L	-0.560	+0.345	+0.795	
	R	-0.66	-0.64	-0.23		R	-0.540	-0.396	-0.164	
H <sub>C</sub>	F	+0.68	+0.35	-0.36	H <sub>C</sub>	F	+0.740	+0.434	-0.278	+0.738
	B	-0.65	-0.76	-0.36		B	-0.395	-0.495	-0.286	-0.482
	L	-0.74	+0.20	+0.65		L	-0.496	+0.295	+0.779	-0.602
	R	-0.74	-0.70	-0.24		R	-0.492	-0.400	-0.136	-0.588
UW (Ground Plane) M ≈ 0.2					UW M ≈ 0.2 (Plate)					Plate plus Extension
Yaw Angle*    0°        45°        90°					Yaw Angle*    0°        45°        90°					0°
H <sub>A</sub>	F	+0.816	+0.440		H <sub>A</sub>	F	+0.815	+0.429		+0.798
	B	-0.481	-0.484			B	-0.436	-0.429		-0.484
	L	-0.647	+0.409			L	-0.584	+0.398		-0.609
	R	-0.659	-0.470			R	-0.594	-0.443		-0.640
H <sub>B</sub>	F	+0.721	+0.445	-0.579	H <sub>B</sub>	F	+0.723	+0.440	-0.509	+0.733
	B	-0.473	-0.581	-0.594		B	-0.423	-0.513	-0.555	-0.462
	L	-0.723	+0.321	+0.793		L	-0.619	+0.325	+0.782	
	R	-0.718	-0.462	-0.160		R	-0.625	-0.414	-0.111	
H <sub>C</sub>	F	+0.644	+0.394	-0.274	H <sub>C</sub>	F	+0.706	+0.415	-0.273	+0.694
	B	-0.518	-0.645	-0.285		B	-0.434	-0.530	-0.304	-0.432
	L	-0.700	-0.222	+0.810		L	-0.517	+0.304	+0.785	
	R	-0.710	-0.528	-0.143		R	-0.513	-0.393	-0.121	

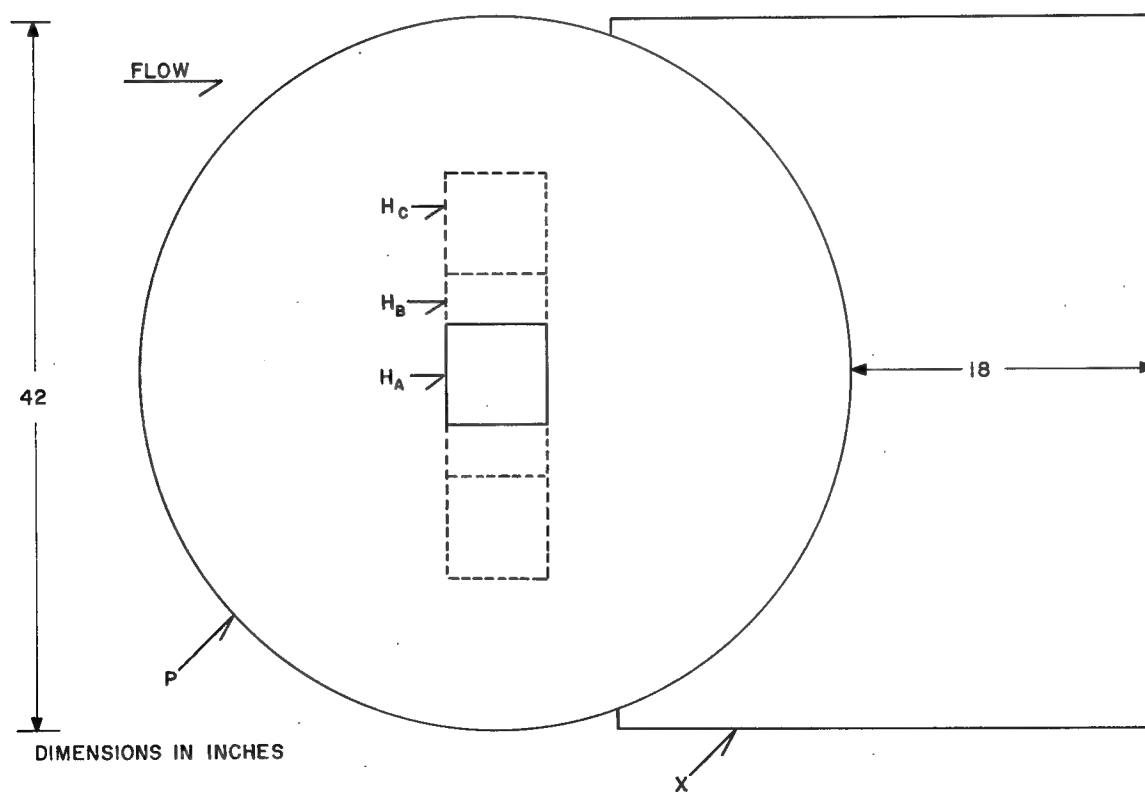
\*F = front; B = back; L = left; R = right

TABLE VI  
Drag Coefficients

Test	$\psi = 0^\circ$			$\psi = 90^\circ$	
	H <sub>A</sub>	H <sub>B</sub>	H <sub>C</sub>	H <sub>B</sub>	H <sub>C</sub>
UW (plate)	1.22	1.14	1.14	0.89	0.91
UW (plate + X)	1.25	1.19	1.13	-	-
UW (ground plane)	1.26	1.19	1.16	0.95	0.95
CWT (plate)	1.22	1.15	1.14	0.96	0.92
CWT (plate + X)	1.24	1.27	1.12	-	-
SUI	1.33	-	-	0.95	0.89
Denmark	1.05	-	-	-	-



VIEW LOOKING DOWNSTREAM



DIMENSIONS IN INCHES

TOP VIEW

Fig. 1 -- Sketch of mounting plate showing house installations and extension plane

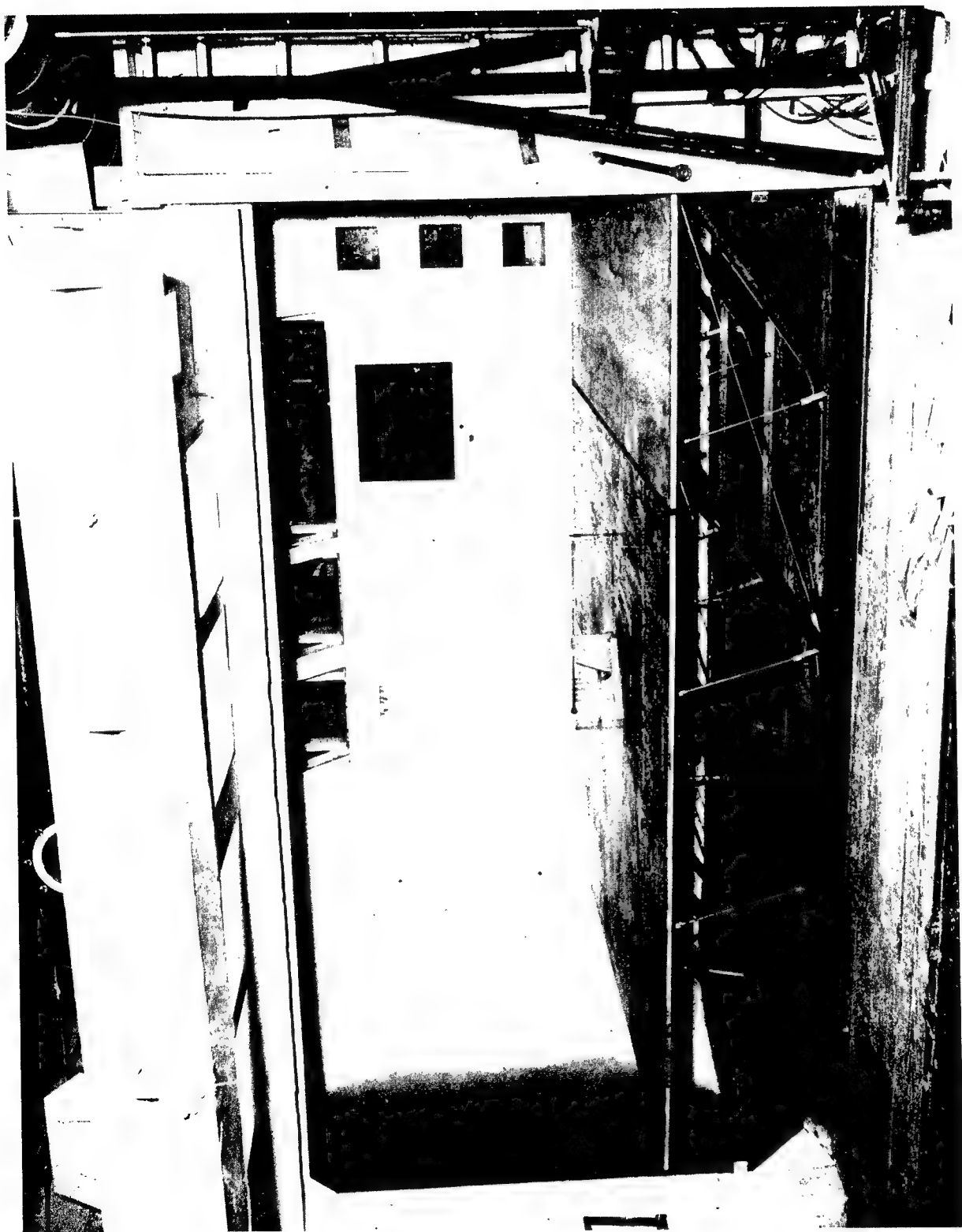


Fig. 2 -- Plate with extension ( $H_B$  block installed)

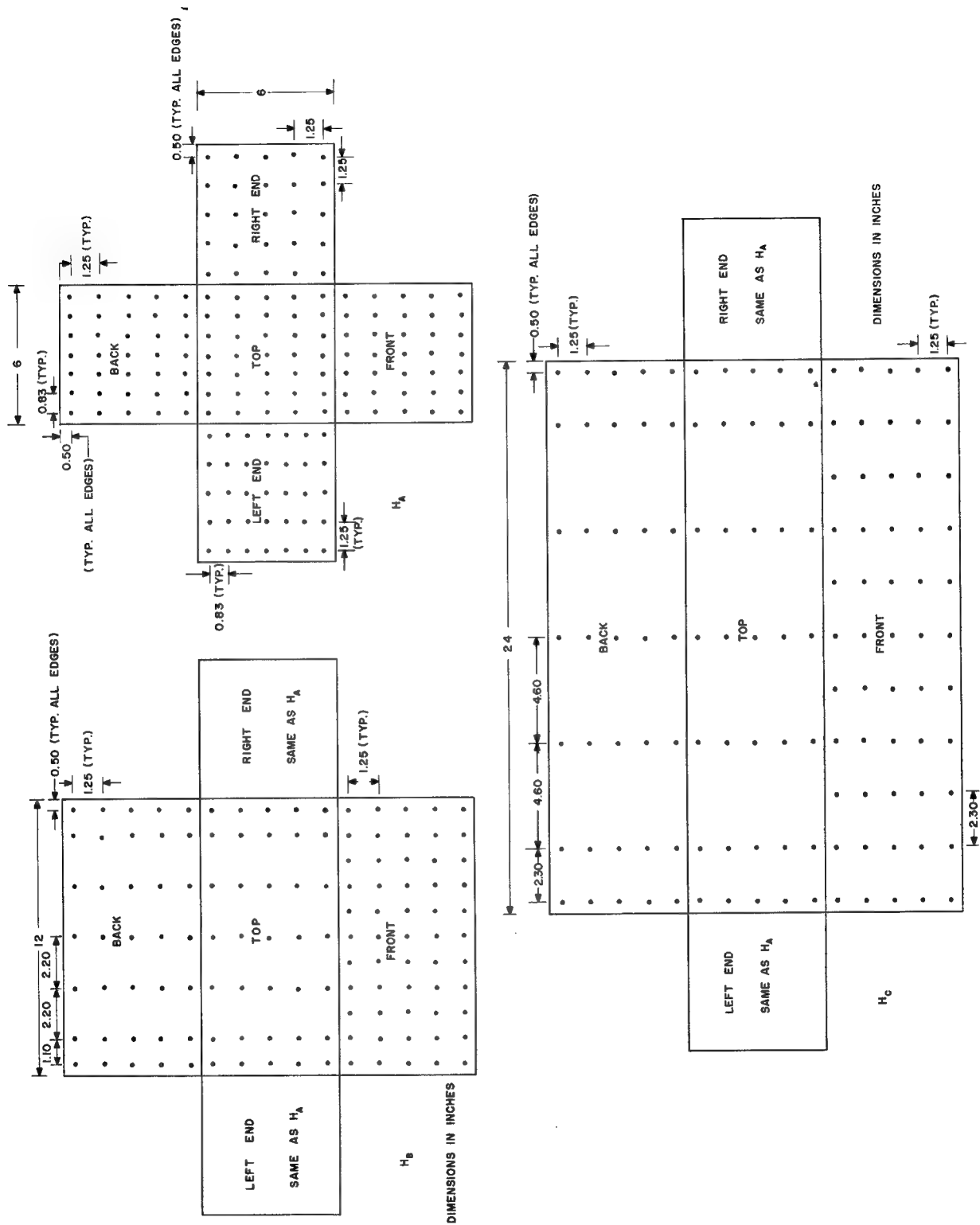


Fig. 3 -- Orifice locations on block forms, developed views

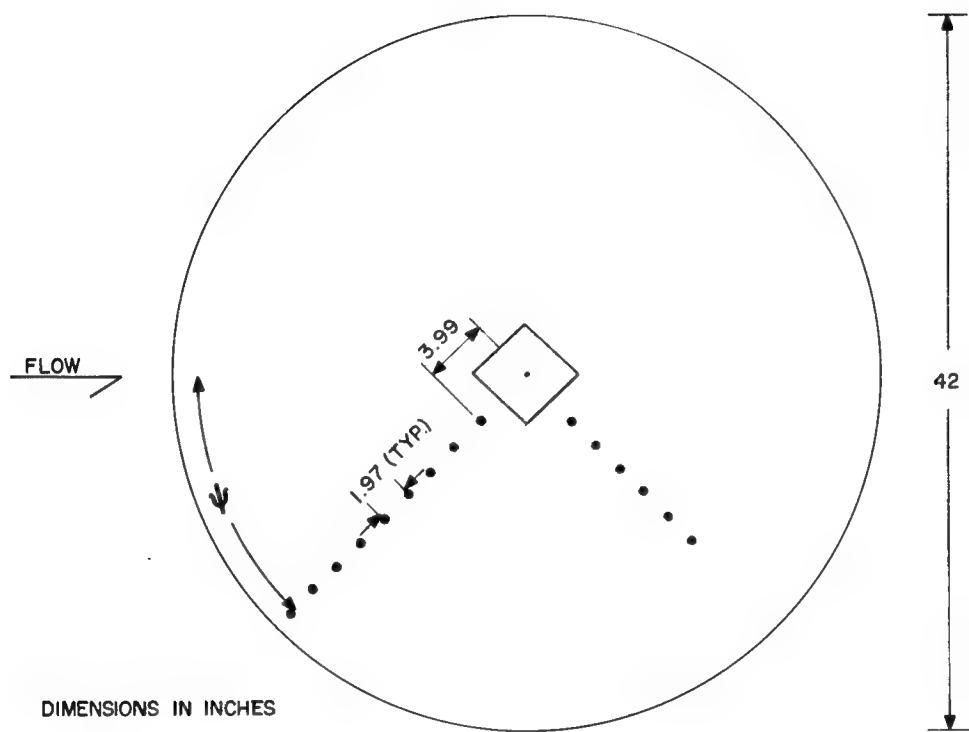


Fig. 4 -- Surface orifice locations on plate shown with  $H_A$  block yawed





Fig. 5 -- Ground plane with yawhead installed on disk

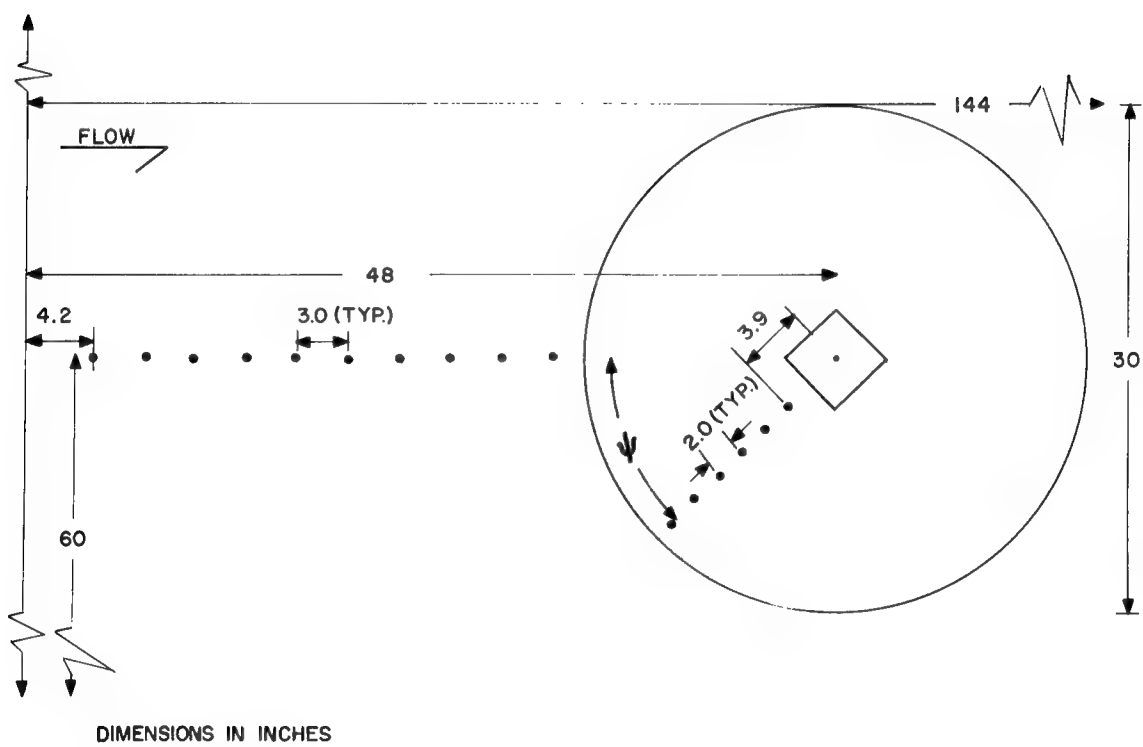


Fig. 6 -- Surface orifice locations on ground plane shown with  $H_A$  block yawed

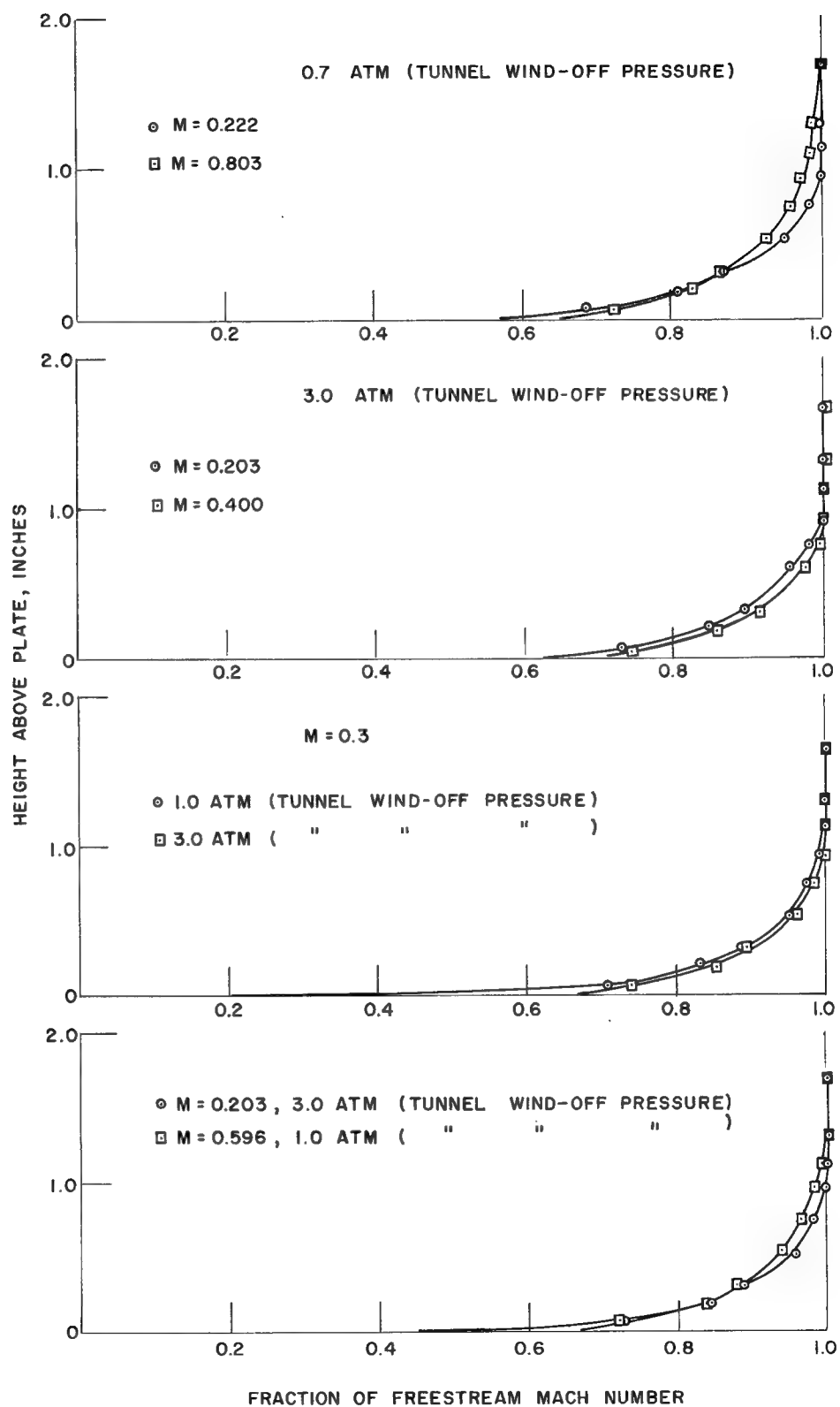


Fig. 7 -- CWT boundary layer profiles on plate mounting

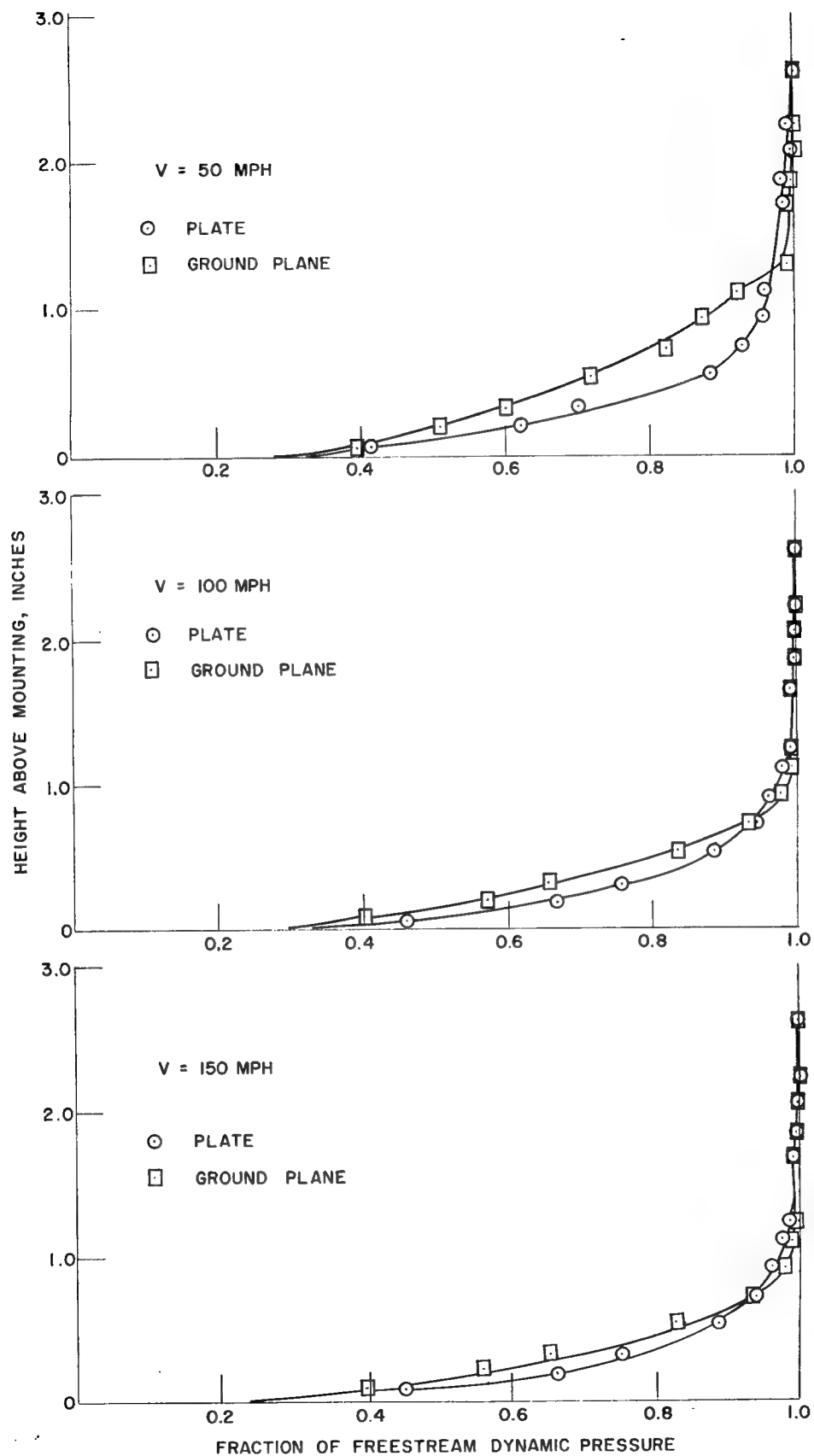


Fig. 8 -- Boundary layer profiles in the UW tunnel

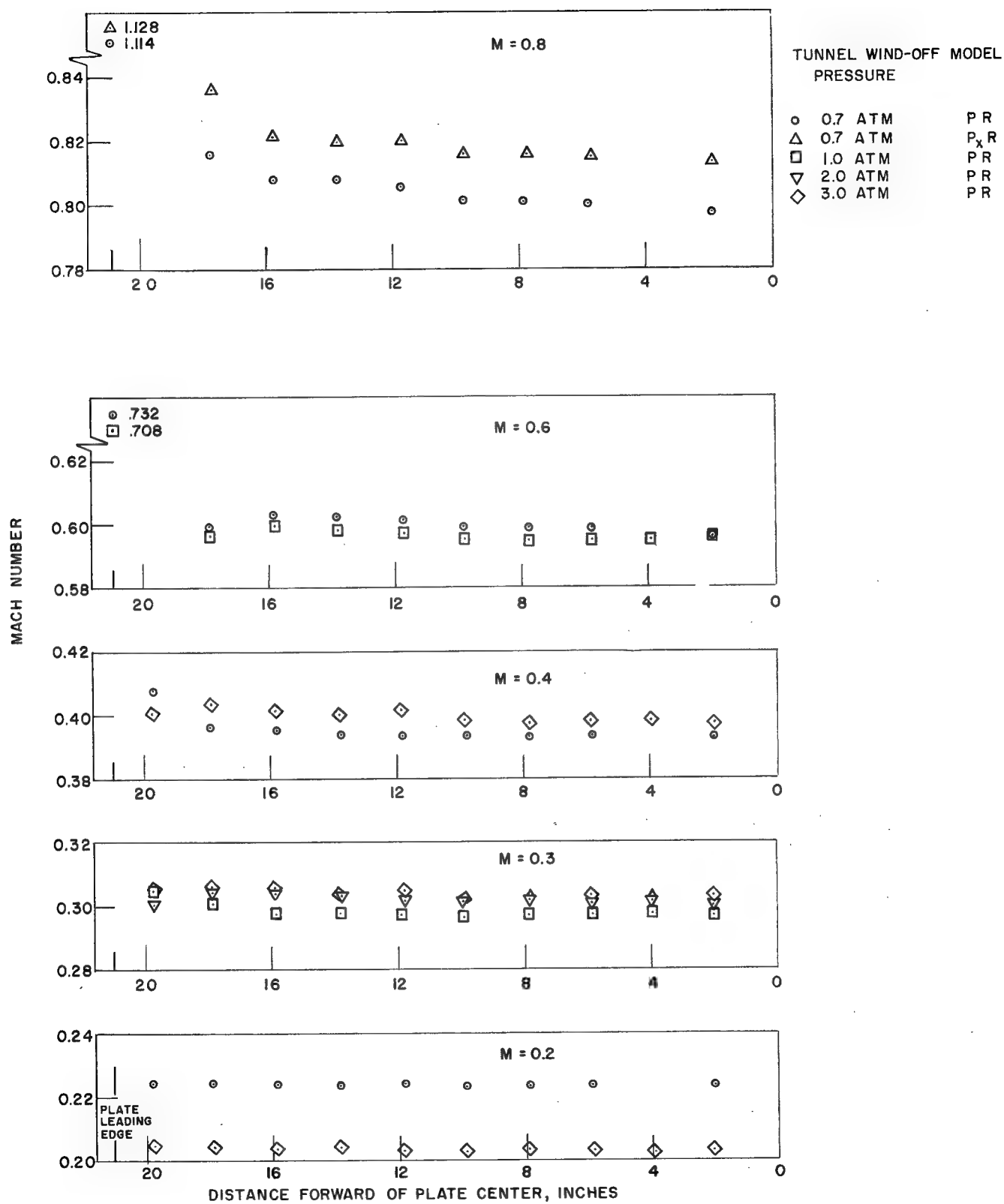


Fig. 9 -- Mach number distribution forward of CWT plate center without model installed

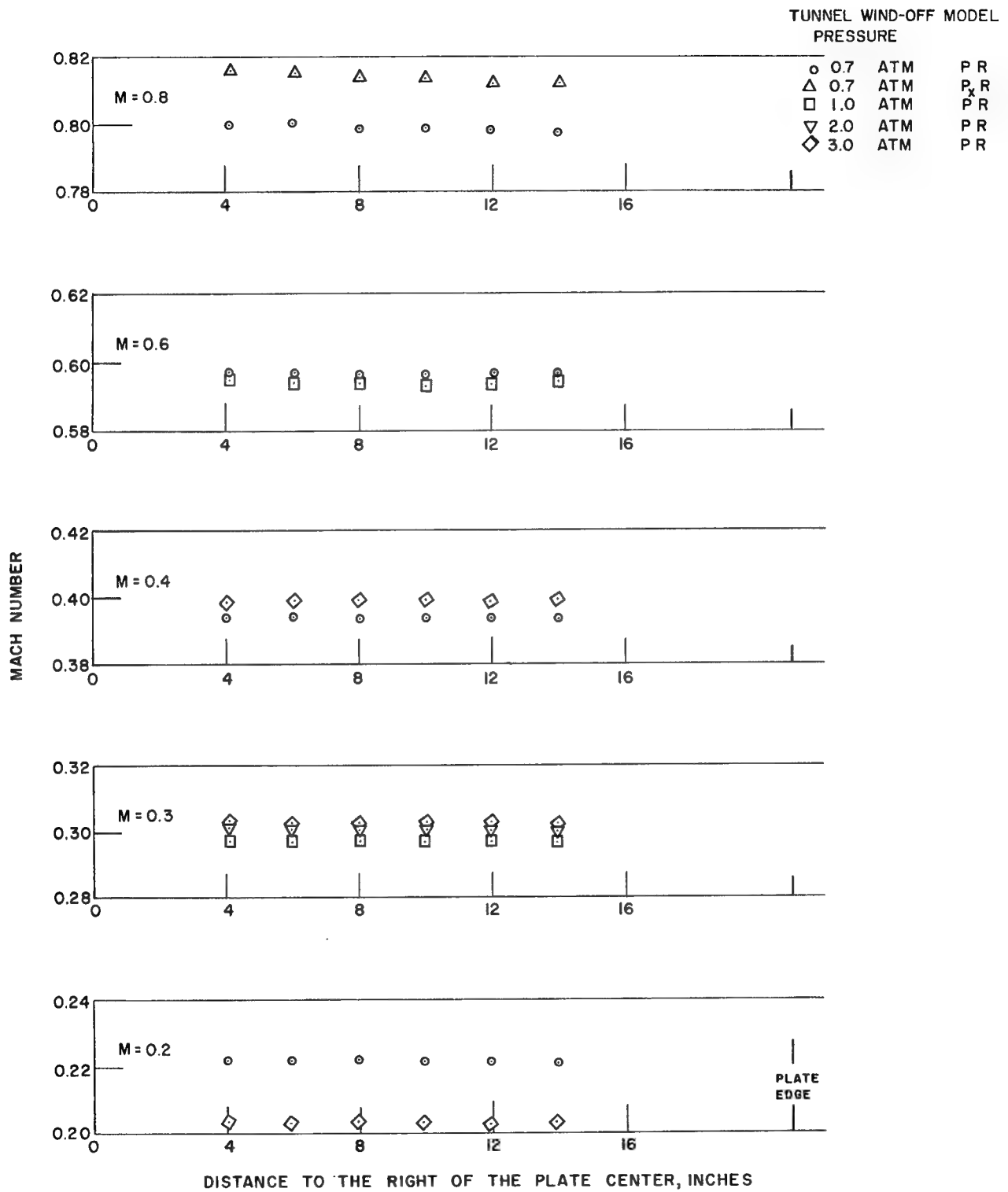


Fig. 10 -- Mach number distribution to the right of CWT plate center without model installed

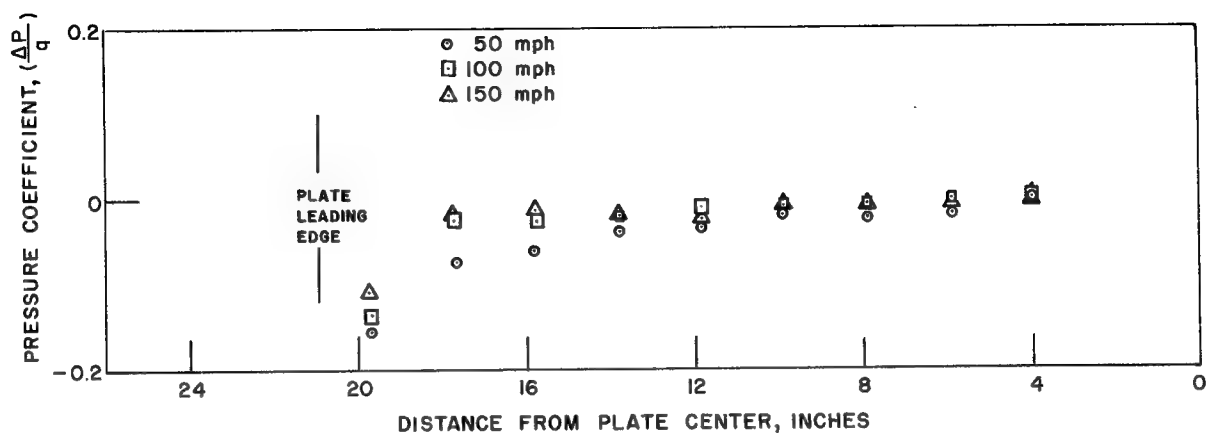


Fig. 11 -- Pressure distribution forward of plate center without model installed in the UW tunnel

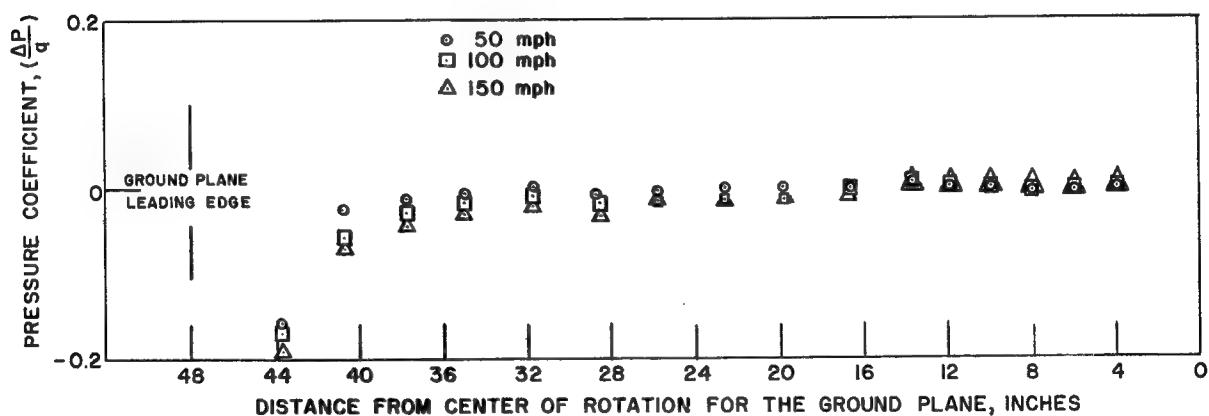


Fig. 12 -- Pressure distribution on the ground plane forward of center of rotation without model installed in the UW tunnel

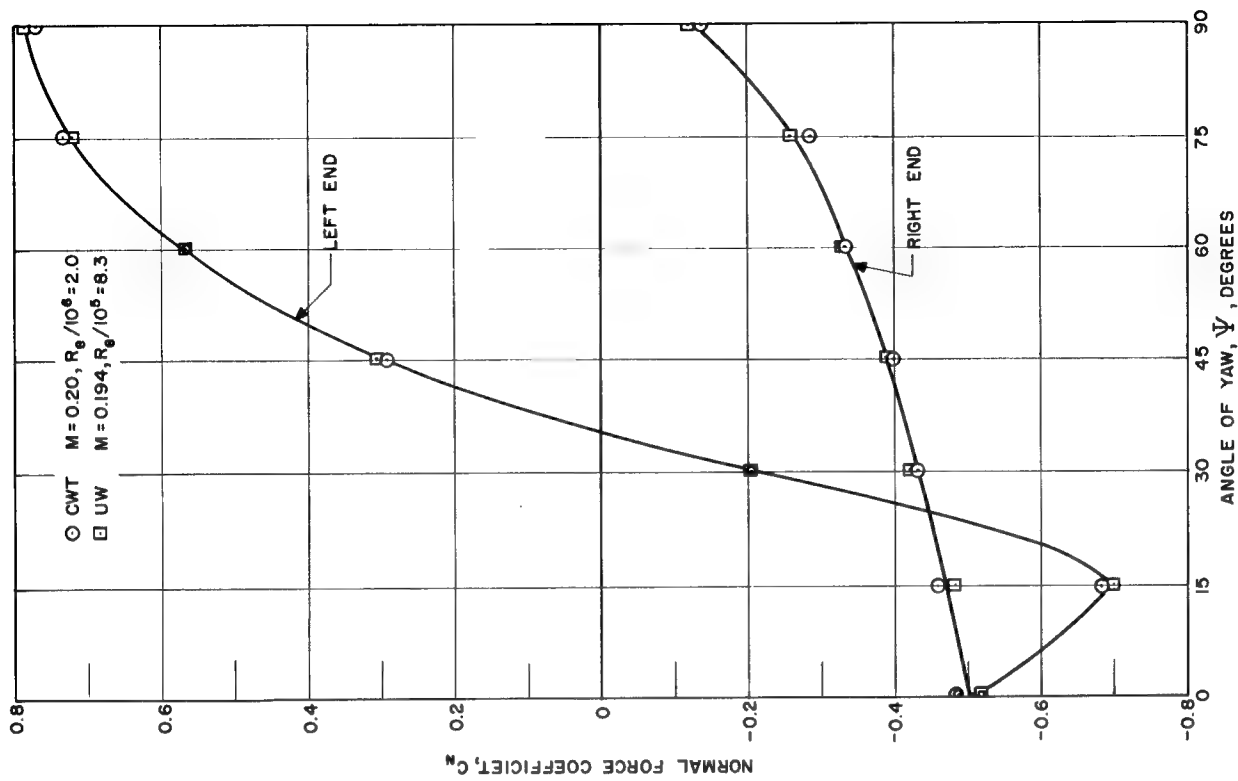
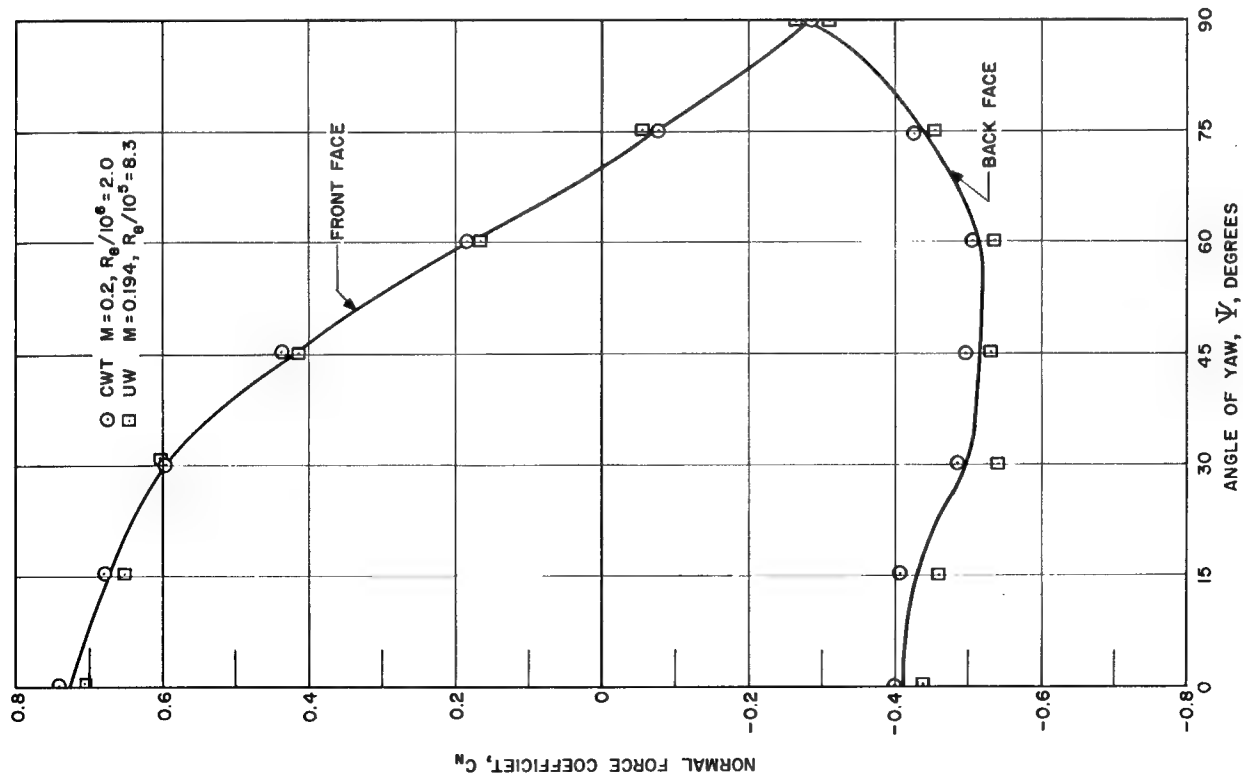


Fig. 13 -- Comparison of normal force coefficients for  $H_{CP}$  at  $M = 0.2$  obtained in two wind tunnels



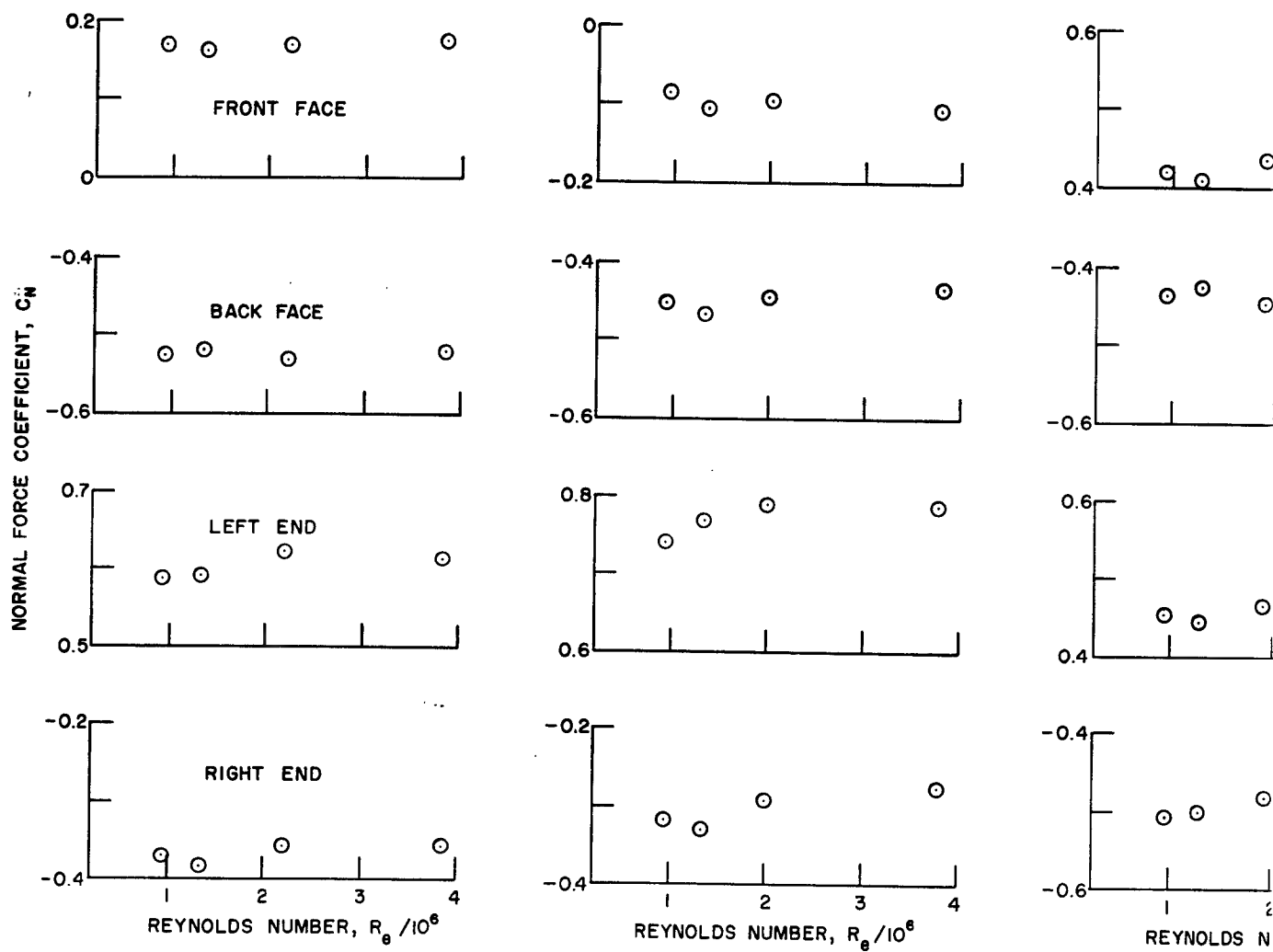
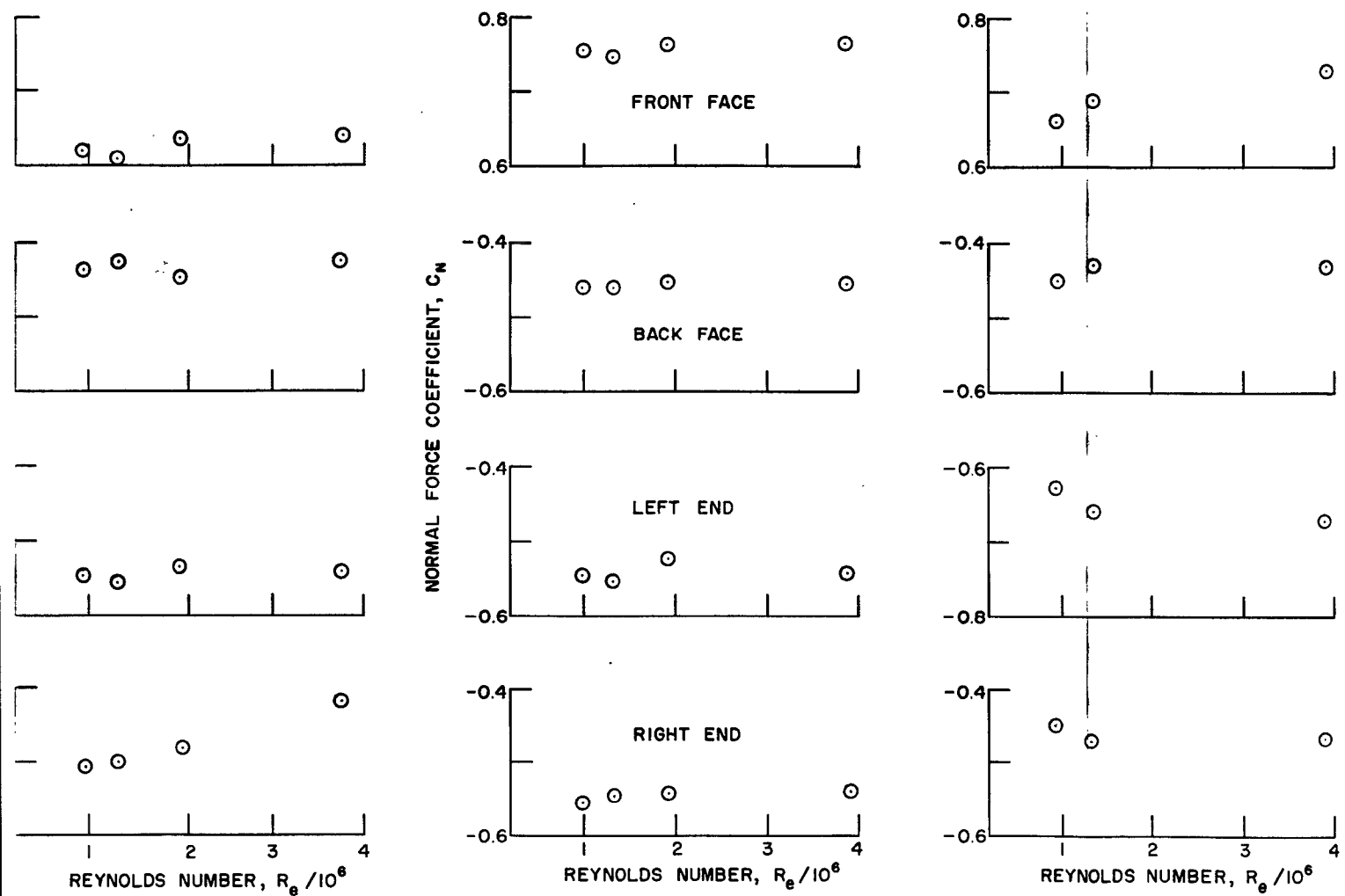


Fig. 14 -- Variations of  $C_n$  with Reyno



Variations of normal force coefficient with Reynolds number

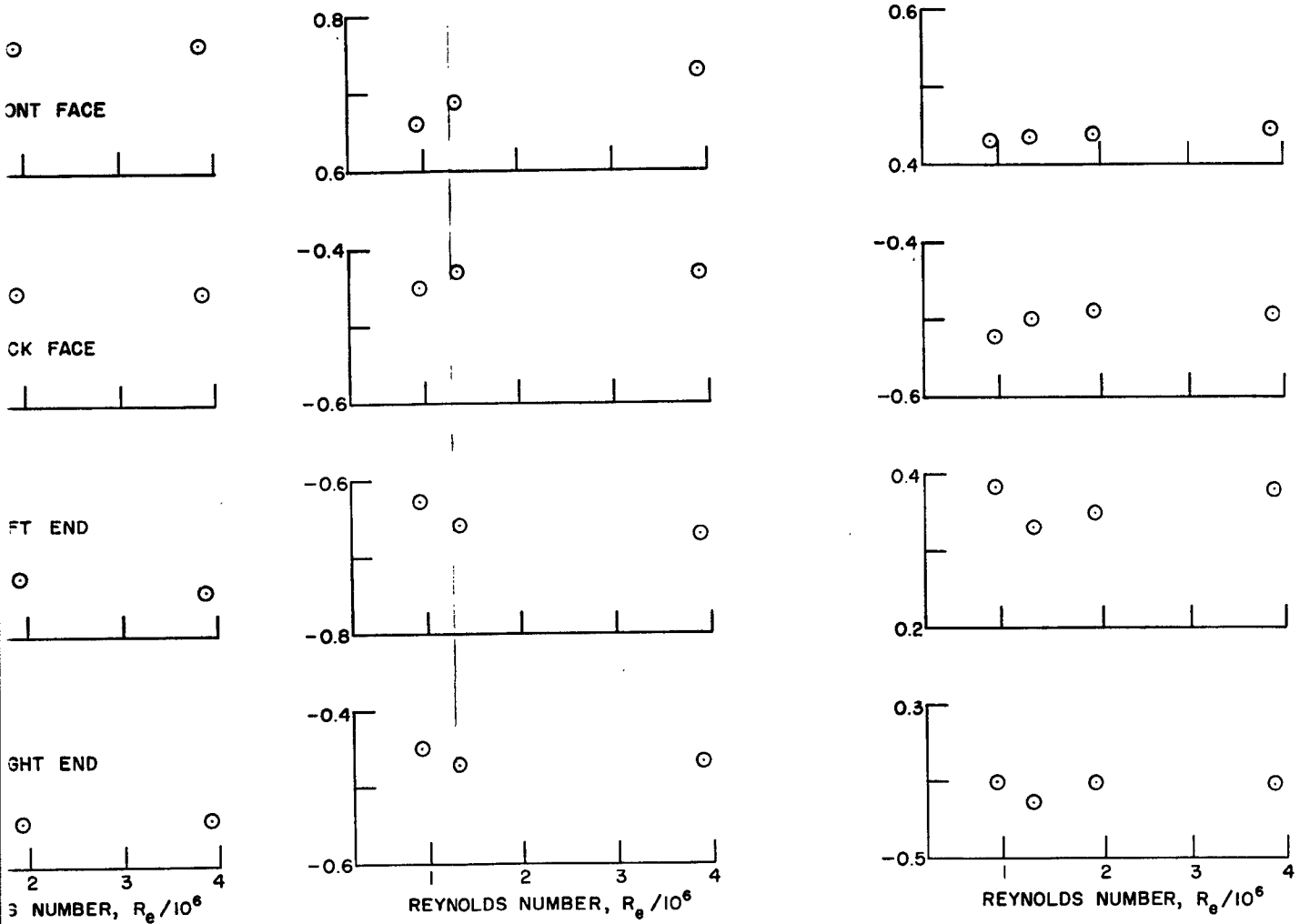


Fig. 15 -- Variation of normal force coefficient with Reynolds number for H<sub>A</sub>P at  $M = 0.4$ ,  $\psi = 45^\circ$

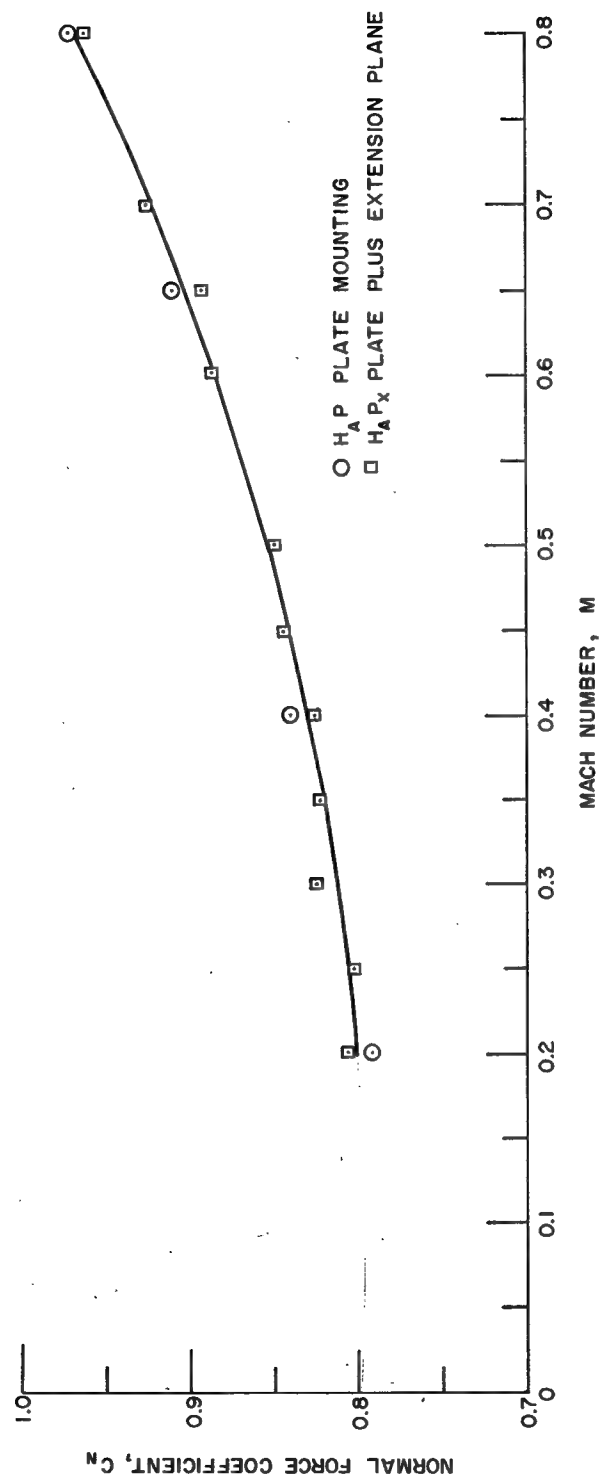


Fig. 16 -- Normal force coefficient on  $H_A$  front face at zero yaw versus Mach number at constant Reynolds number

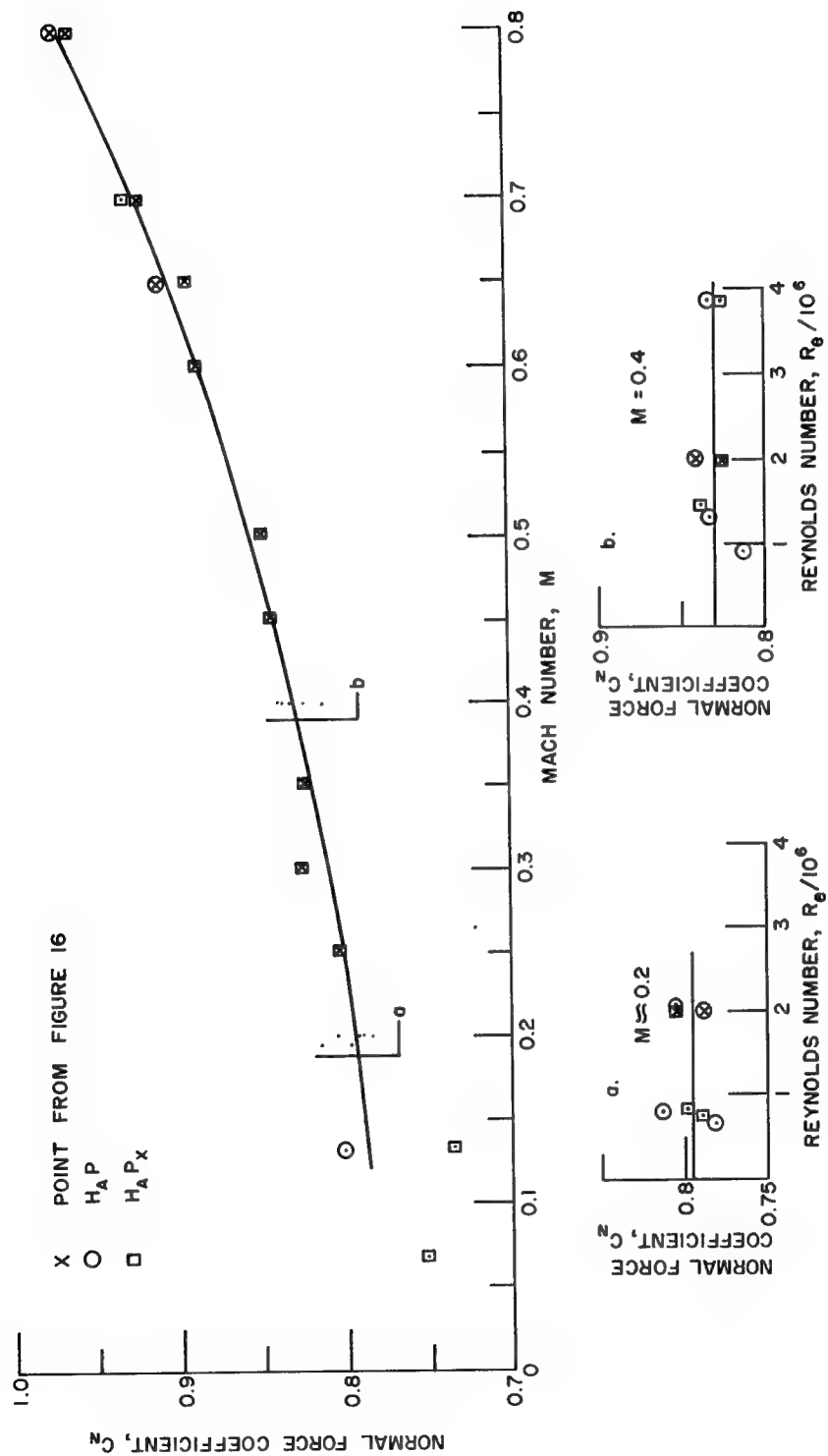


Fig. 17 -- Normal force coefficient on  $H_A$  front face at zero yaw versus Mach number for various Reynolds numbers

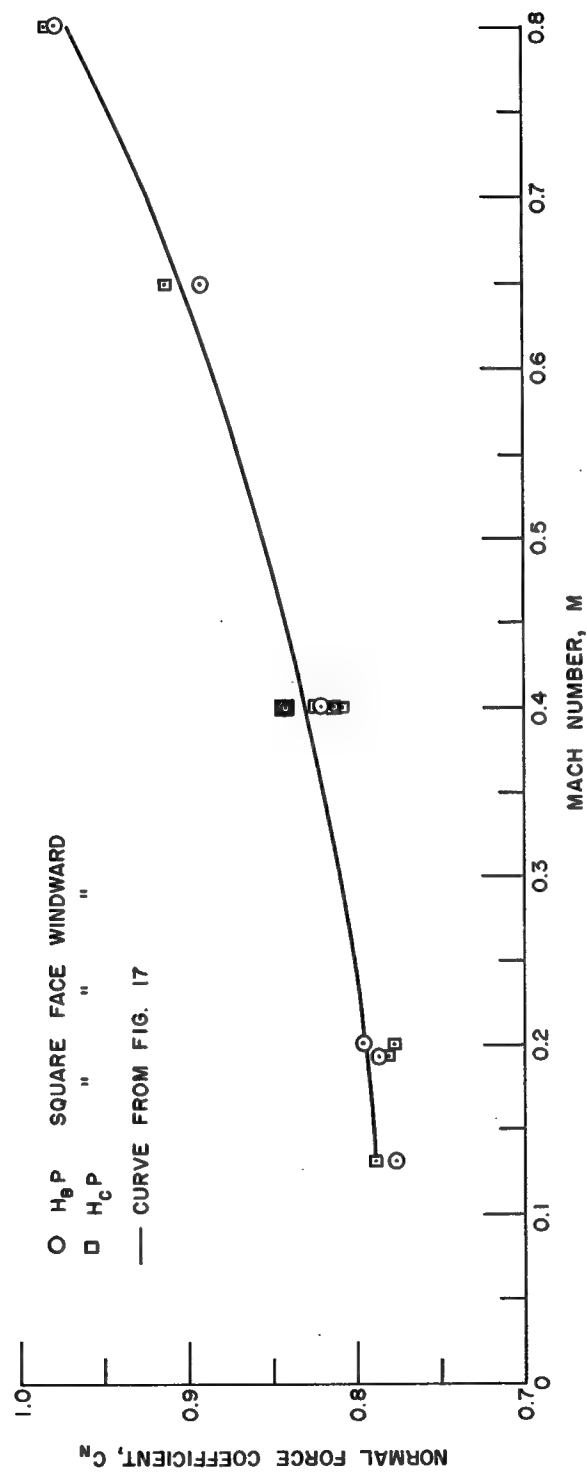


Fig. 18 -- Normal force coefficient on square face in the windward direction,  $\psi = 90^\circ$

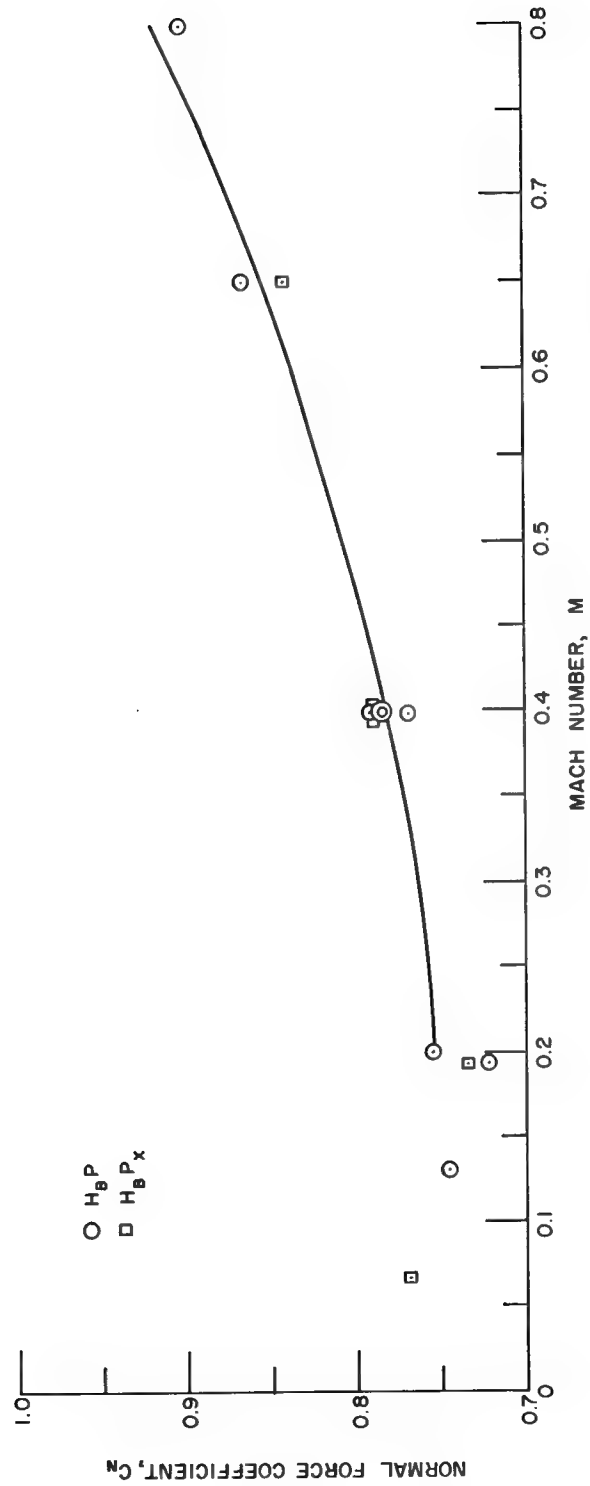


Fig. 19 -- Normal force coefficient on  $H_B$  front face at zero yaw versus Mach number  
(various Reynolds numbers)

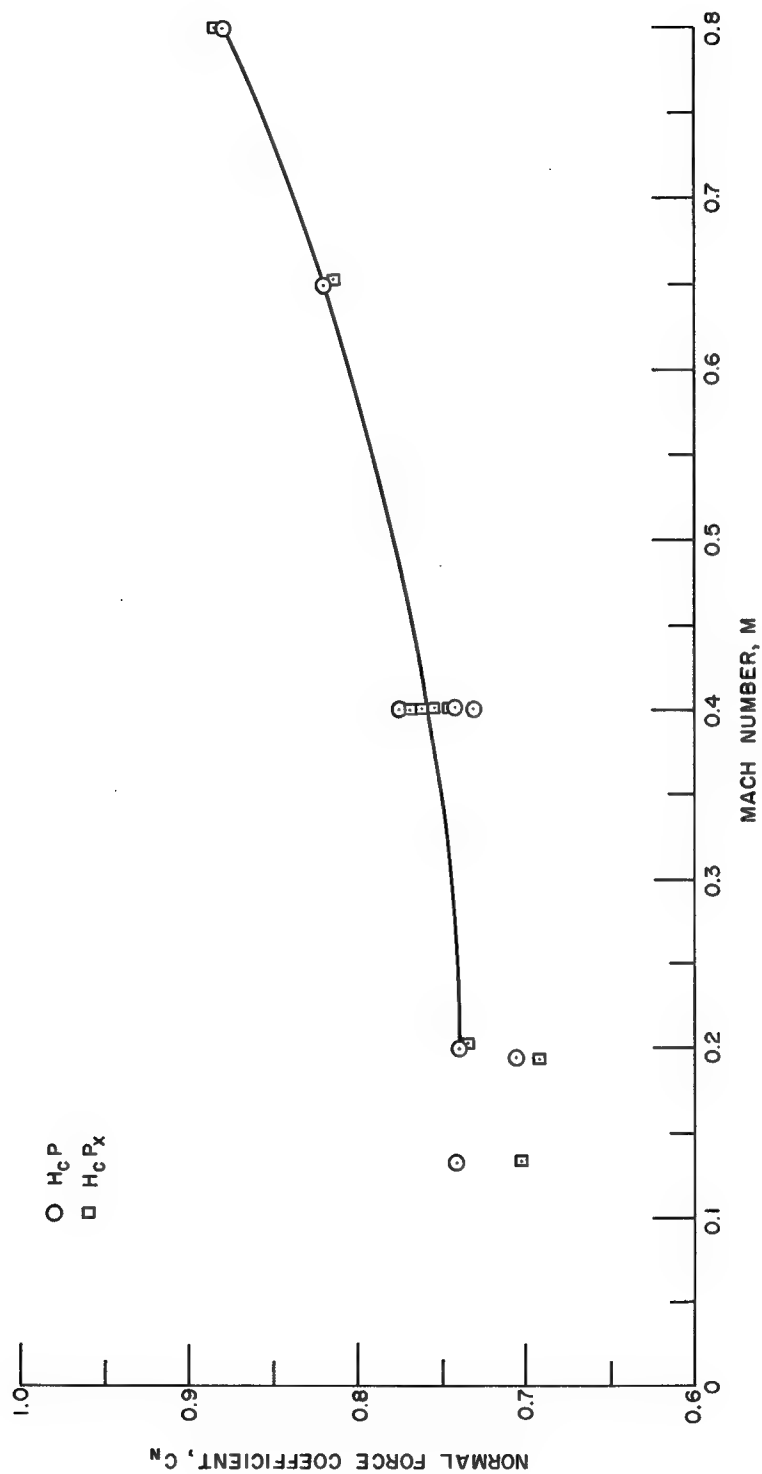


Fig. 20 -- Normal force coefficient on HC front face at zero yaw versus Mach number  
(various Reynolds numbers)



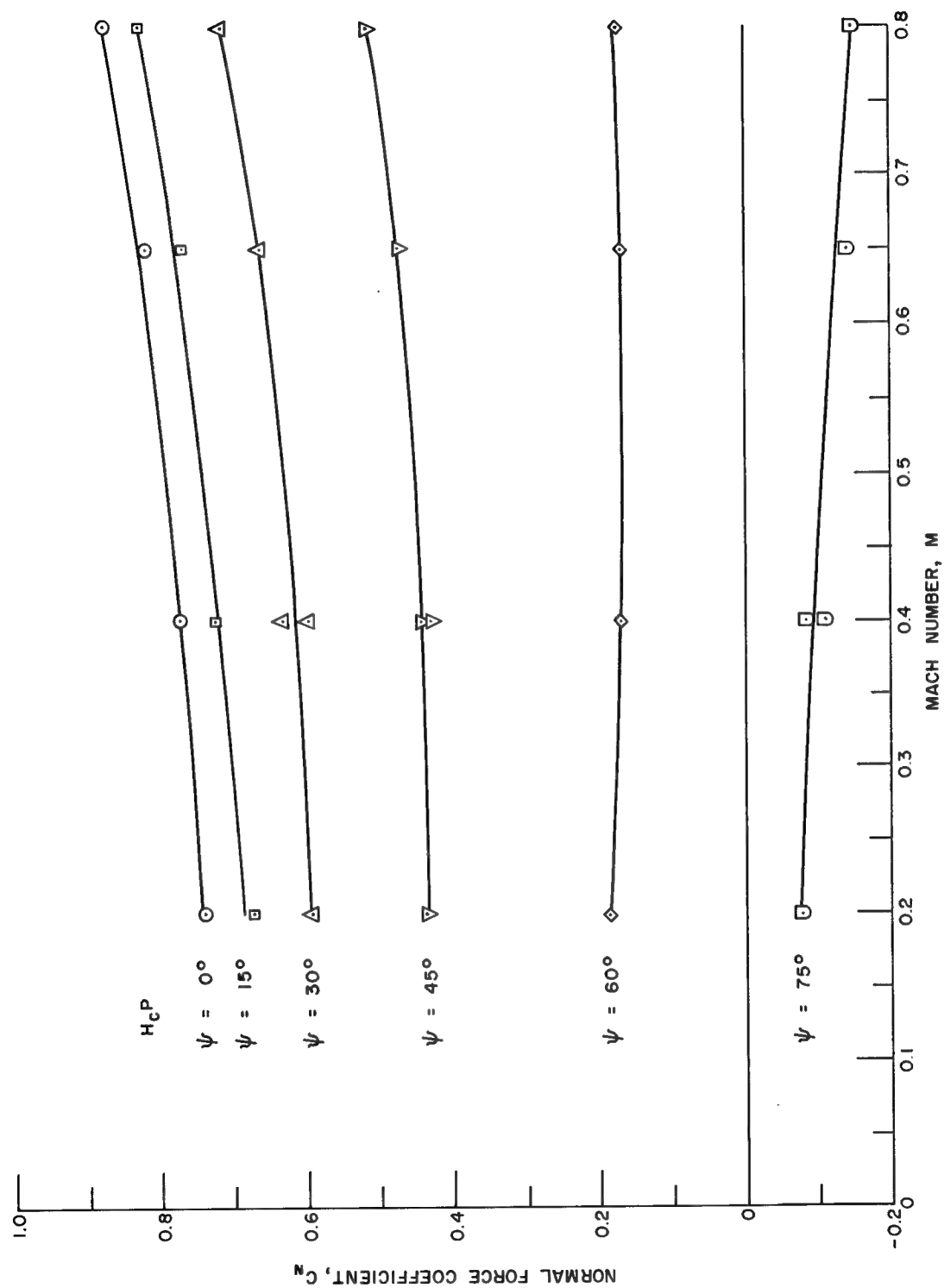


Fig. 21 -- Variation of  $H_{CP}$  front face normal force coefficient with Mach number, yaw angle as a parameter

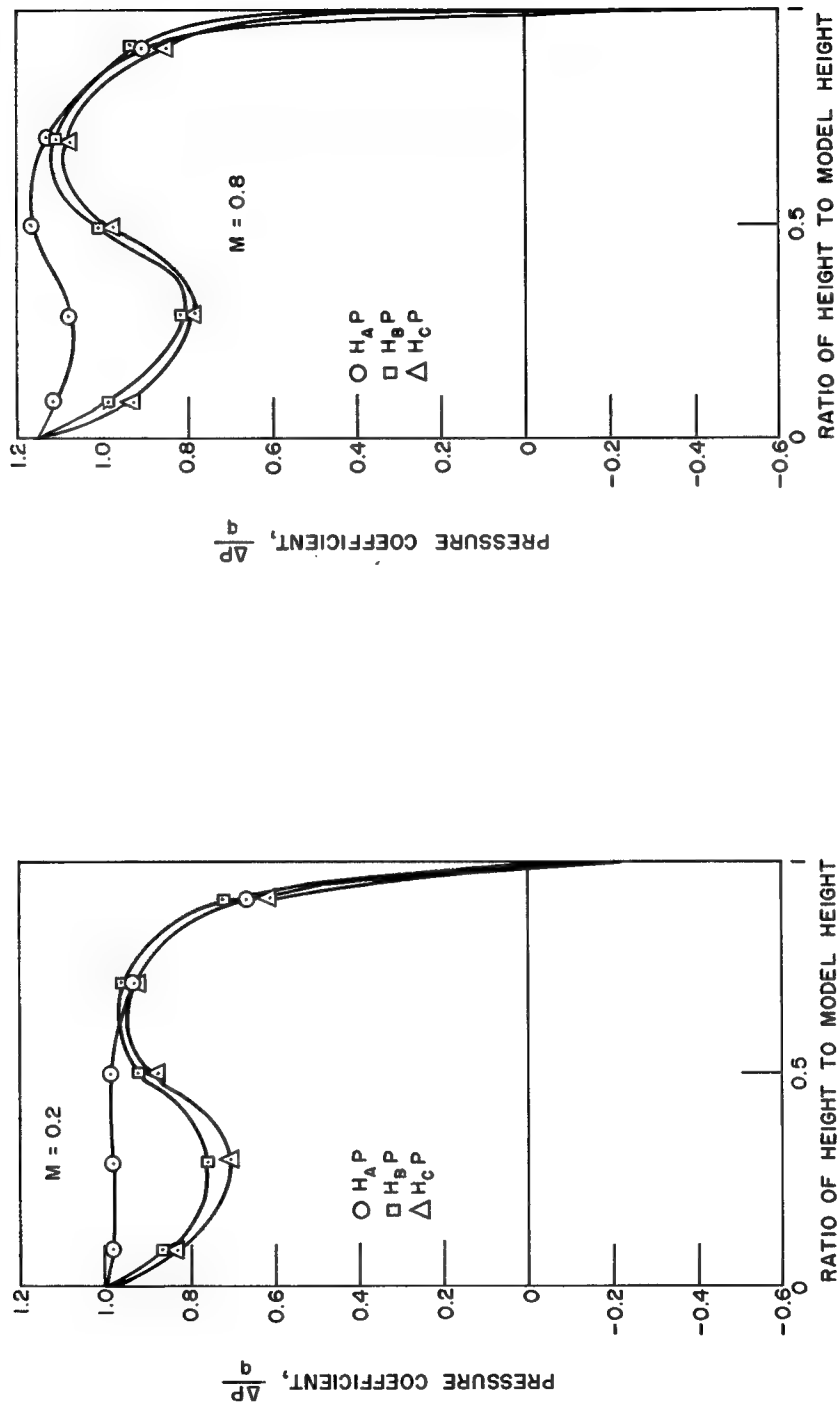


Fig. 22 -- Front face vertical centerline pressure profiles at  $M = 0.2$  and  $M = 0.8$ , block form as a parameter, Reynolds number is constant,  $\psi = 0^\circ$

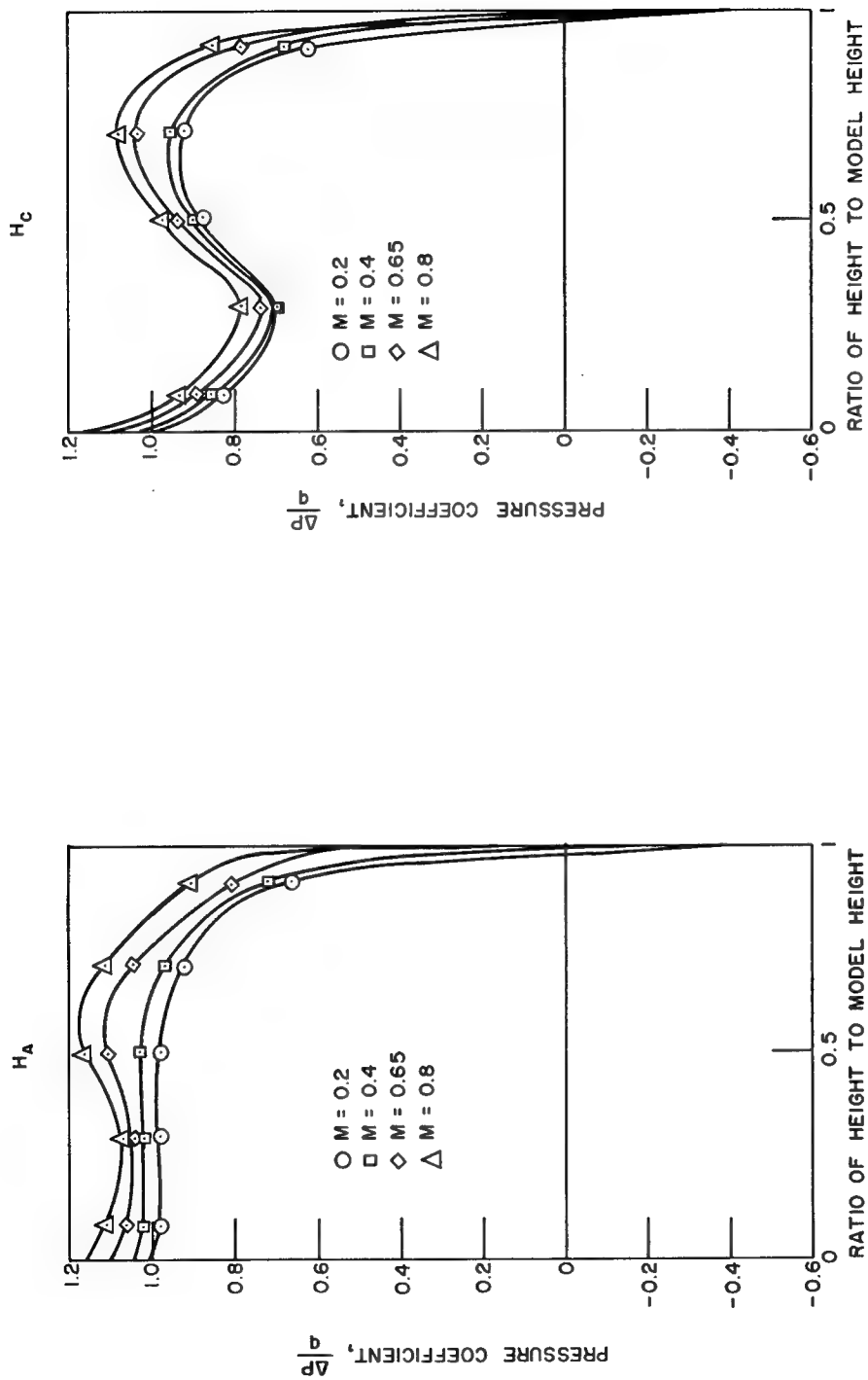


Fig. 23 -- Front face vertical centerline pressure profiles for  $H_A$  and  $H_C$ , Mach number as a parameter, Reynolds number is constant,  $\psi = 0^\circ$

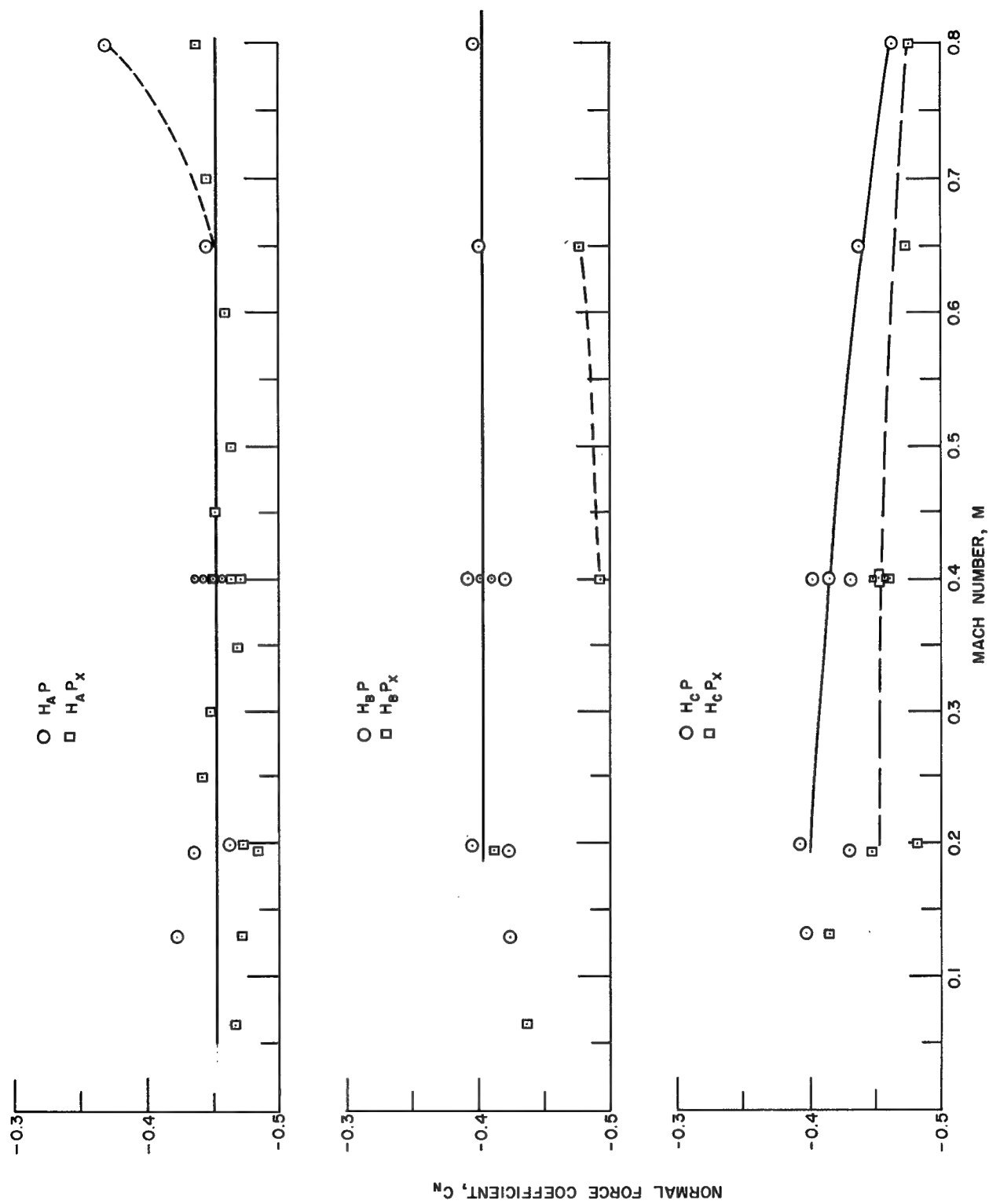


Fig. 24 -- Normal force coefficient on back face at zero yaw versus Mach number for all models (mixed Reynolds numbers)

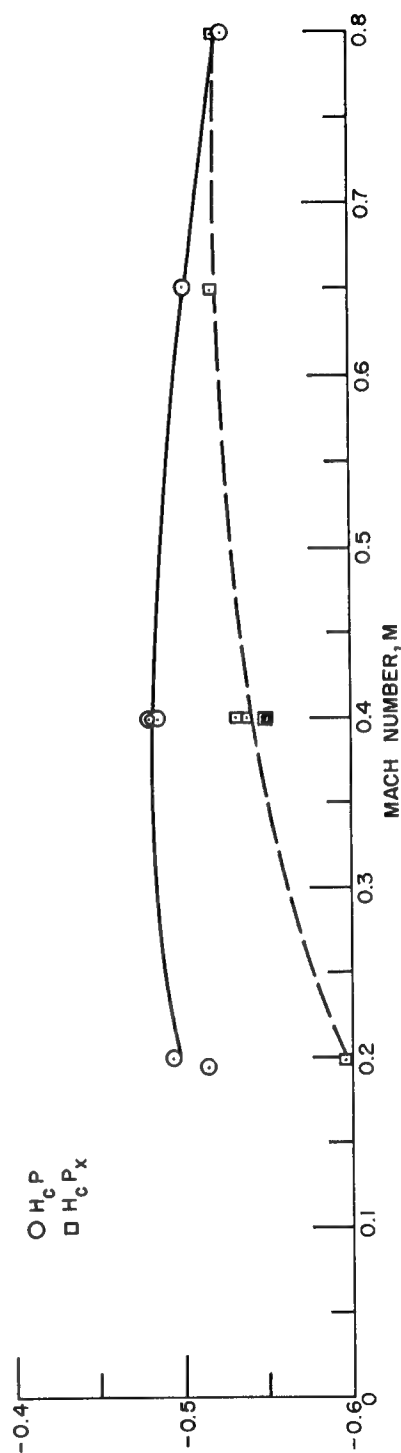
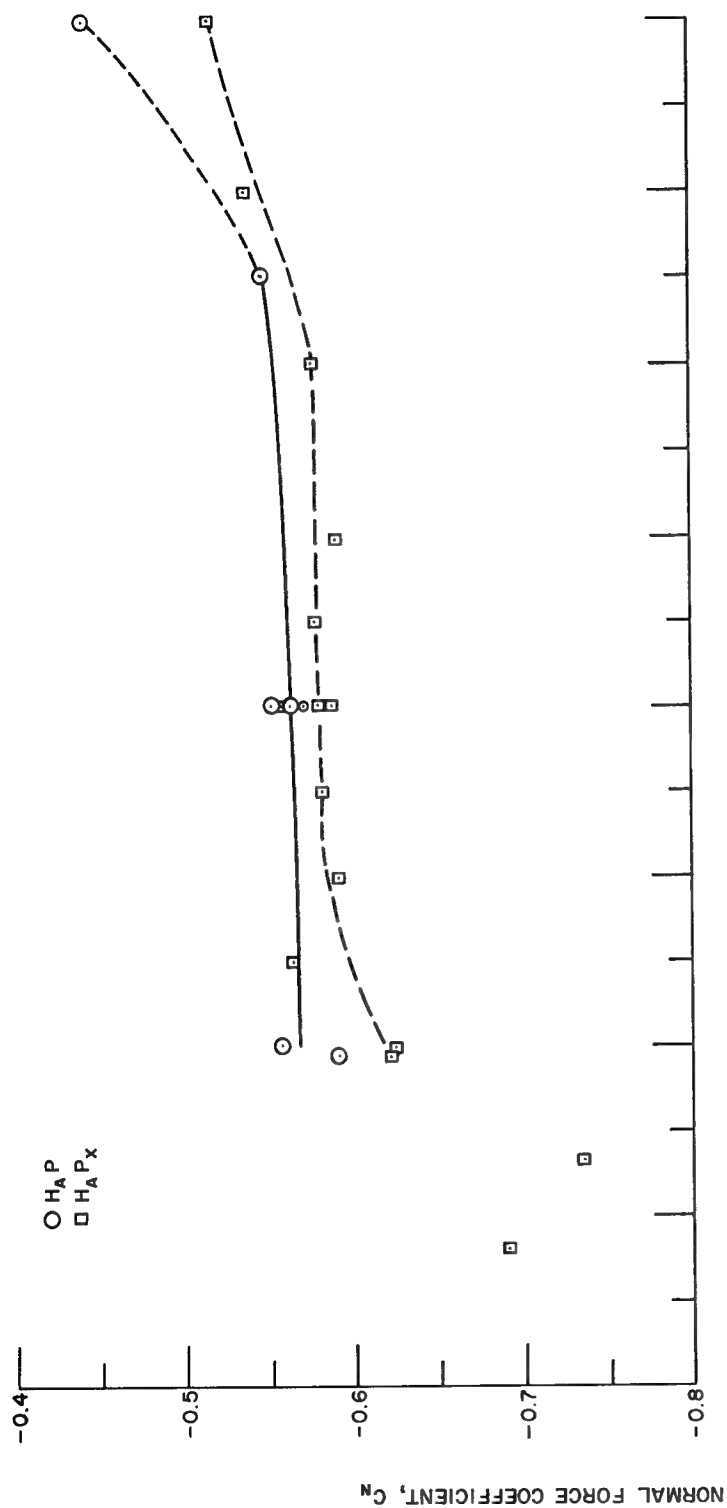


Fig. 25 -- Normal force coefficient averaged for left and right ends at zero yaw versus Mach number for  $H_A$  and  $H_C$  (mixed Reynolds numbers)

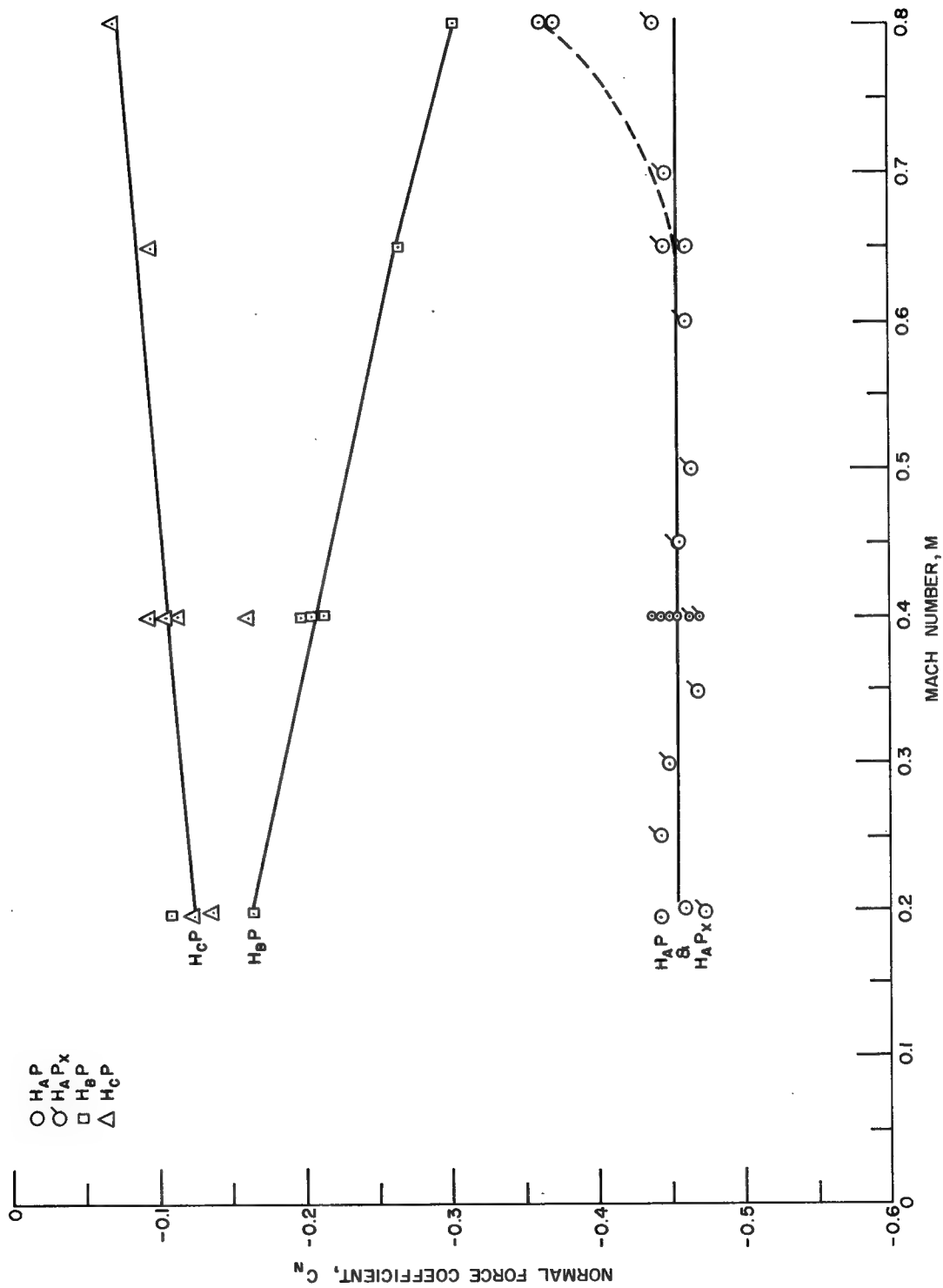


Fig. 26 -- Normal force coefficient on square face in leeward position,  $\psi = 90^\circ$

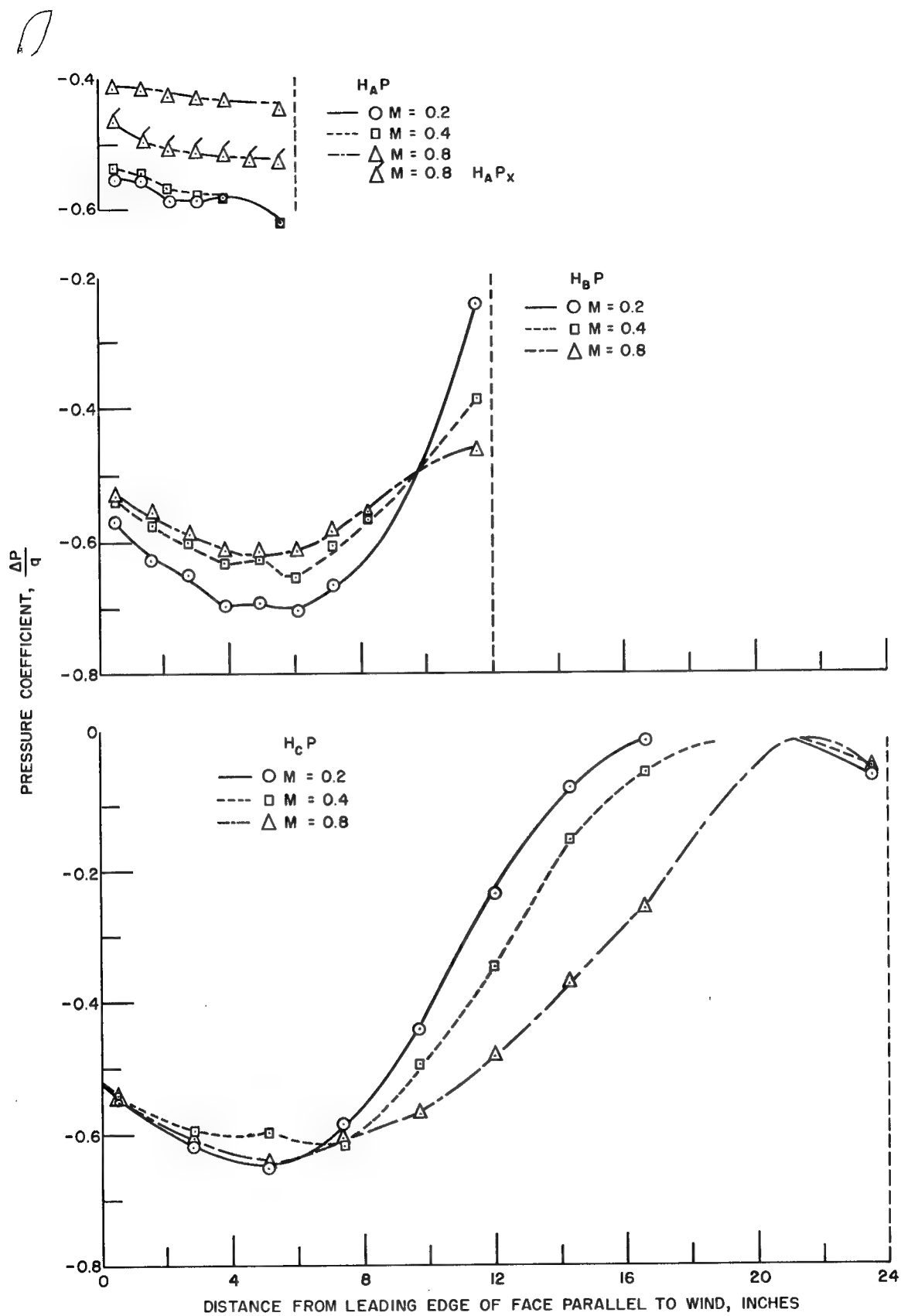


Fig. 27 -- Horizontal centerline pressure distribution on face parallel to wind, for each model at  $\psi = 90^\circ$ , Mach number as parameter

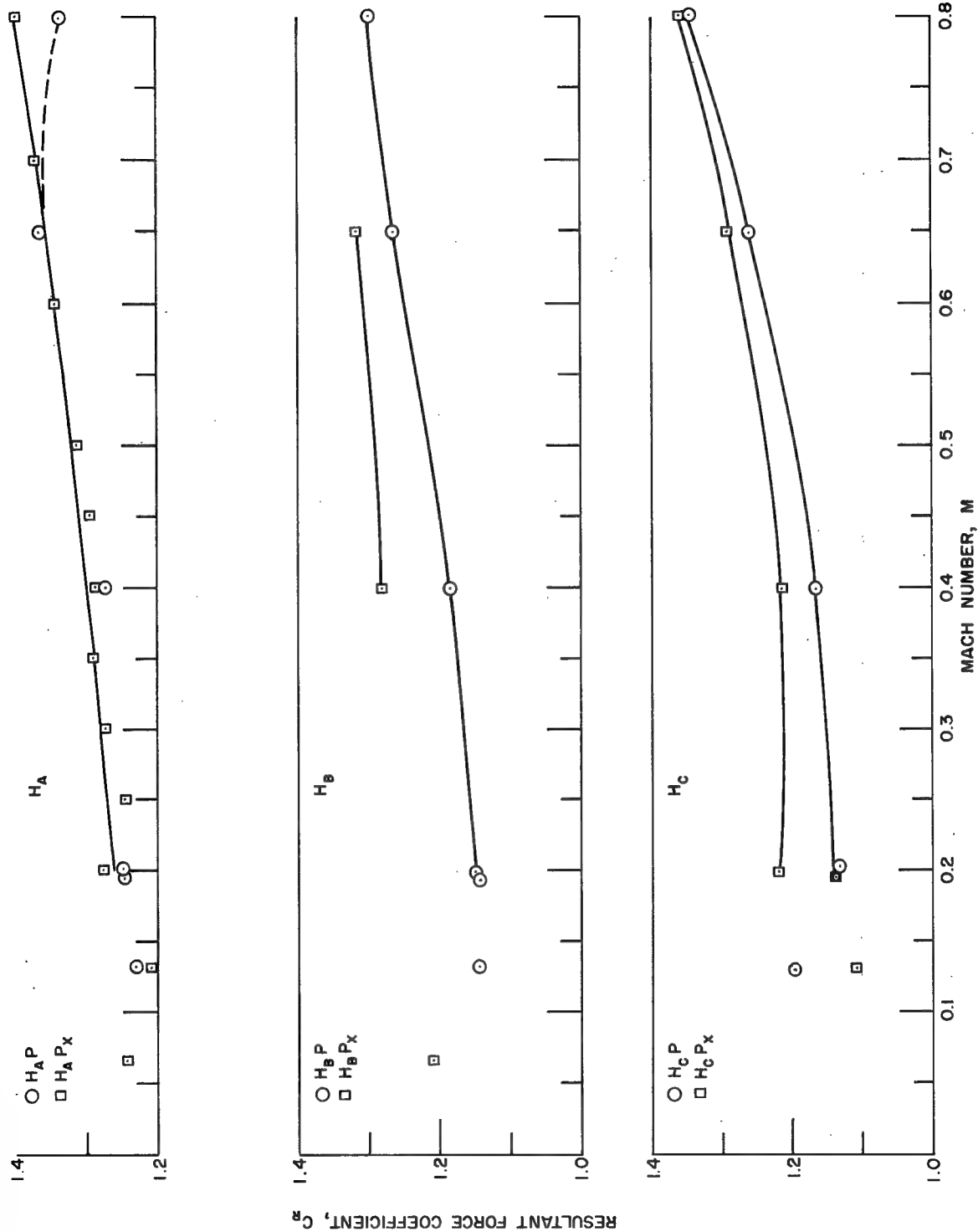


Fig. 28 -- Resultant force coefficient versus Mach number at zero yaw, block form and mounting as parameters



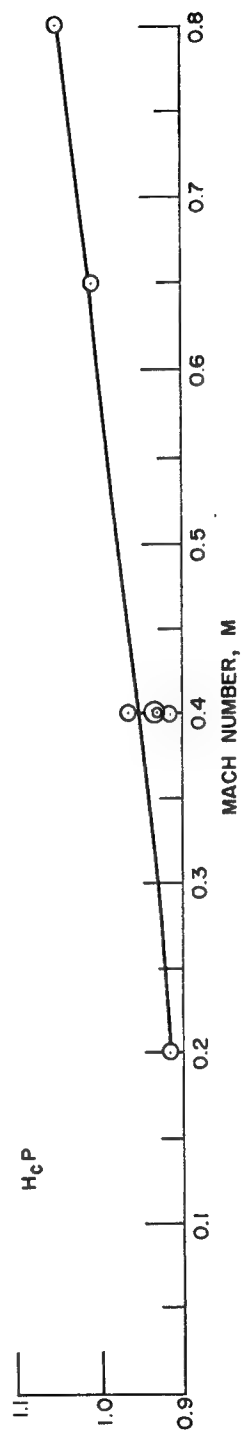
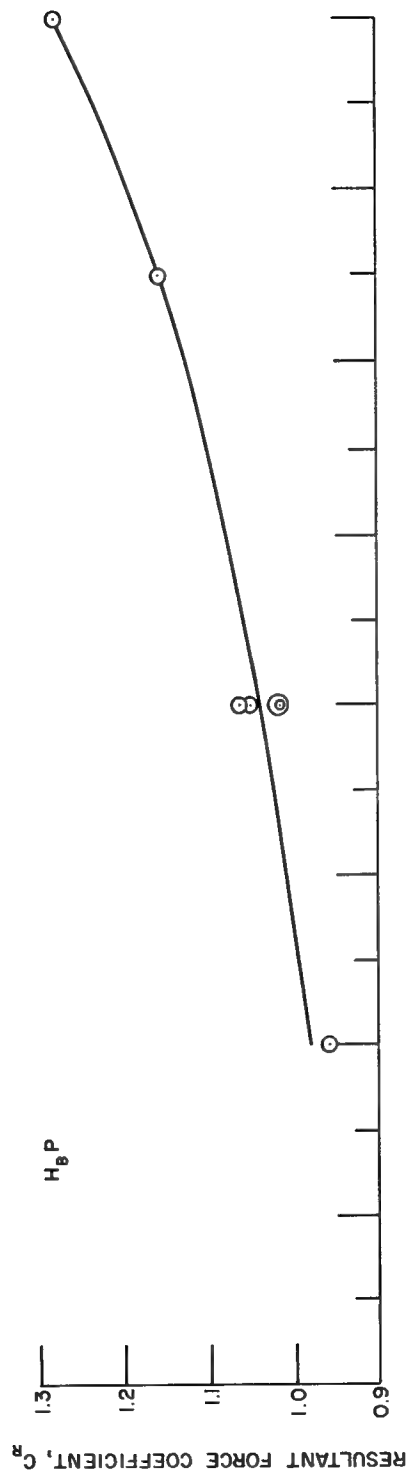
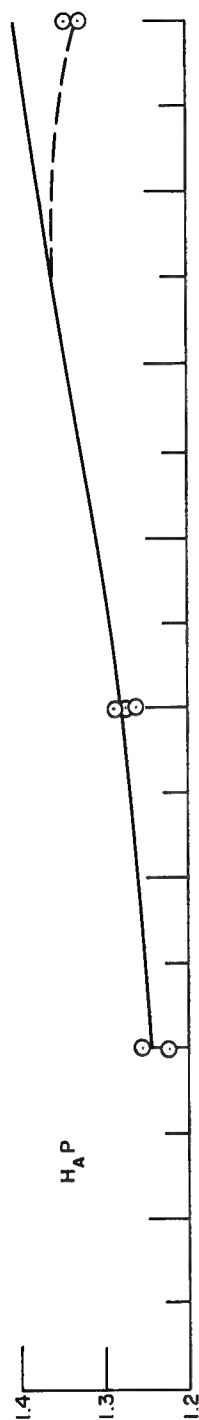


Fig. 29 -- Resultant force coefficient versus Mach number,  $\psi = 90^\circ$ , block form as parameter

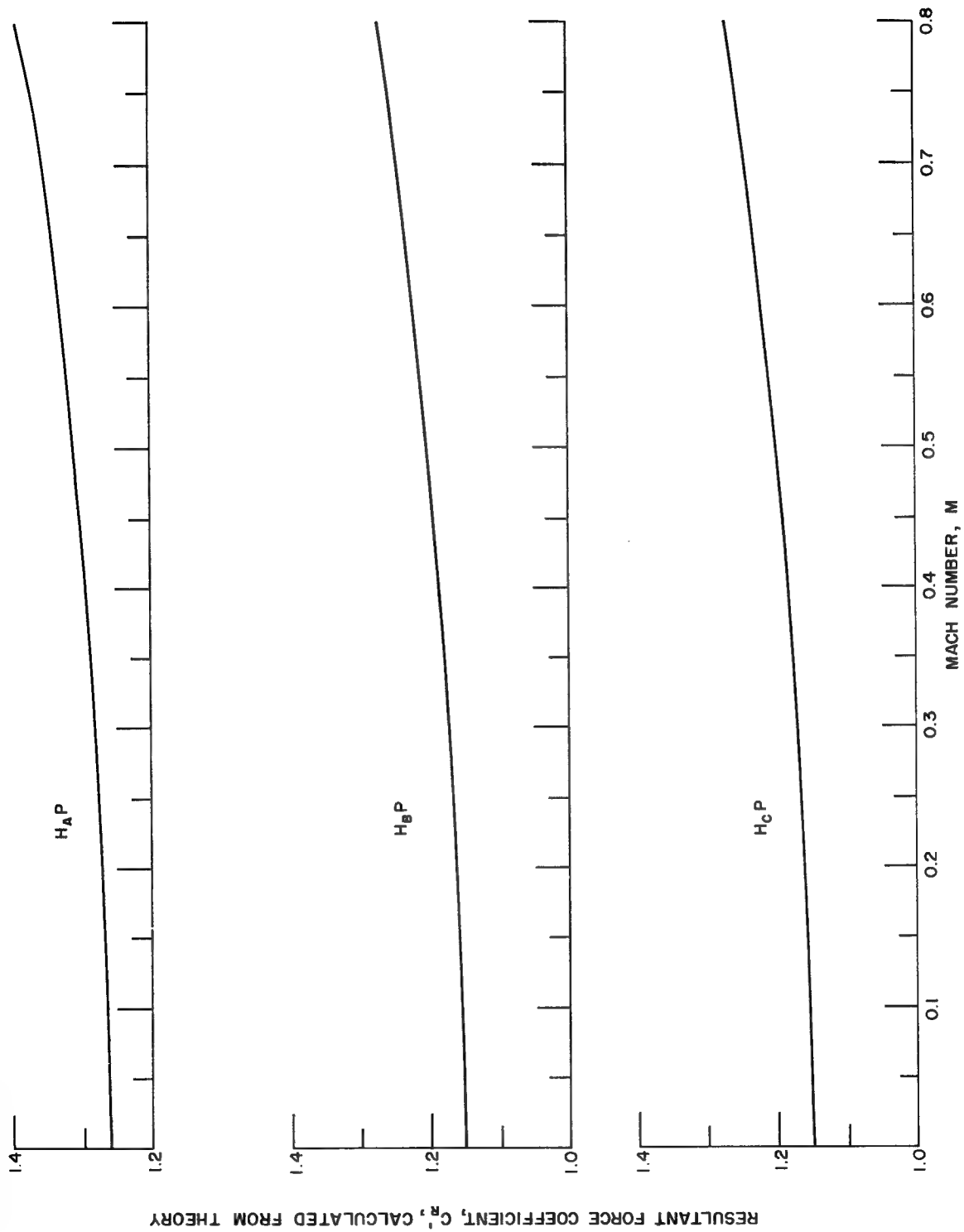


Fig. 30 -- Resultant force coefficient versus Mach number calculated from theoretical impact pressures (based on  $M = 0.4$  experimental values), block form as a parameter,  $\psi = 0^\circ$

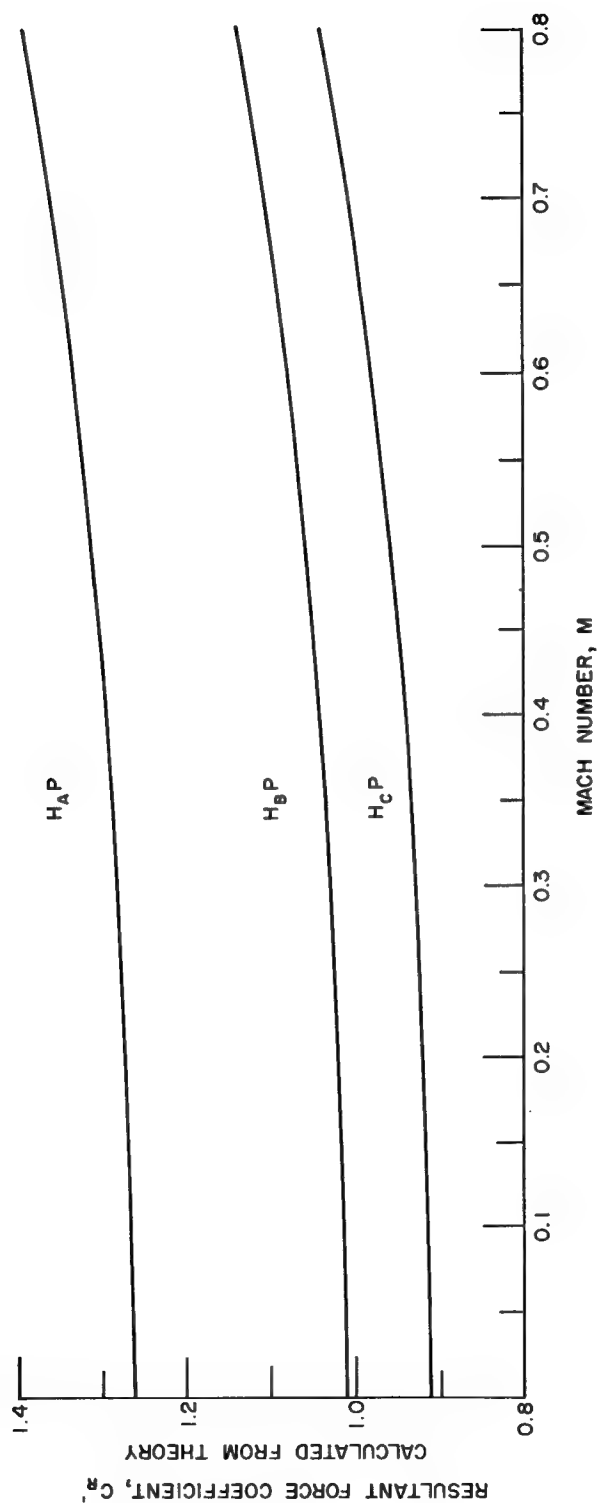


Fig. 31 -- Resultant force coefficient versus Mach number calculated from theoretical impact pressures (based on  $M = 0.4$  experimental values), block form as a parameter,  $\psi = 90^\circ$

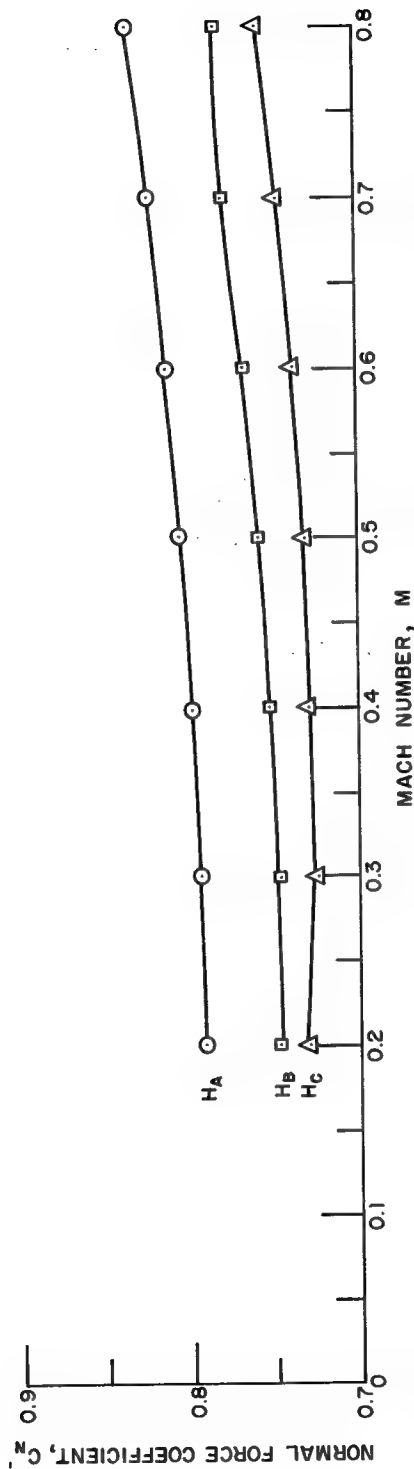


Fig. 32 -- Normal force coefficient on the front face based on impact pressure,  $\frac{C_N(M)}{1 + \frac{M^2}{4}}$ , versus Mach number, block form with plate mounting as a parameter,  $\psi = 0^\circ$

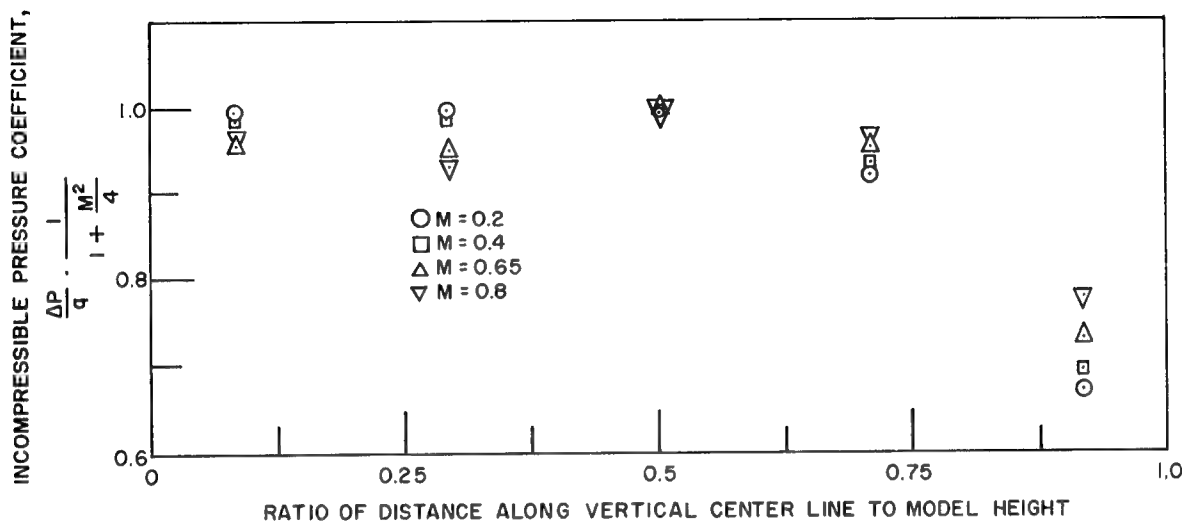


Fig. 33a -- Vertical centerline pressure distribution corrected for compressibility effects on  $H_A$  block, Mach number as a parameter

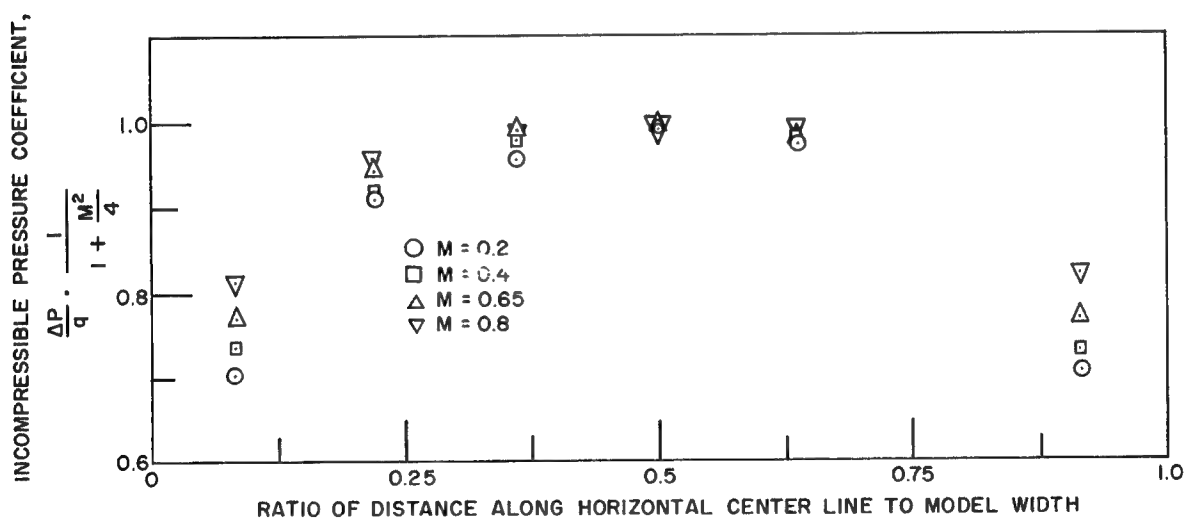


Fig. 33b -- Horizontal centerline pressure distribution corrected for compressibility effects on  $H_A$  block, Mach number as a parameter

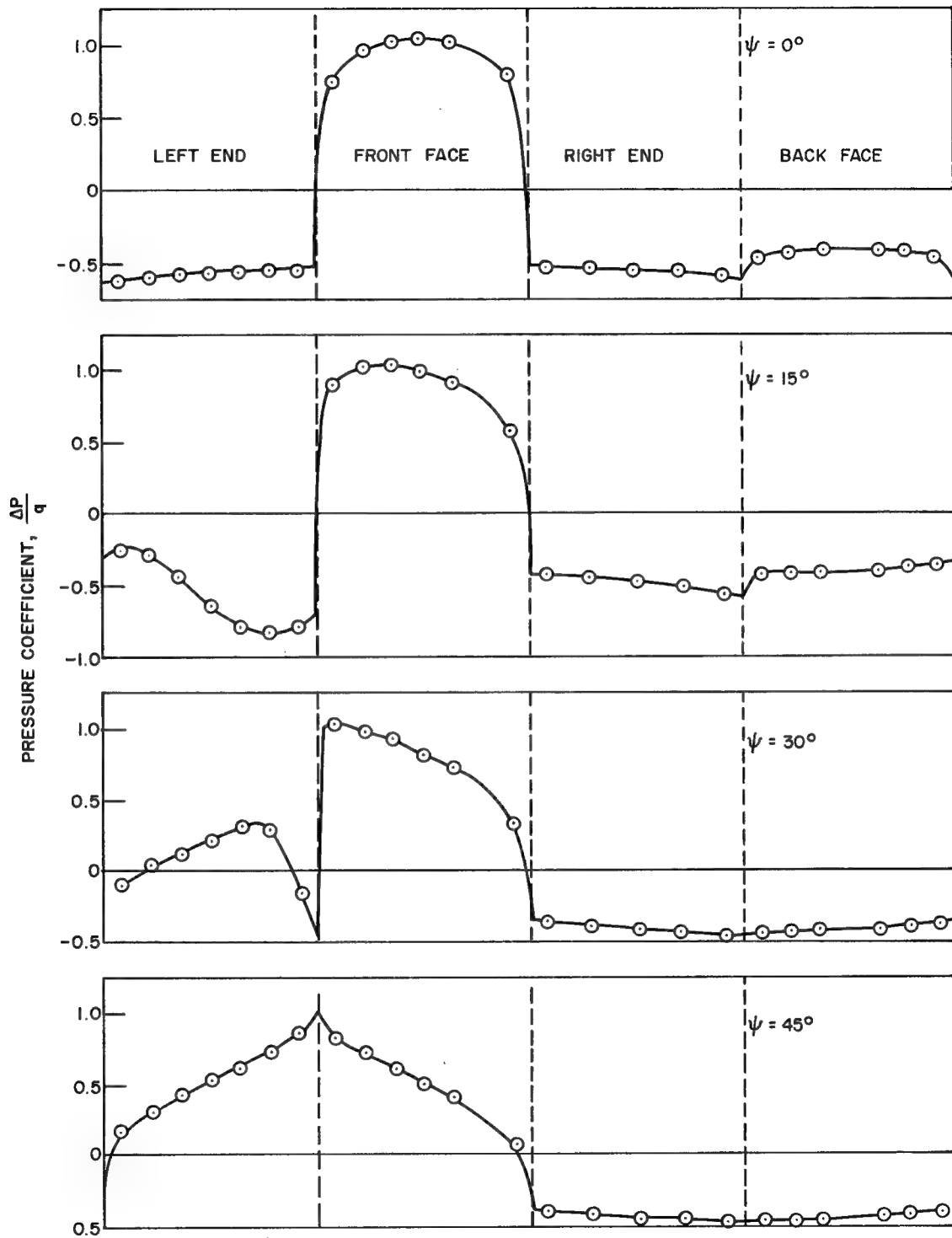


Fig. 34 -- Horizontal centerline pressure distribution on  $H_A$  block at  $M = 0.4$ , yaw angle as a parameter

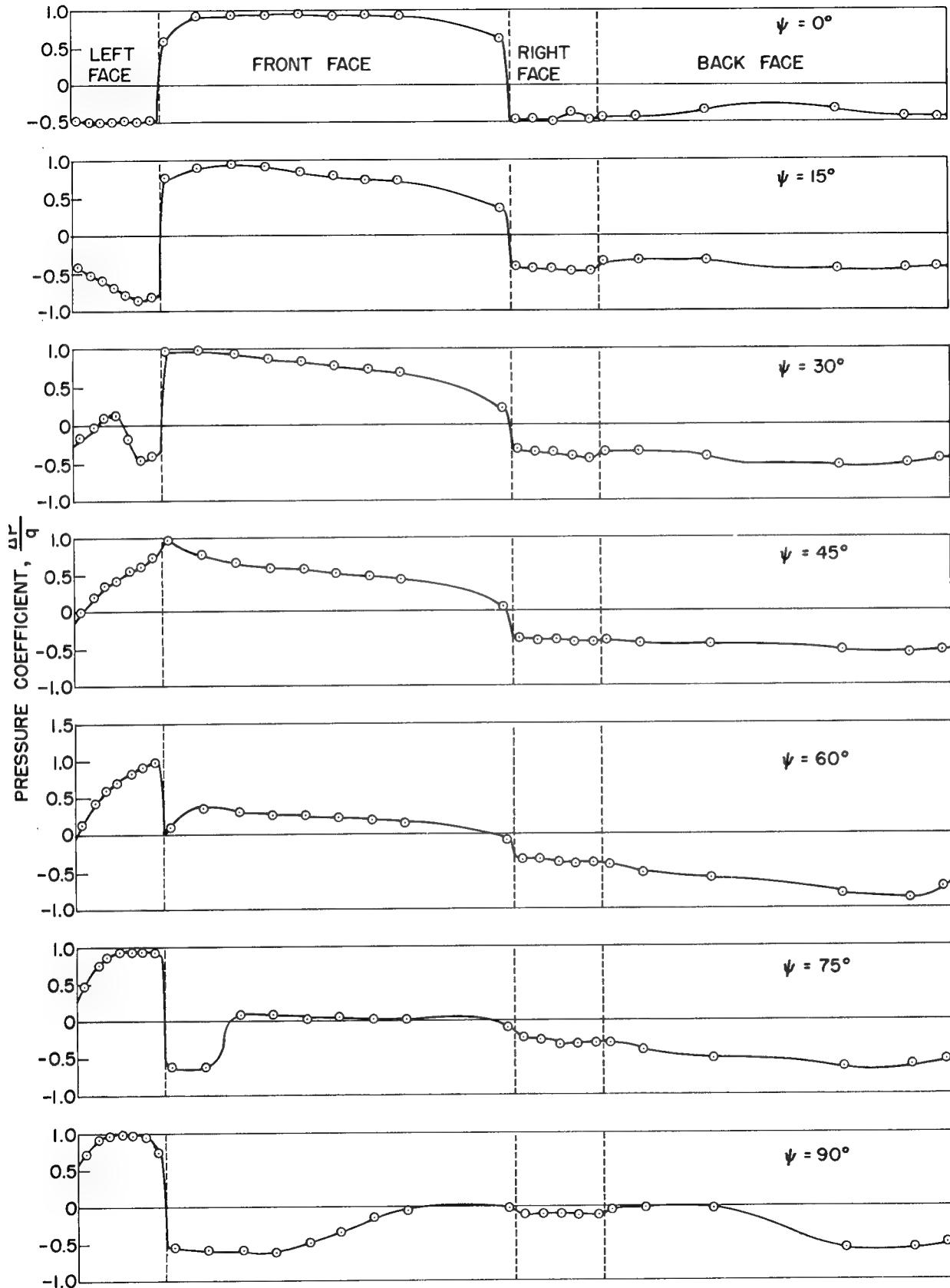


Fig. 35 -- Horizontal centerline pressure distribution on HC block at  $M = 0.4$ , yaw angle as a parameter

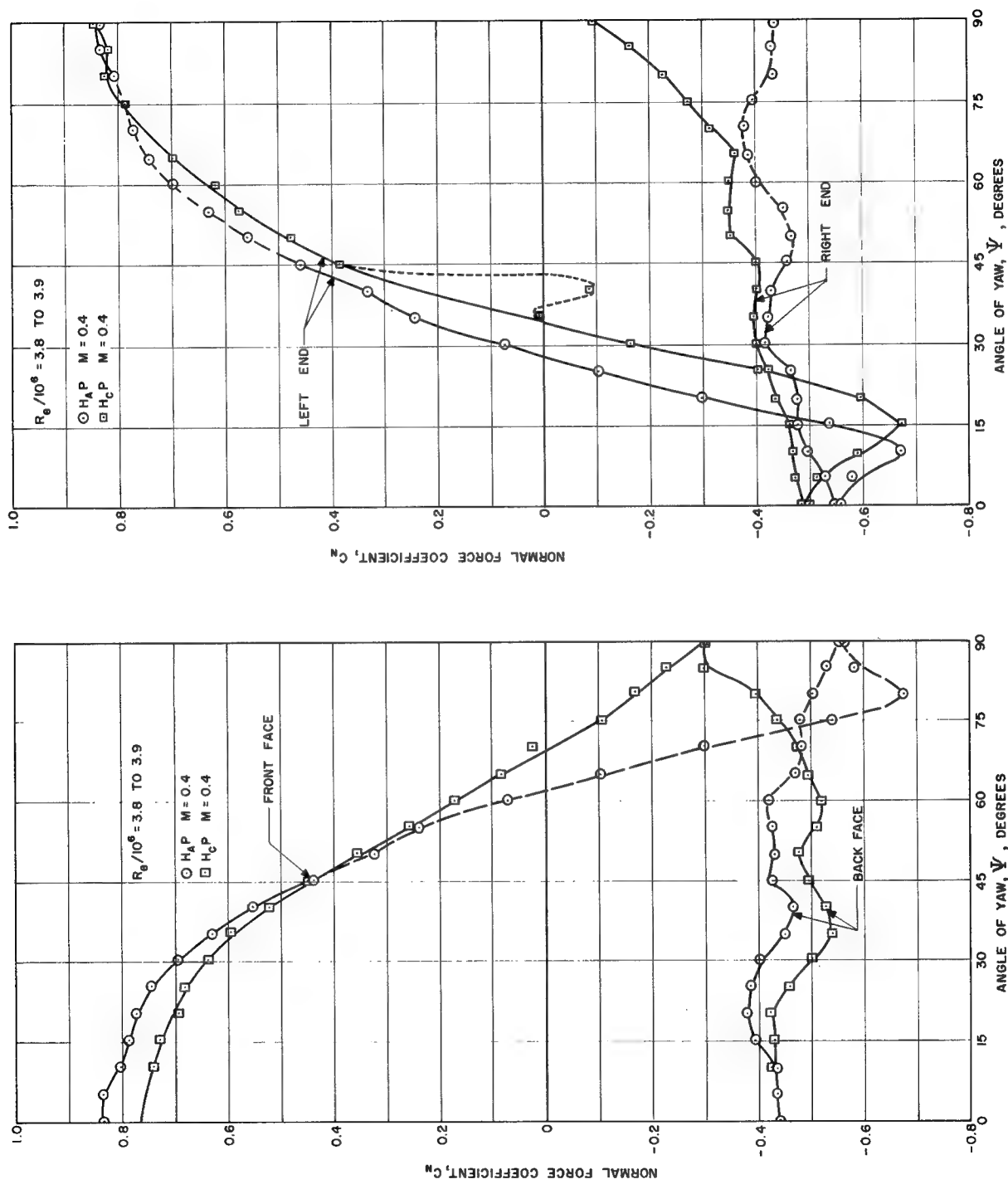


Fig. 36 -- Variation of panel normal force coefficients with yaw angle for HA P and HC P models at  $M = 0.4$



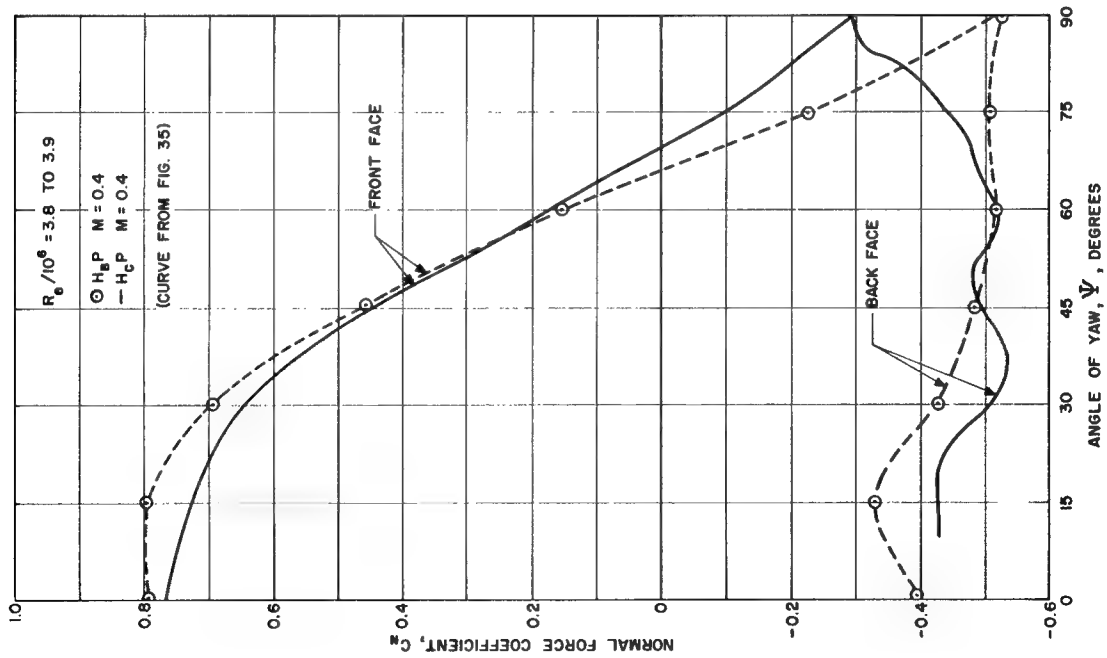
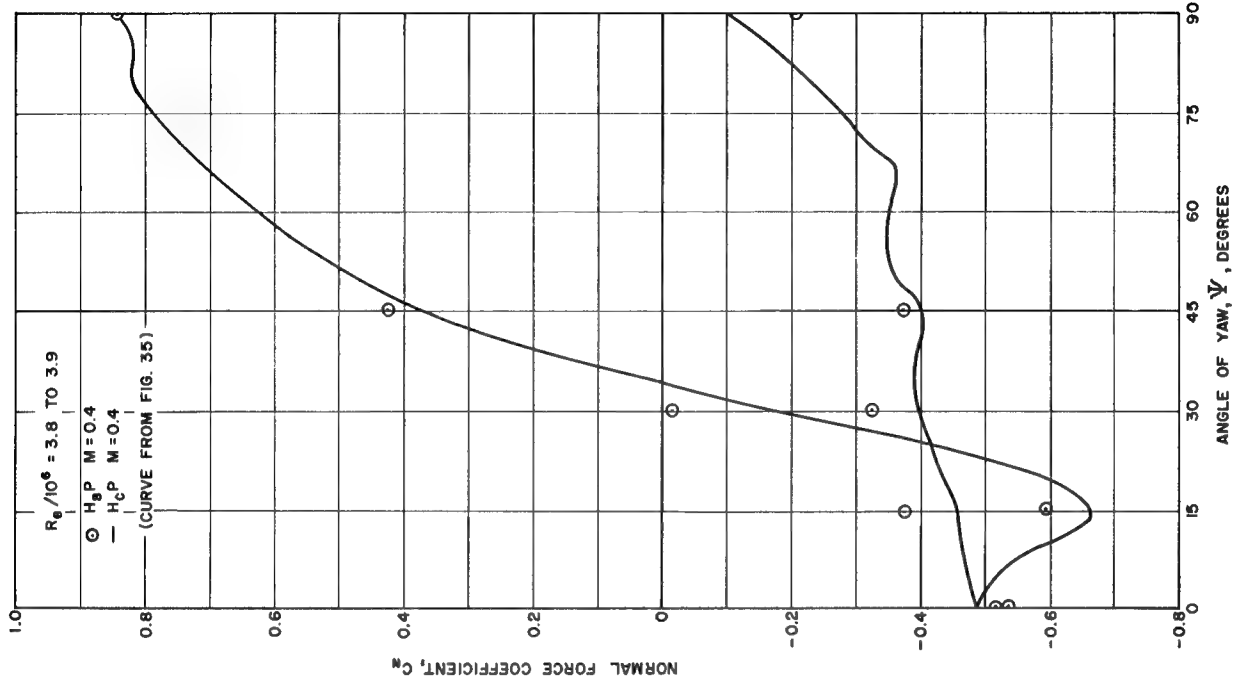


Fig. 37 -- Variation of panel normal force coefficients with yaw angle for  $H_{BP}$  and  $H_{CP}$  models at  $M = 0.4$

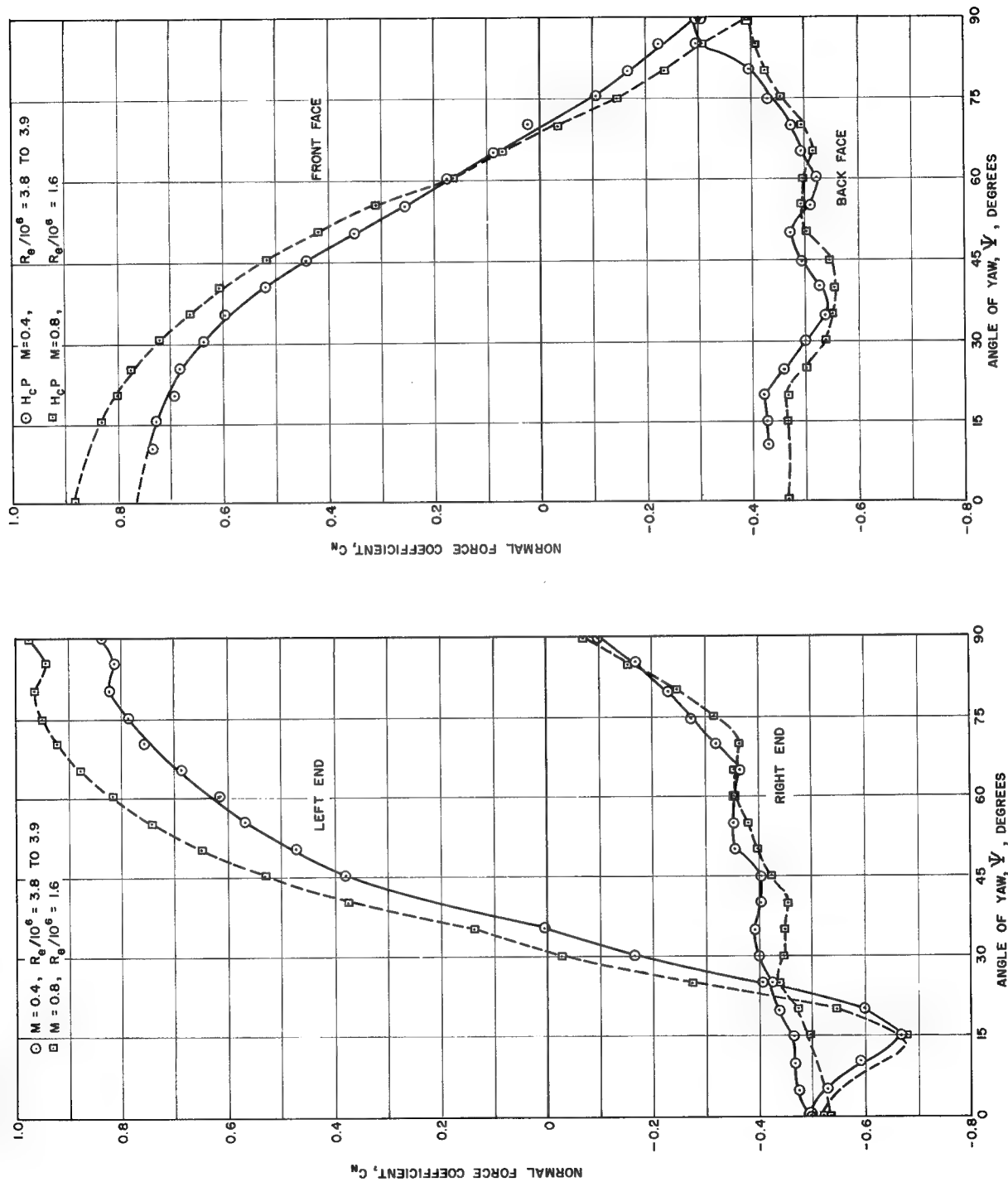


Fig. 38 -- Variation of panel normal force coefficients with yaw angle for  $H_C P$  model at  $M = 0.4$  and  $M = 0.8$

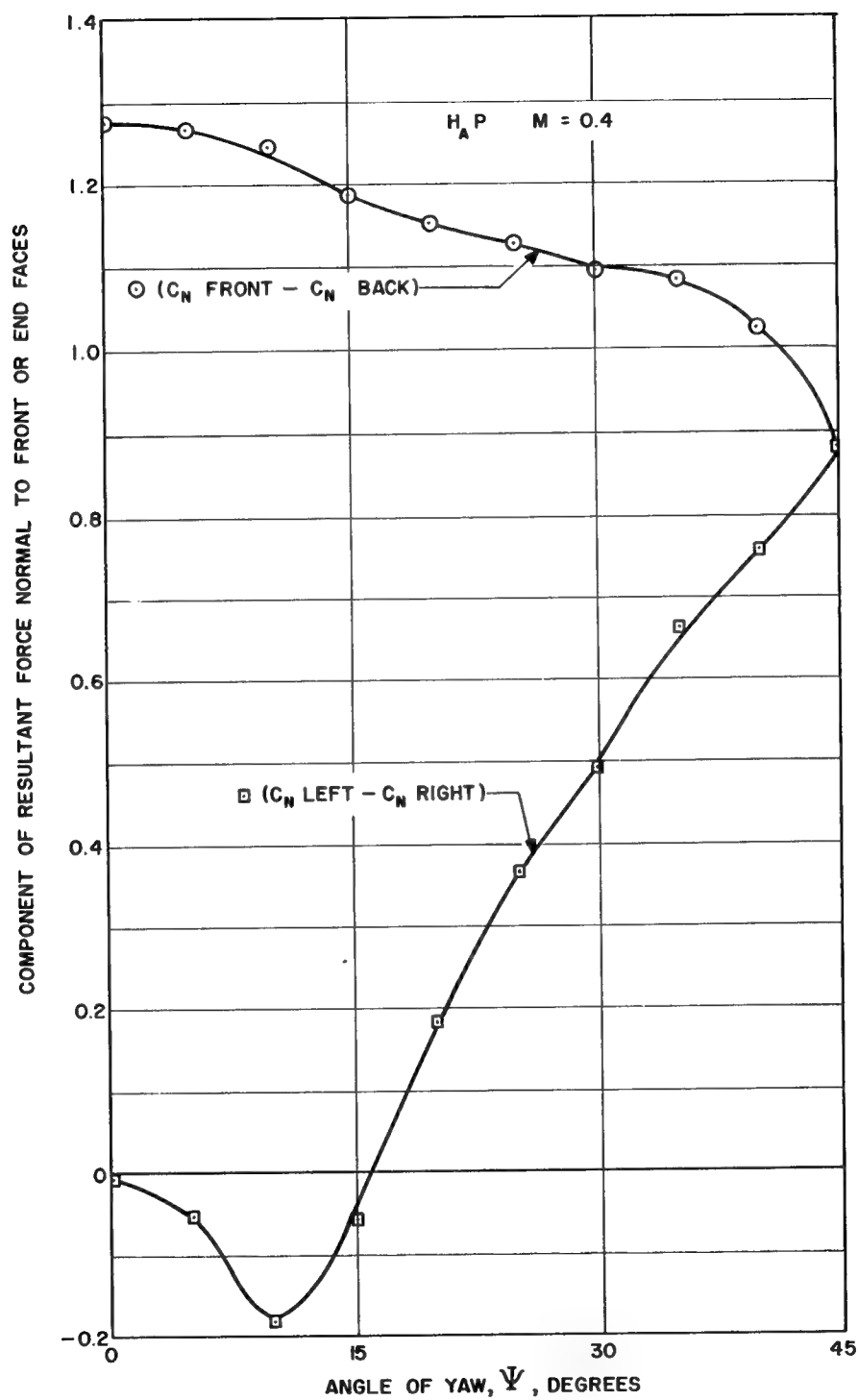


Fig. 39 -- Right angle components of resultant force on  $H_A P$  model versus yaw angle for  $M = 0.4$

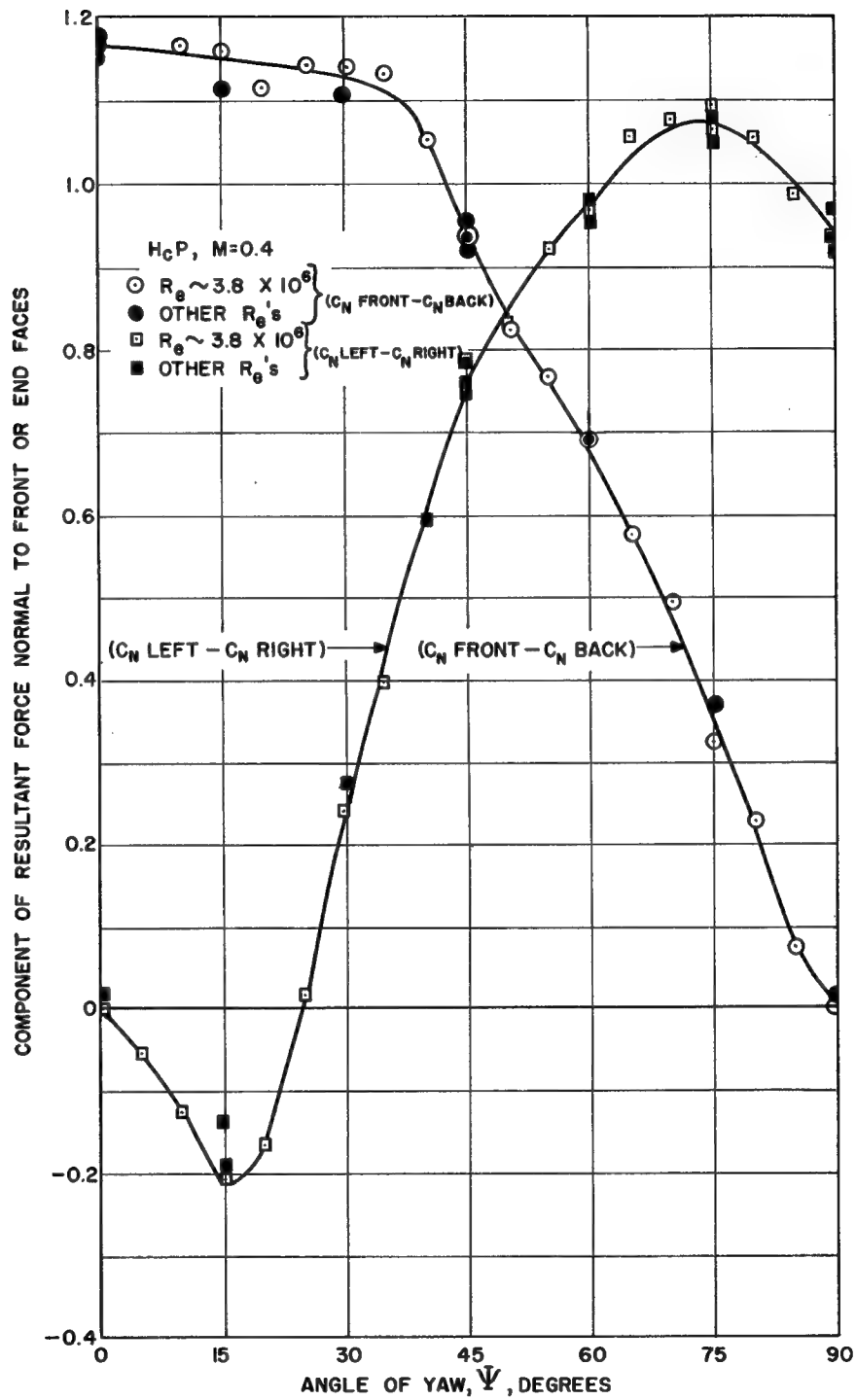


Fig. 40 -- Right angle components of resultant force on  $H_{CP}$  model versus yaw angle for  $M = 0.4$

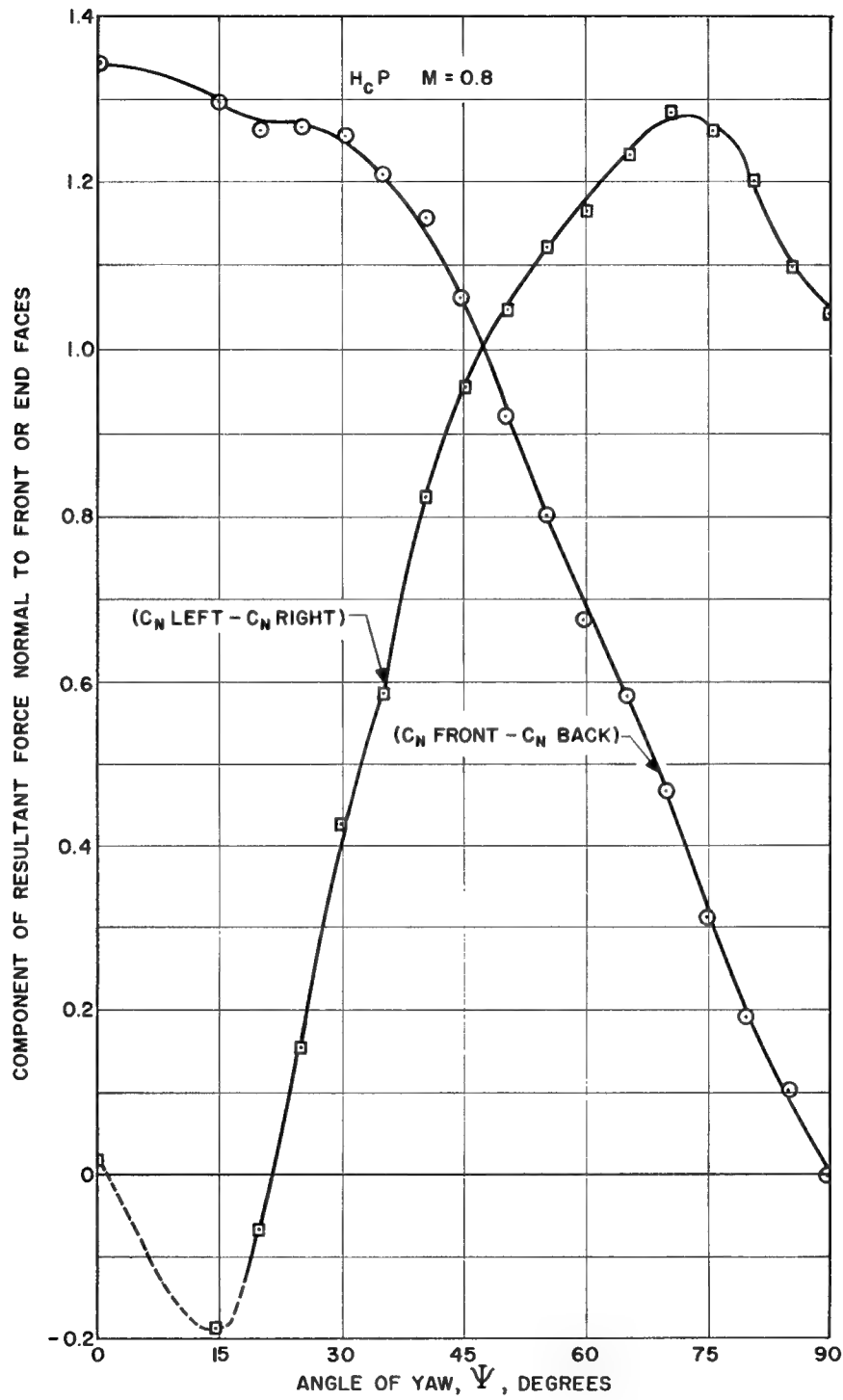


Fig. 41 -- Right angle components of resultant force on  $H_C P$  model versus yaw angle for  $M = 0.8$

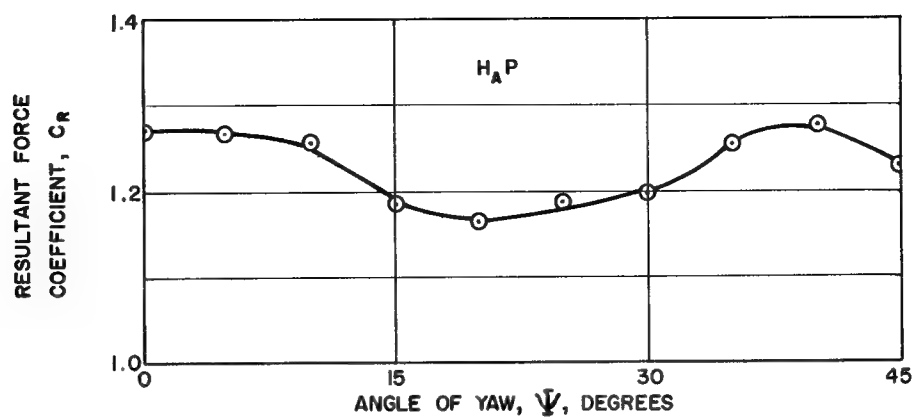


Fig. 42 -- Resultant force coefficient versus yaw angle for  $H_A P$  model at  $M = 0.4$

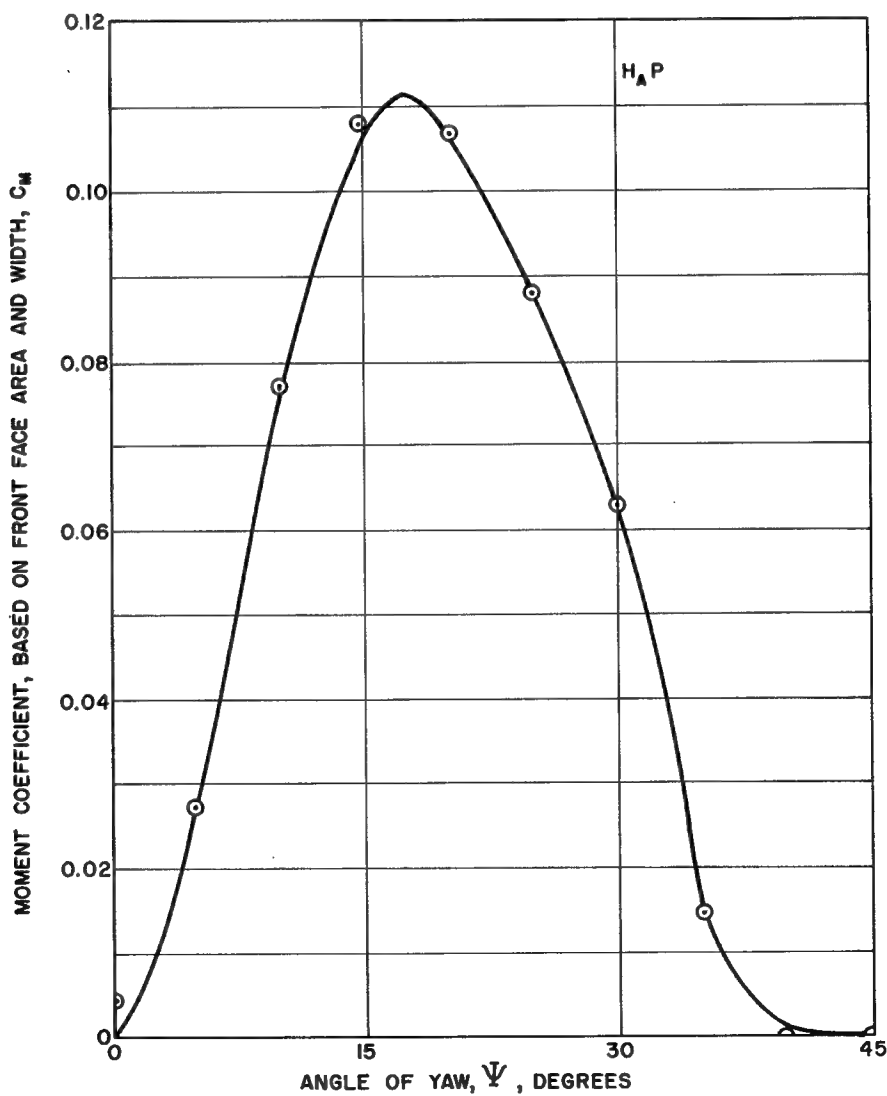


Fig. 43 -- Moment coefficient versus yaw angle for  $H_A P$  model at  $M = 0.4$

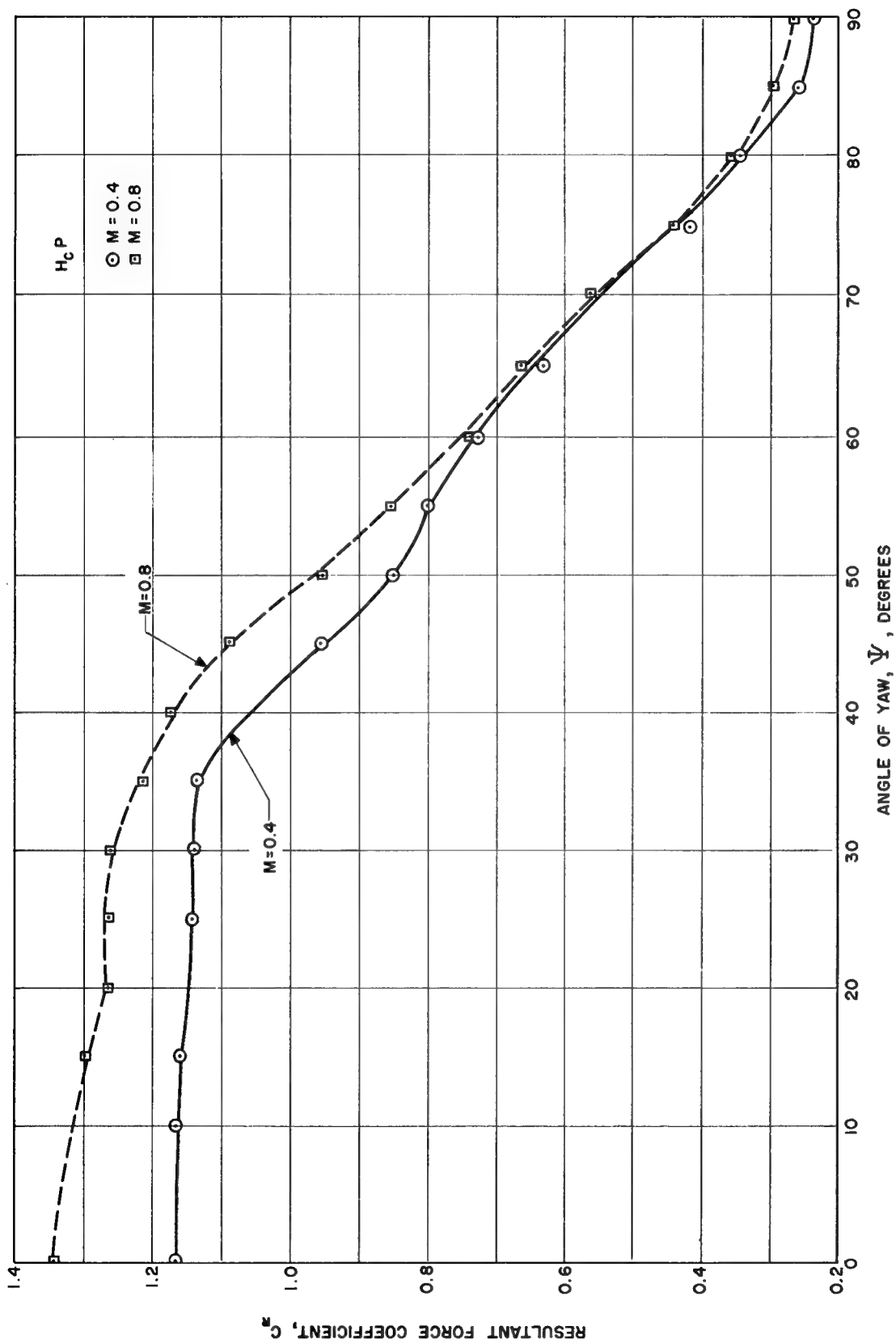


Fig. 44 -- Resultant force coefficient versus yaw angle for  $H_{cP}$   
model at  $M = 0.4$  and  $M = 0.8$

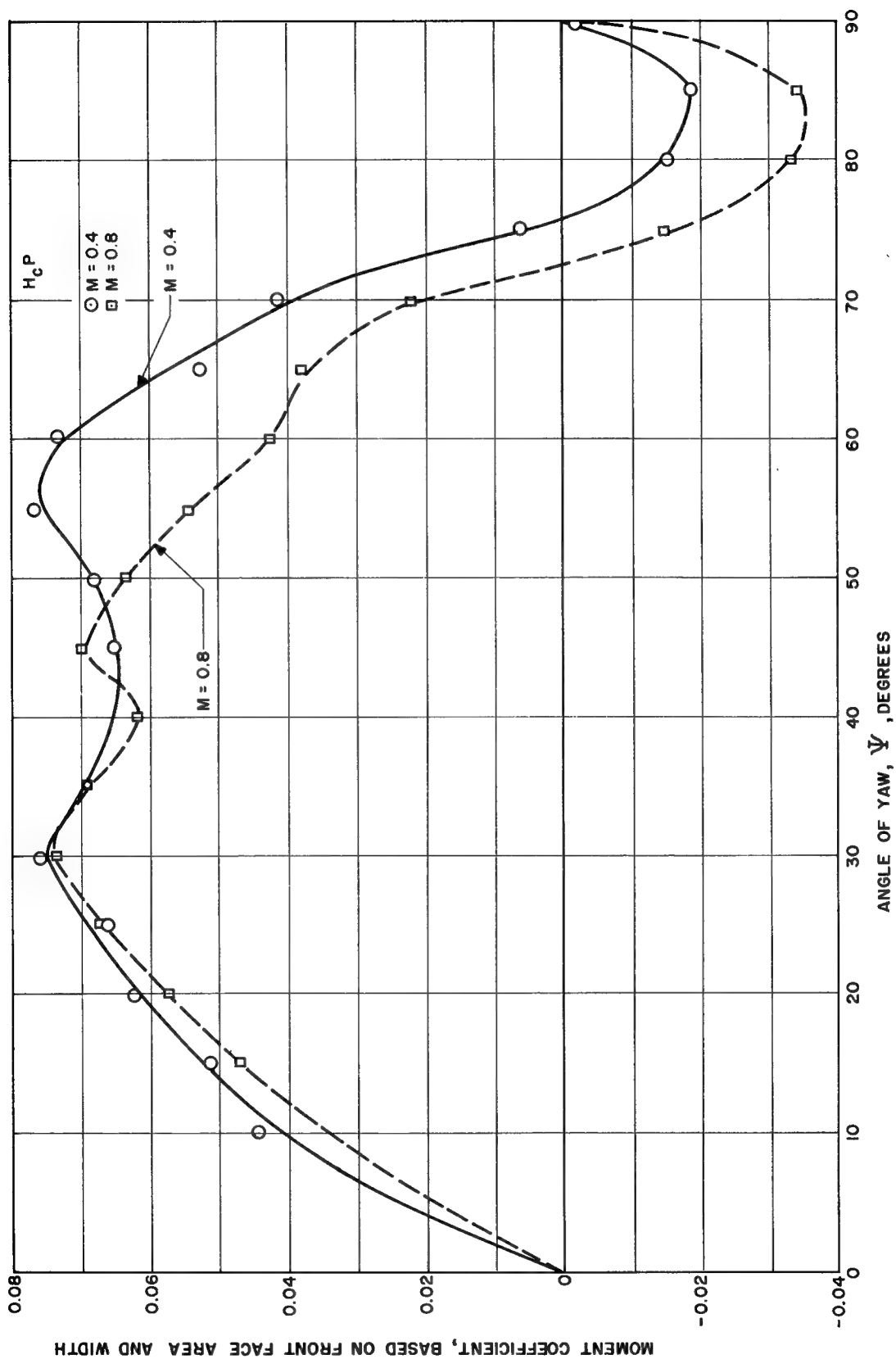


Fig. 45 -- Moment coefficient versus yaw angle for  $H_{cP}$  model at  $M = 0.4$  and  $M = 0.8$



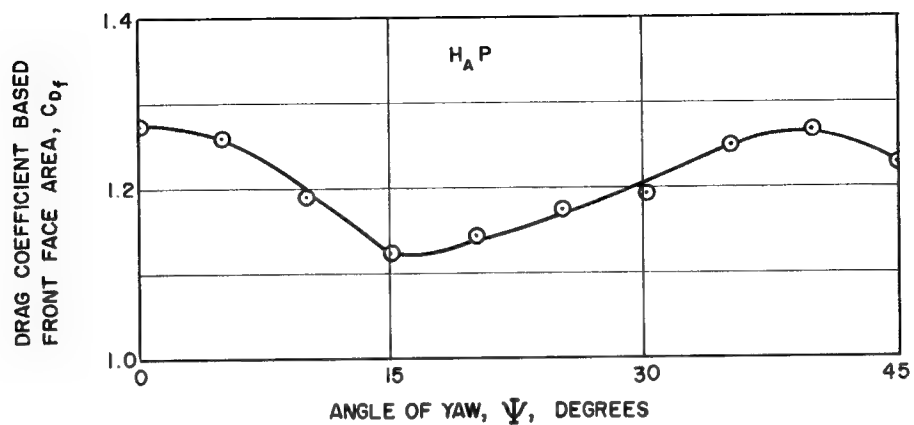


Fig. 46 -- Drag coefficient, based on front face area, versus yaw angle for  $H_A P$  model at  $M = 0.4$

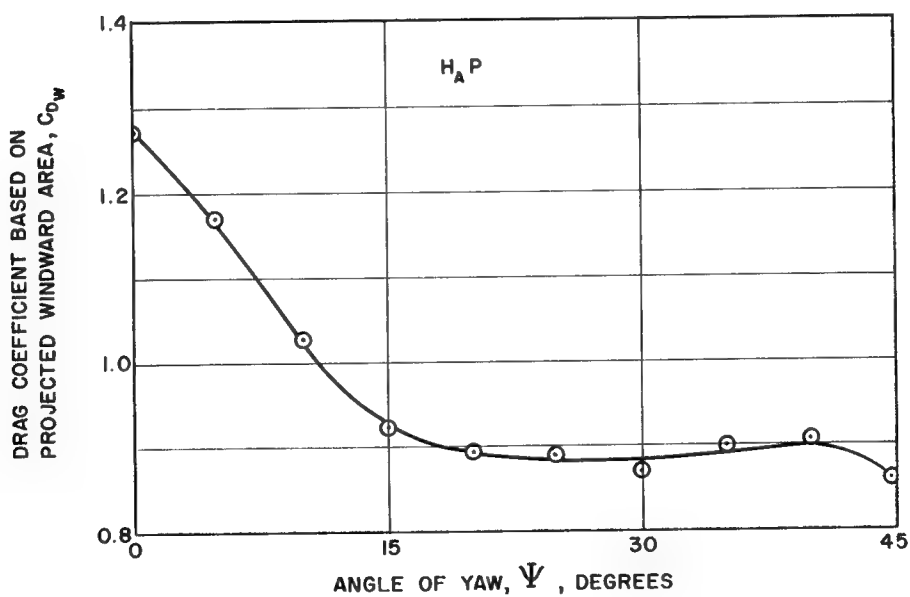


Fig. 47 -- Drag coefficient, based on projected windward area, versus yaw angle for  $H_A P$  model at  $M = 0.4$

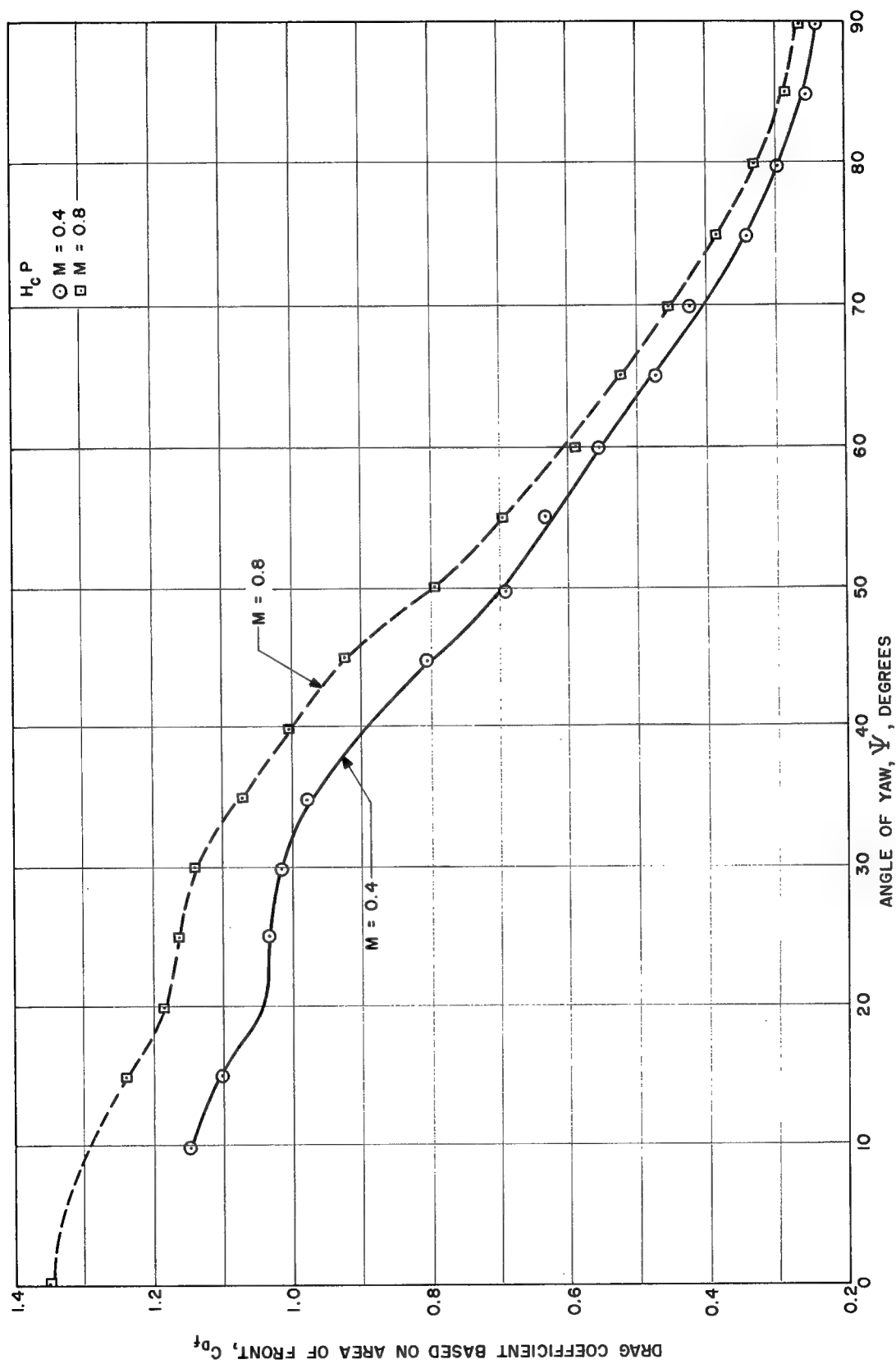


Fig. 48 -- Drag coefficient, based on front face area, versus yaw angle for  $H_{cP}$  model at  $M = 0.4$  and  $M = 0.8$

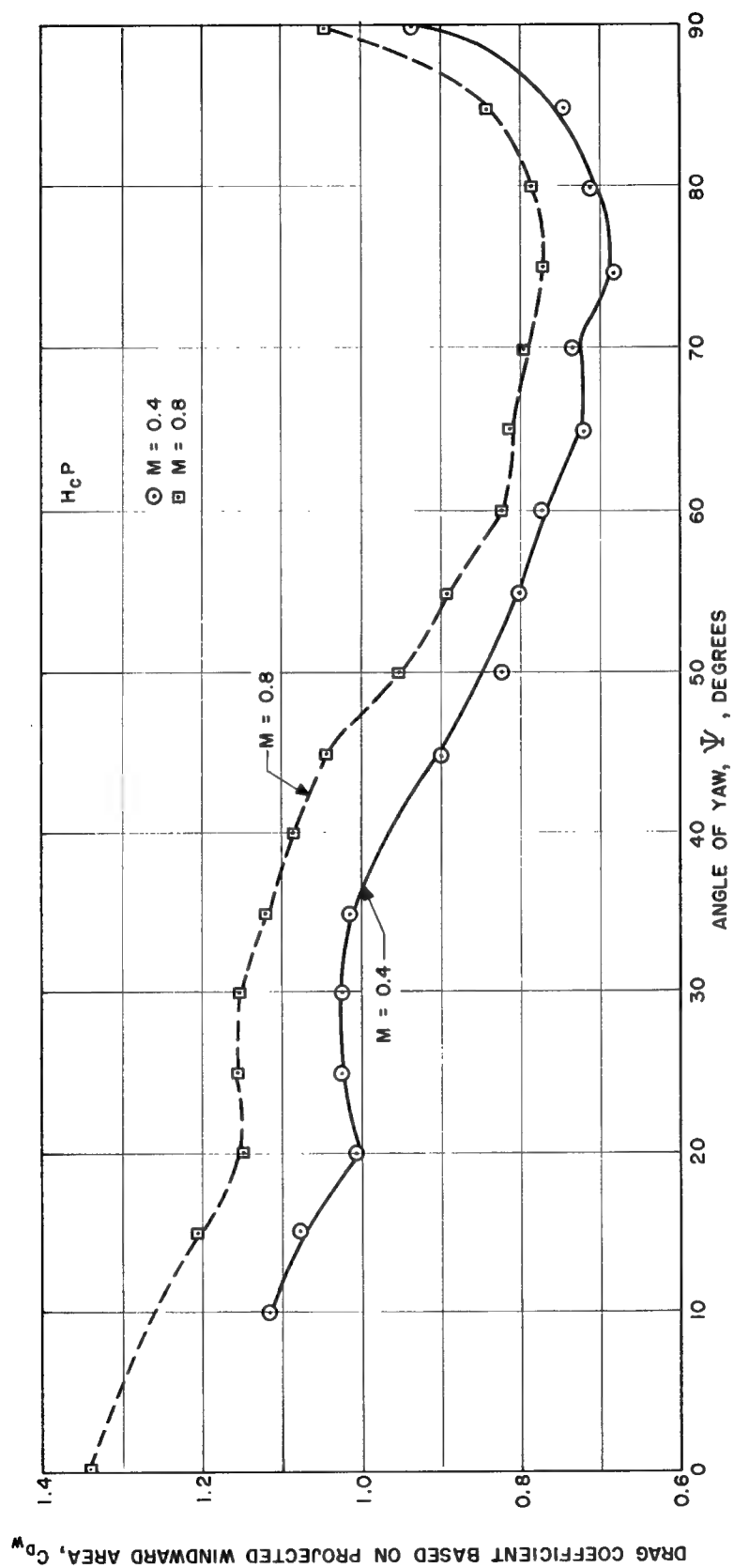


Fig. 49 -- Drag coefficient, based on projected windward area, versus yaw angle for  $H_C P$  model at  $M = 0.4$  and  $M = 0.8$

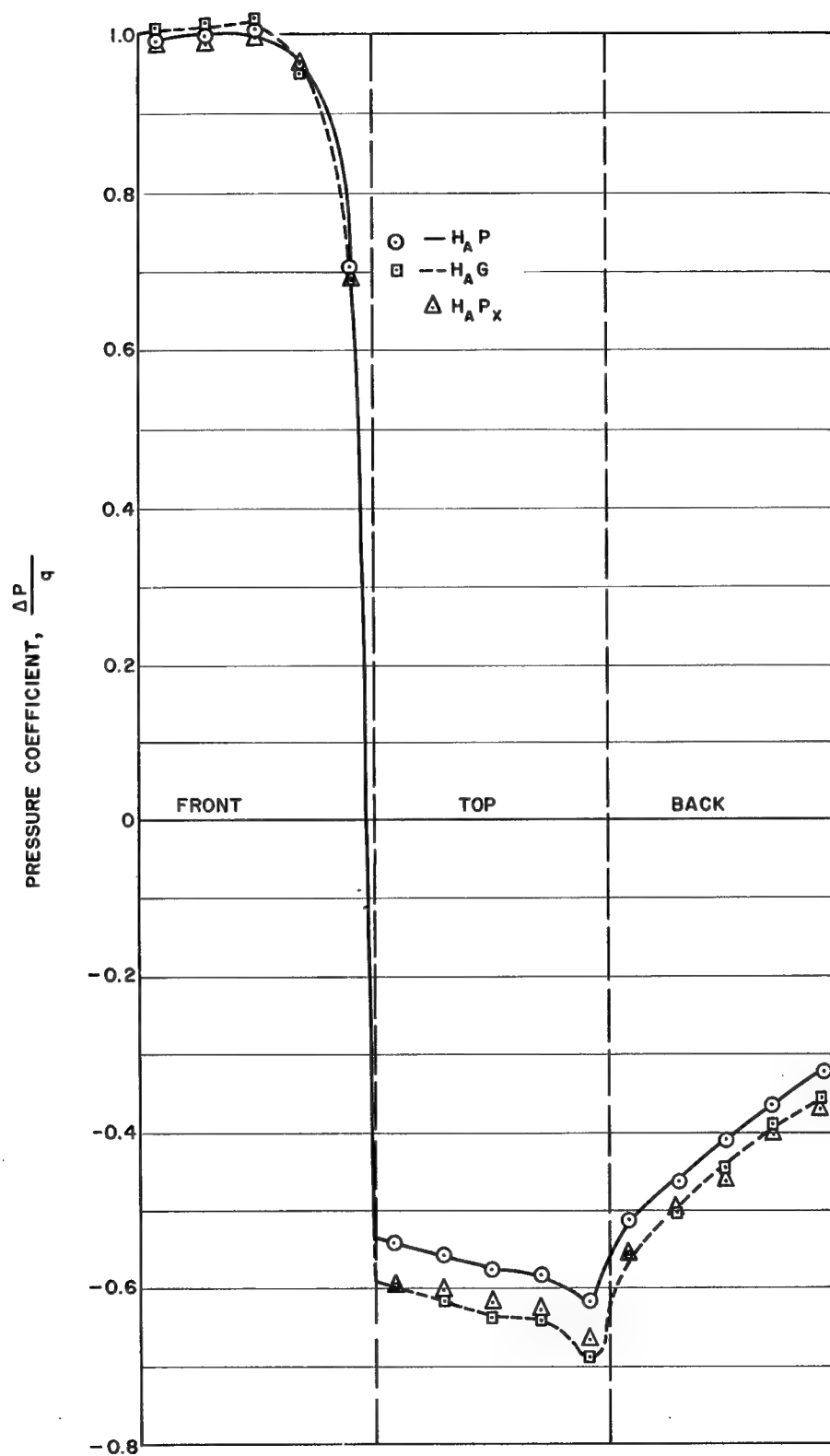


Fig. 50 -- Vertical centerline pressure distribution on  $H_A$  block in UW tunnel, at  $M \approx 0.2$ , mounting as parameter,  $\psi = 0^\circ$

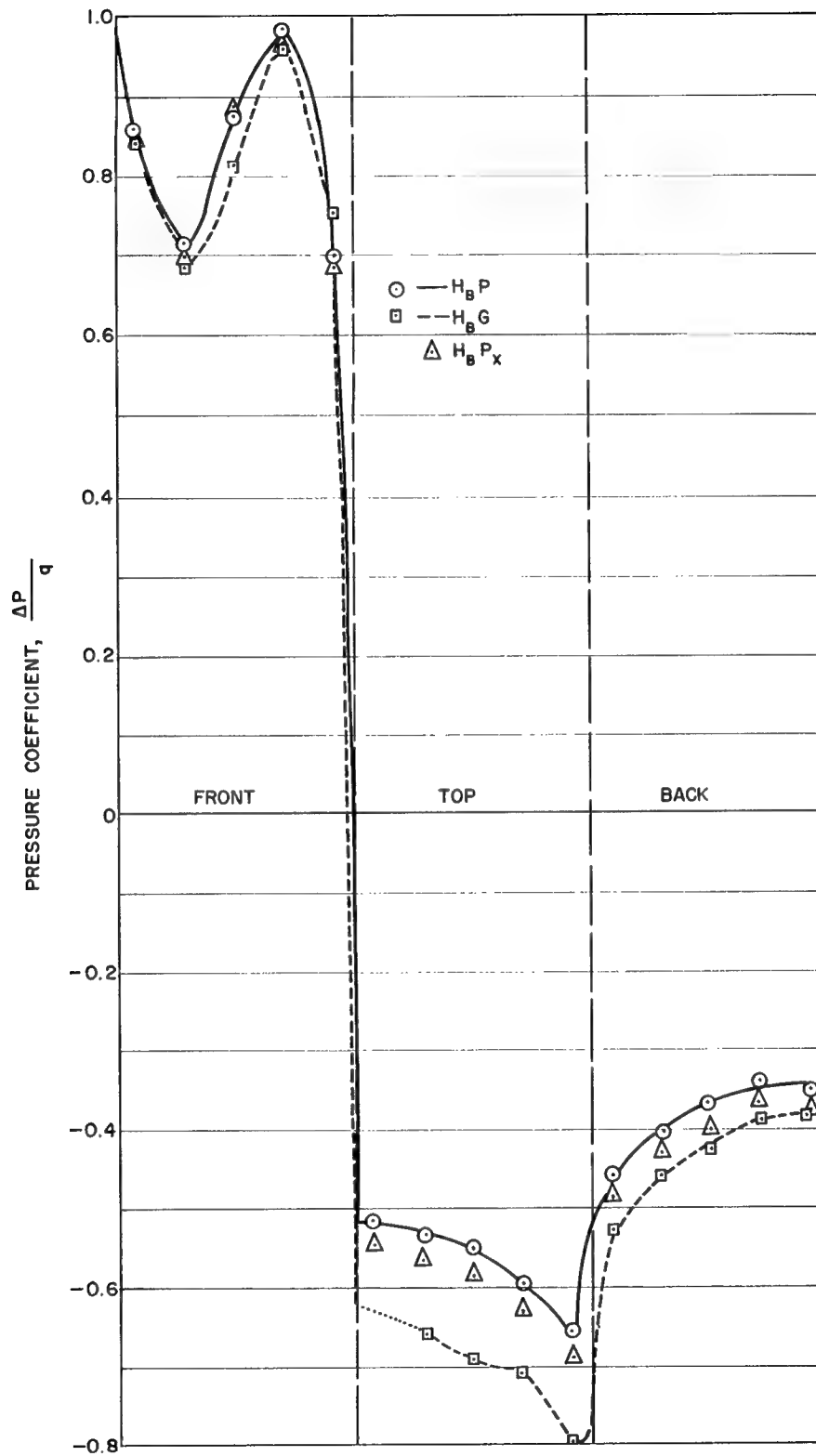


Fig. 51 -- Vertical centerline pressure distribution on  $H_B$  block in UW tunnel, at  $M \approx 0.2$ , mounting as parameter,  $\psi = 0^\circ$

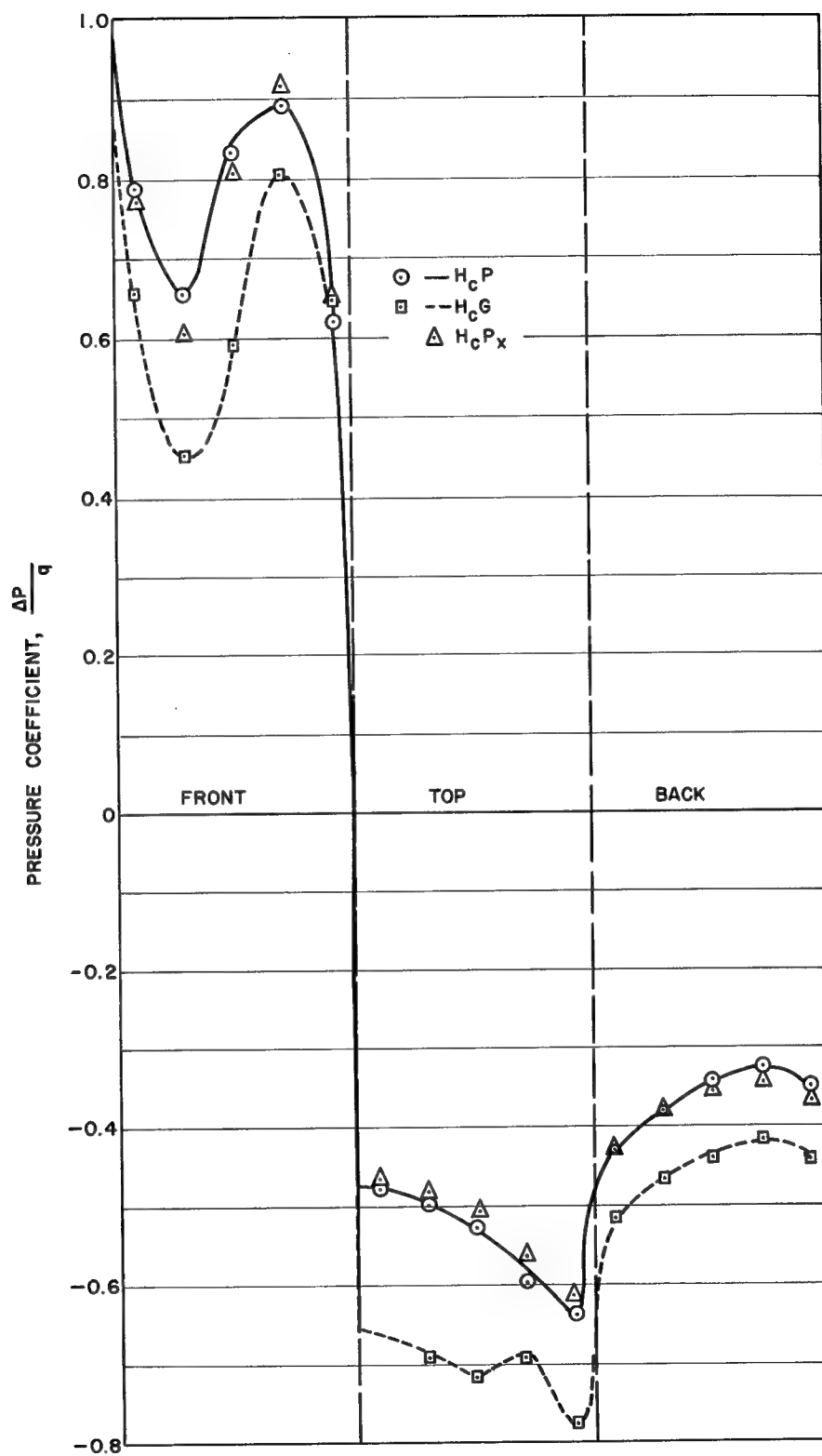


Fig. 52 -- Vertical centerline pressure distribution on  $H_C$  block in UW tunnel at  $M \approx 0.2$ , mounting as parameter,  $\psi = 0^\circ$

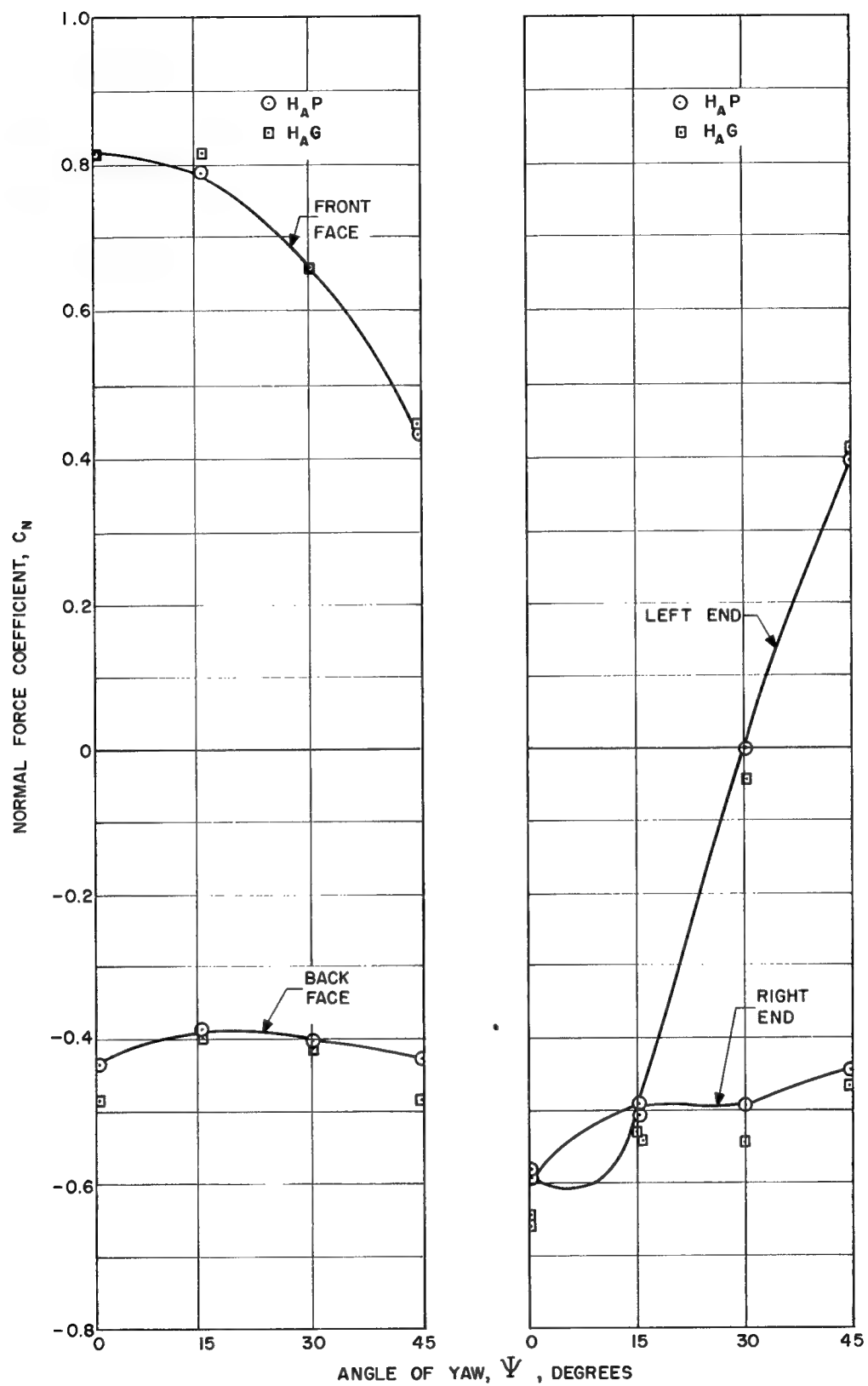


Fig. 53 -- Variation of panel normal force coefficient with yaw angle for  $H_A$  block at  $M \approx 0.2$ , mounting as parameter

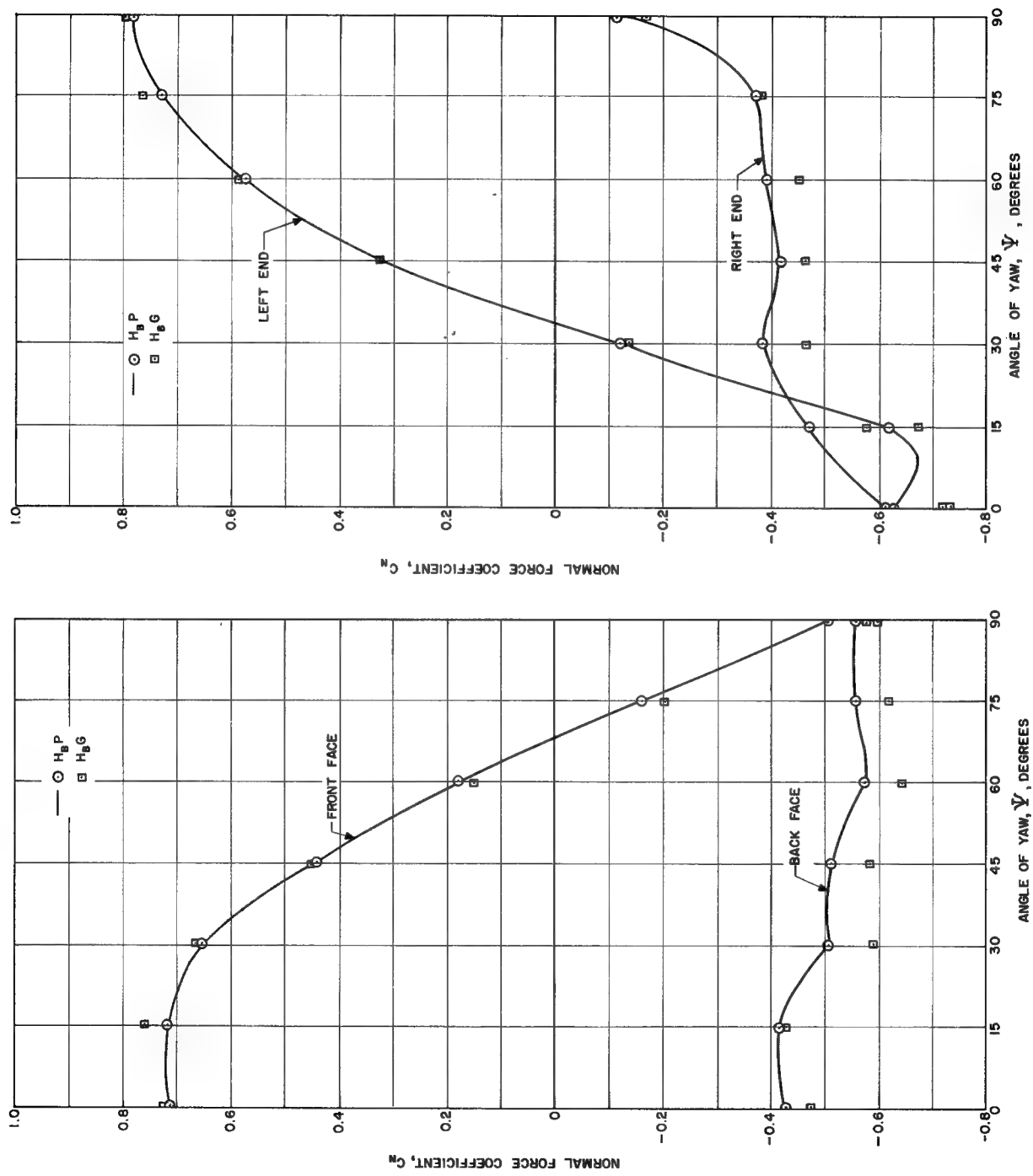


Fig. 54 -- Variation of panel normal force coefficient with yaw angle for  $H_B$  block at  $M \approx 0.2$ , mounting as parameter



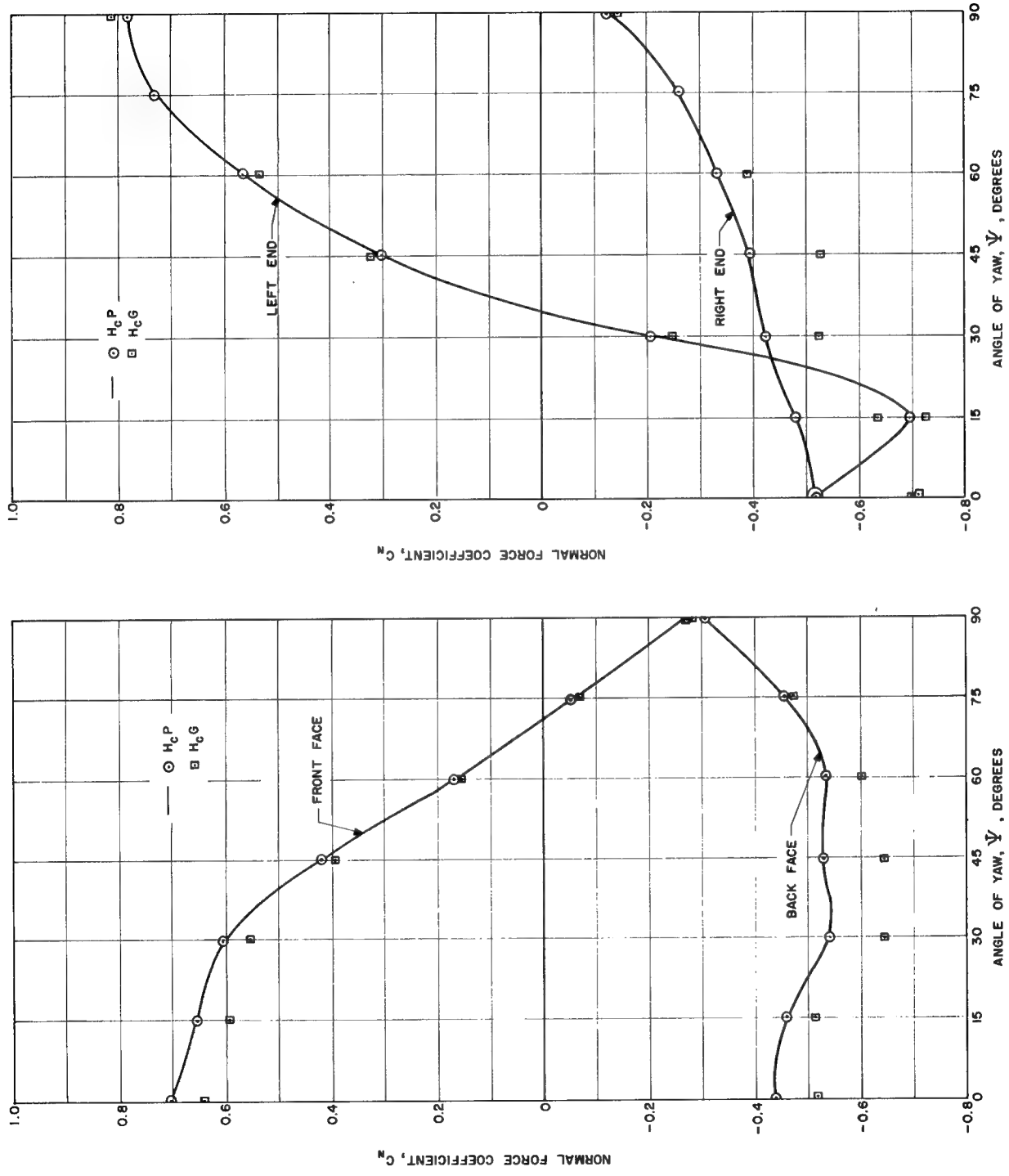


Fig. 55 -- Variation of panel normal force coefficient with yaw angle for  $H_C$  block at  $M \approx 0.2$ , mounting as parameter

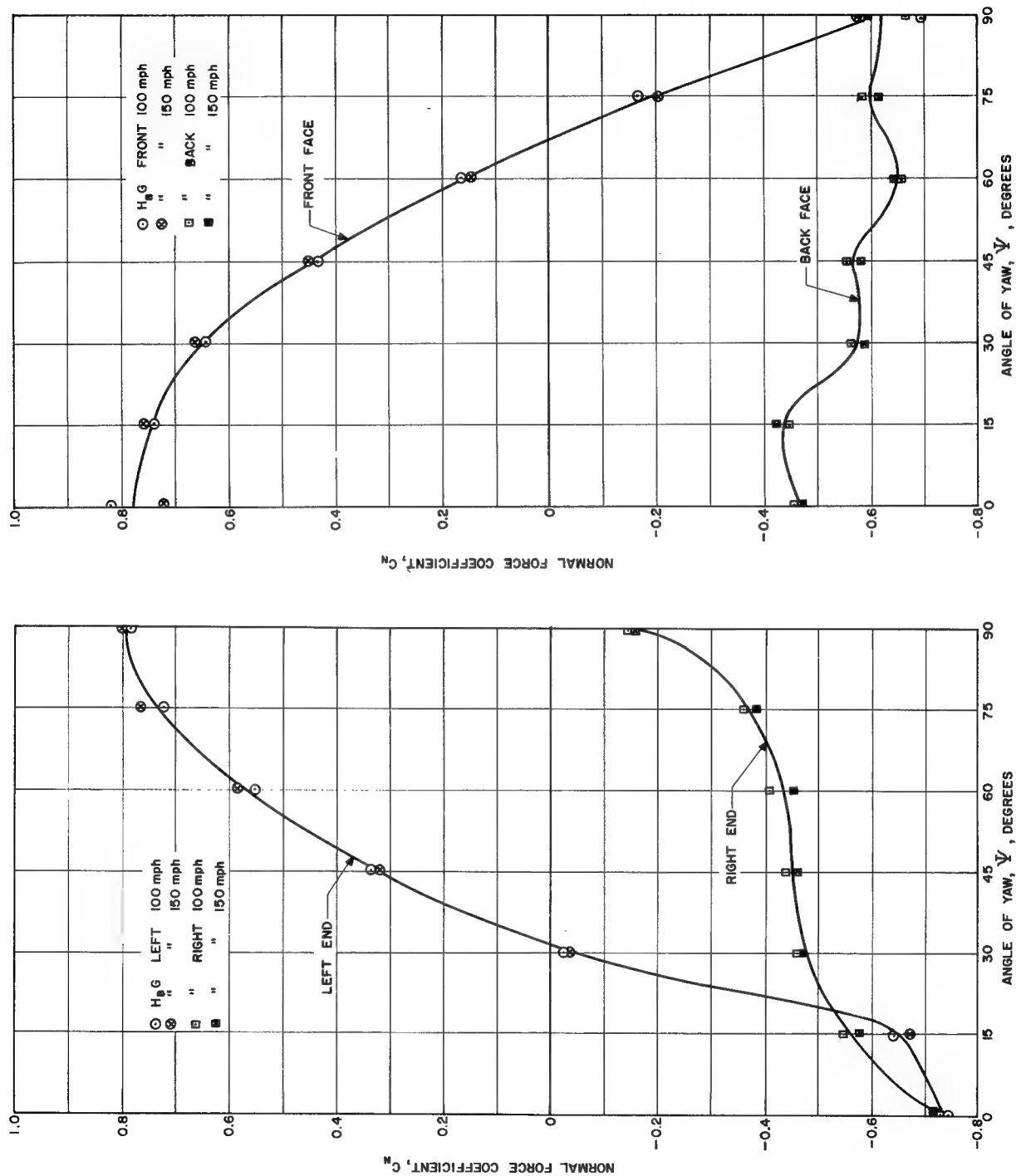


Fig. 56 -- Variation of panel normal force coefficient with yaw angle for H<sub>B</sub>G model at 100 and 150 mph

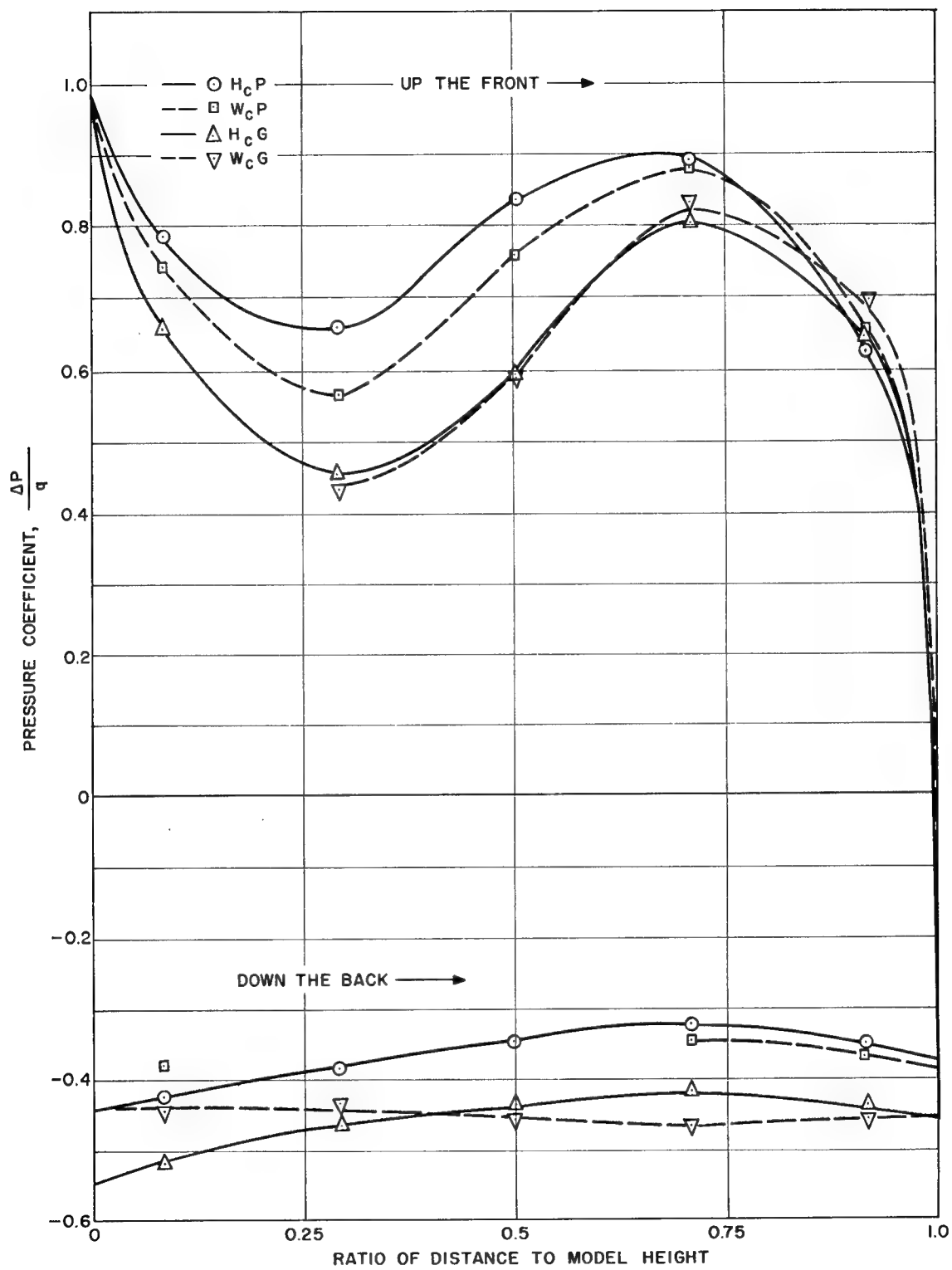


Fig. 57 -- Vertical centerline pressure distribution on wall ( $W_C$ ) and  $H_C$  block at  $M \approx 0.2$ , mounting as a parameter

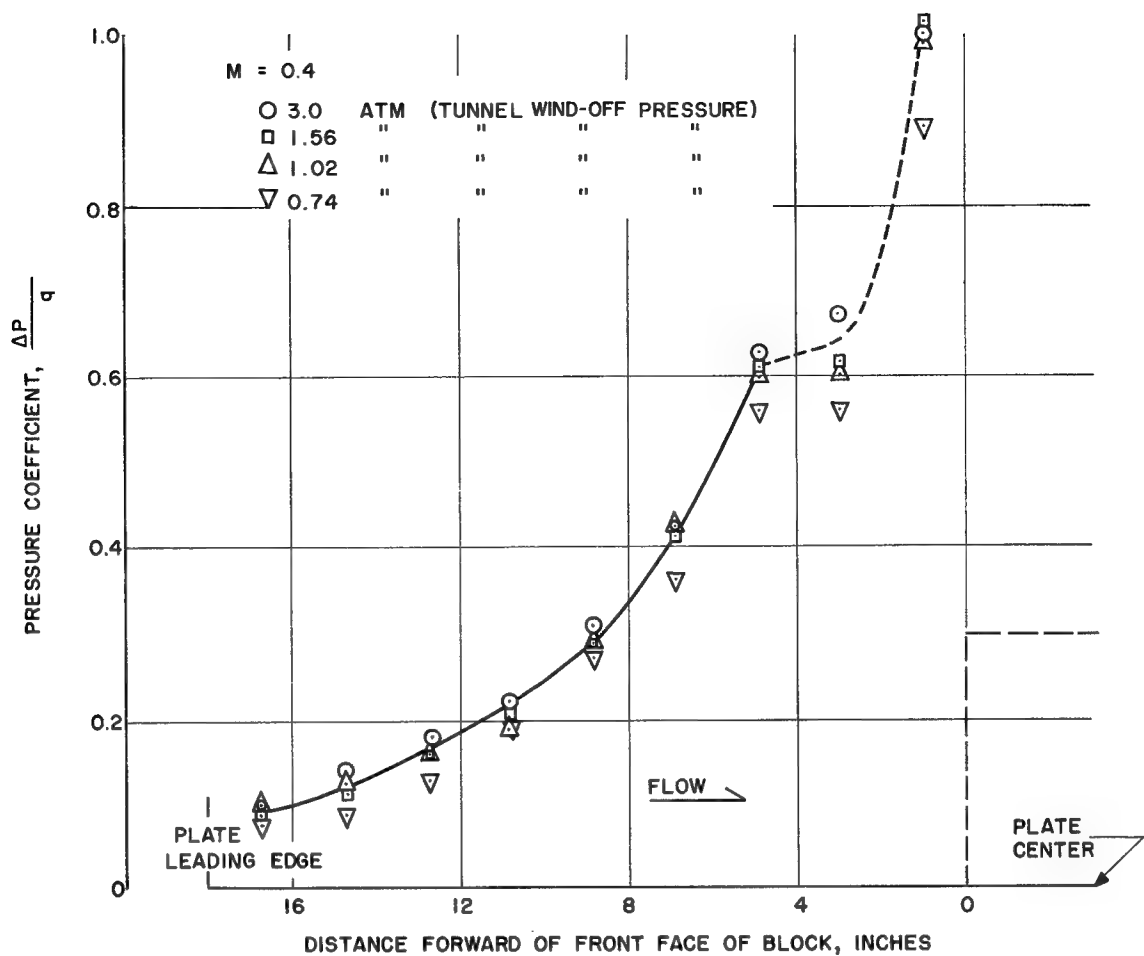


Fig. 58 -- Pressure distribution on mounting plate forward of  $H_A$  block in CWT test at  $M = 0.4$ , tunnel pressure as parameter

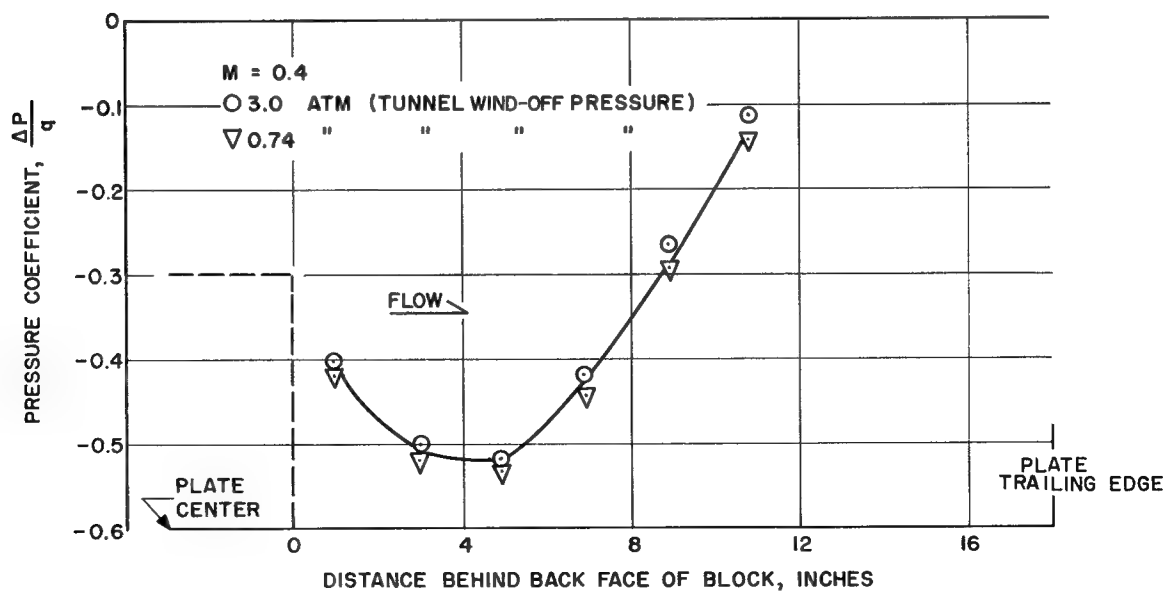


Fig. 59 -- Pressure distribution on mounting plate behind  $H_A$  block in CWT test at  $M = 0.4$ , tunnel pressure as parameter

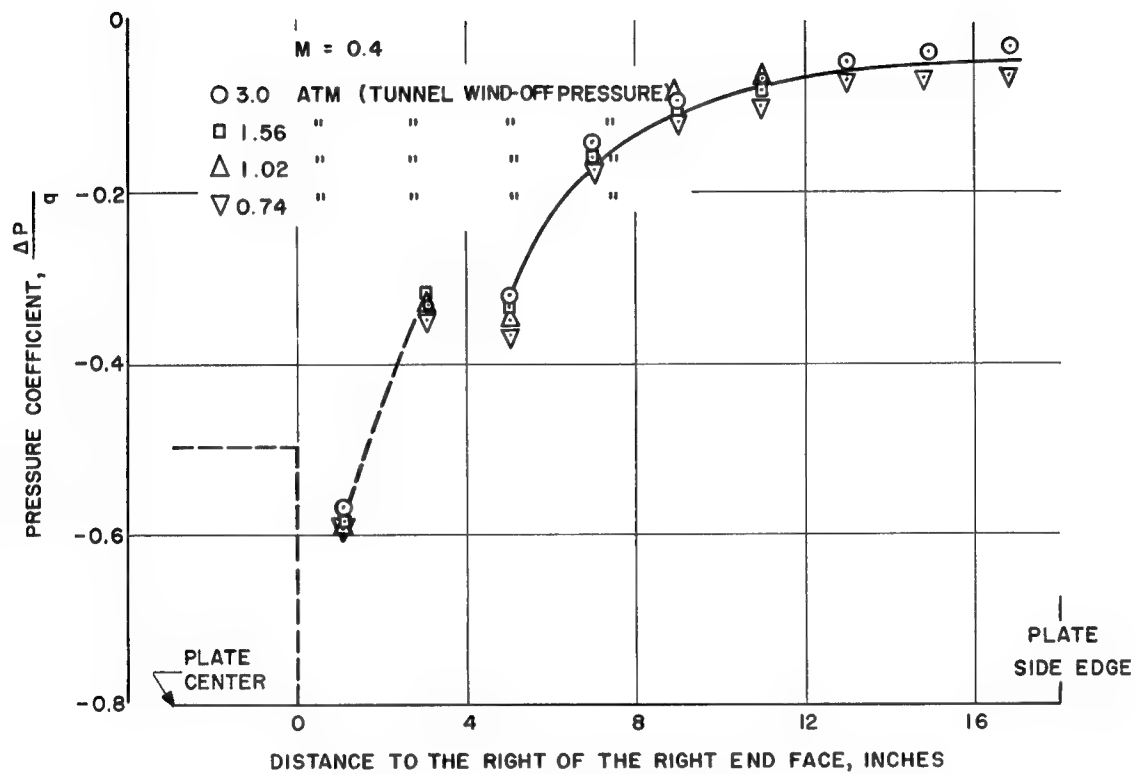


Fig. 60 -- Pressure distribution on mounting plate to the right of  $H_A$  block in CWT test at  $M = 0.4$ , tunnel pressure as parameter

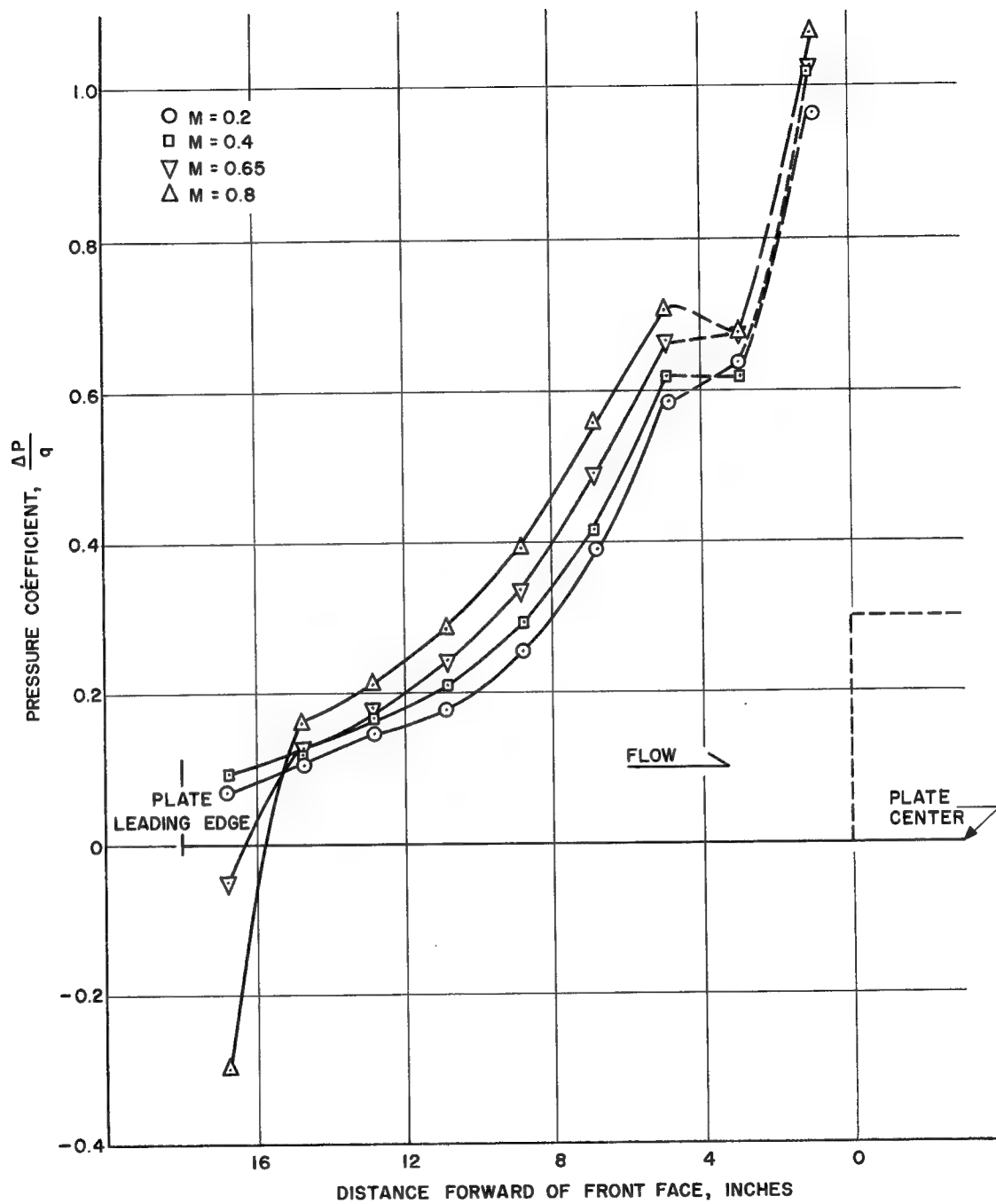


Fig. 61 -- Pressure distribution on mounting plate forward of HA block in CWT test, Mach number as parameter

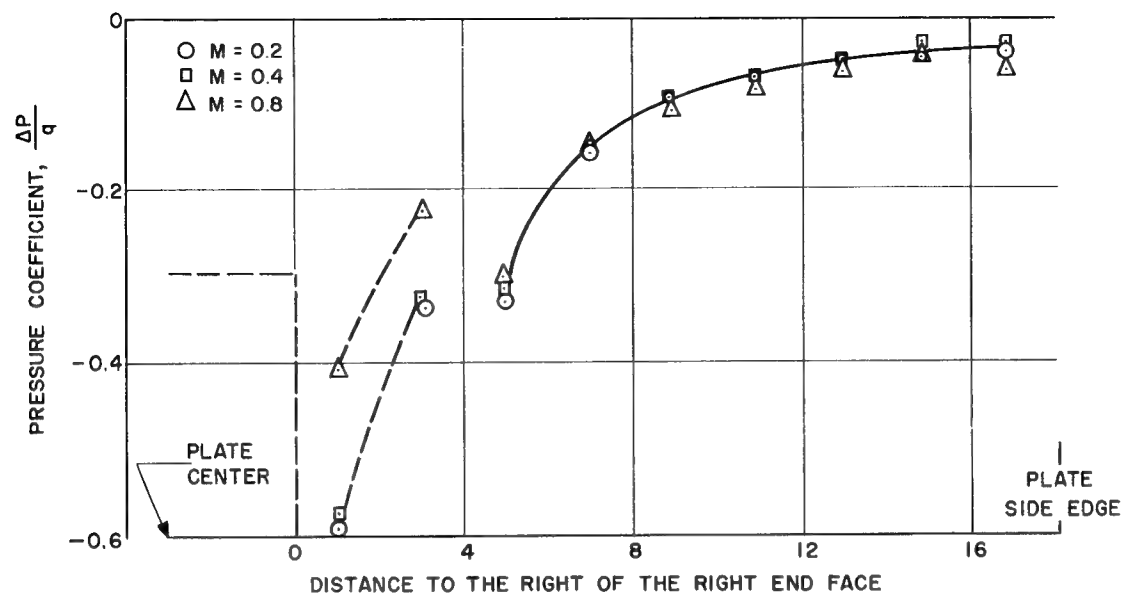


Fig. 62 -- Pressure distribution on mounting plate to the right of the  $H_A$  block in CWT test, Mach number as parameter

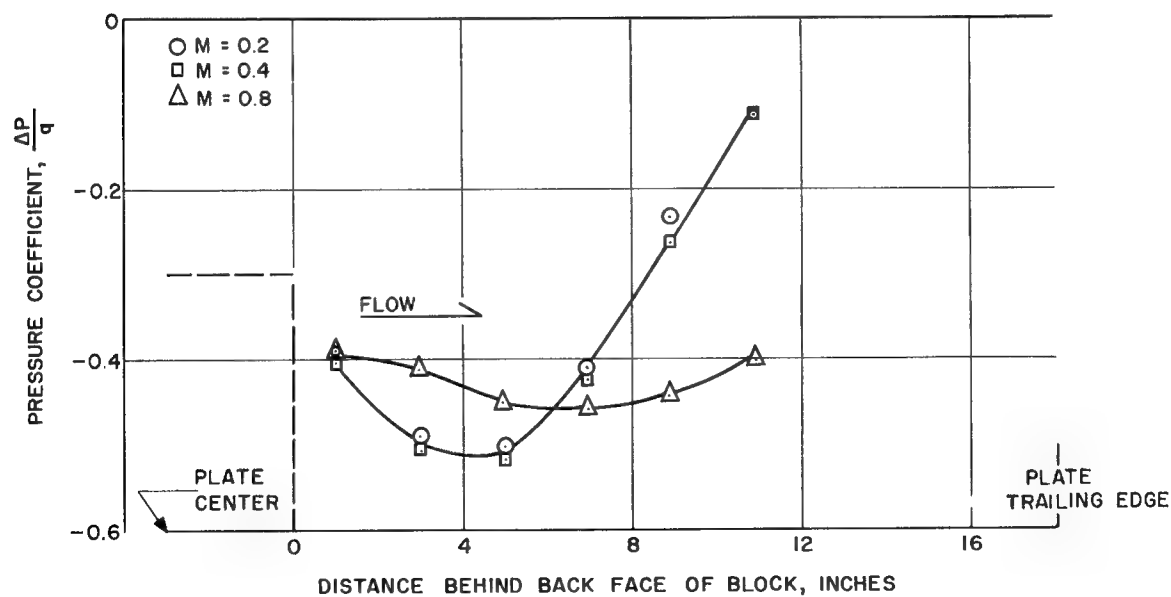


Fig. 63 -- Pressure distribution on mounting plate behind the  $H_A$  block in CWT test, Mach number as parameter

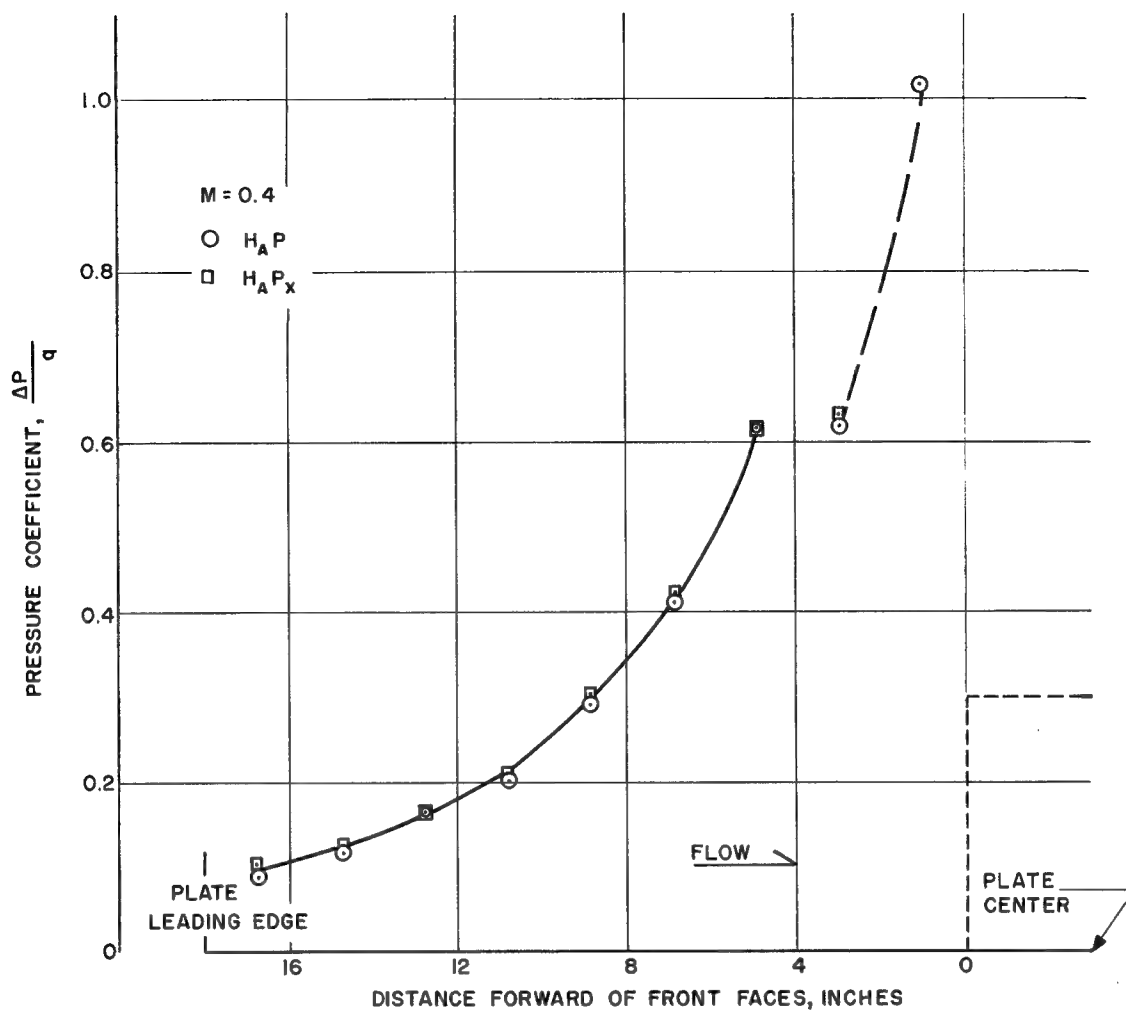


Fig. 64 -- Pressure distribution on mounting plate forward of  $H_A$  block in CWT test at  $M = 0.4$ , mounting as parameter

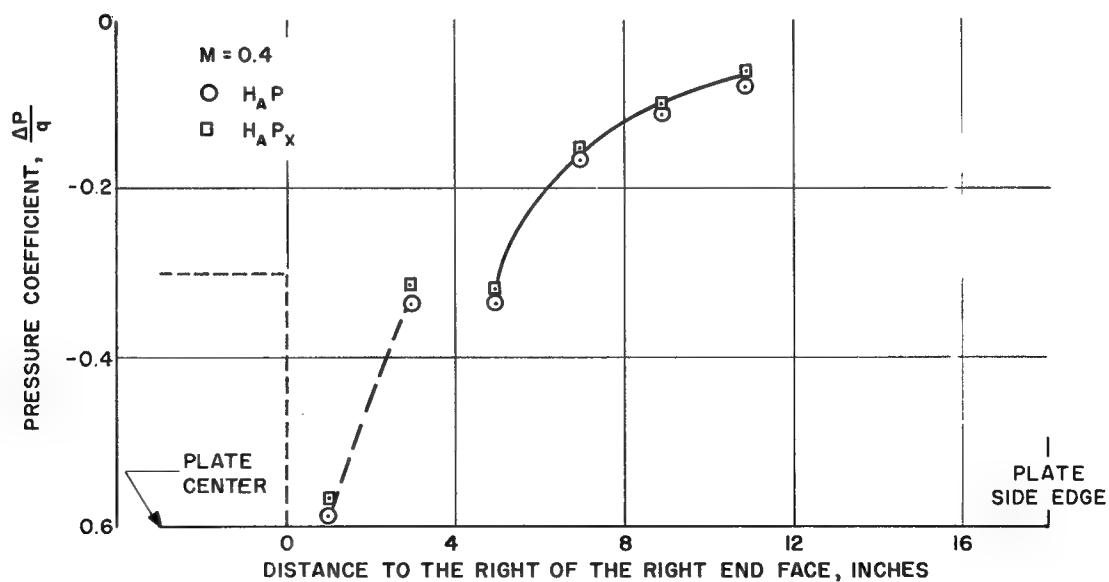


Fig. 65 -- Pressure distribution on mounting plate forward of  $H_A$  block in CWT test at  $M = 0.4$ , mounting as parameter



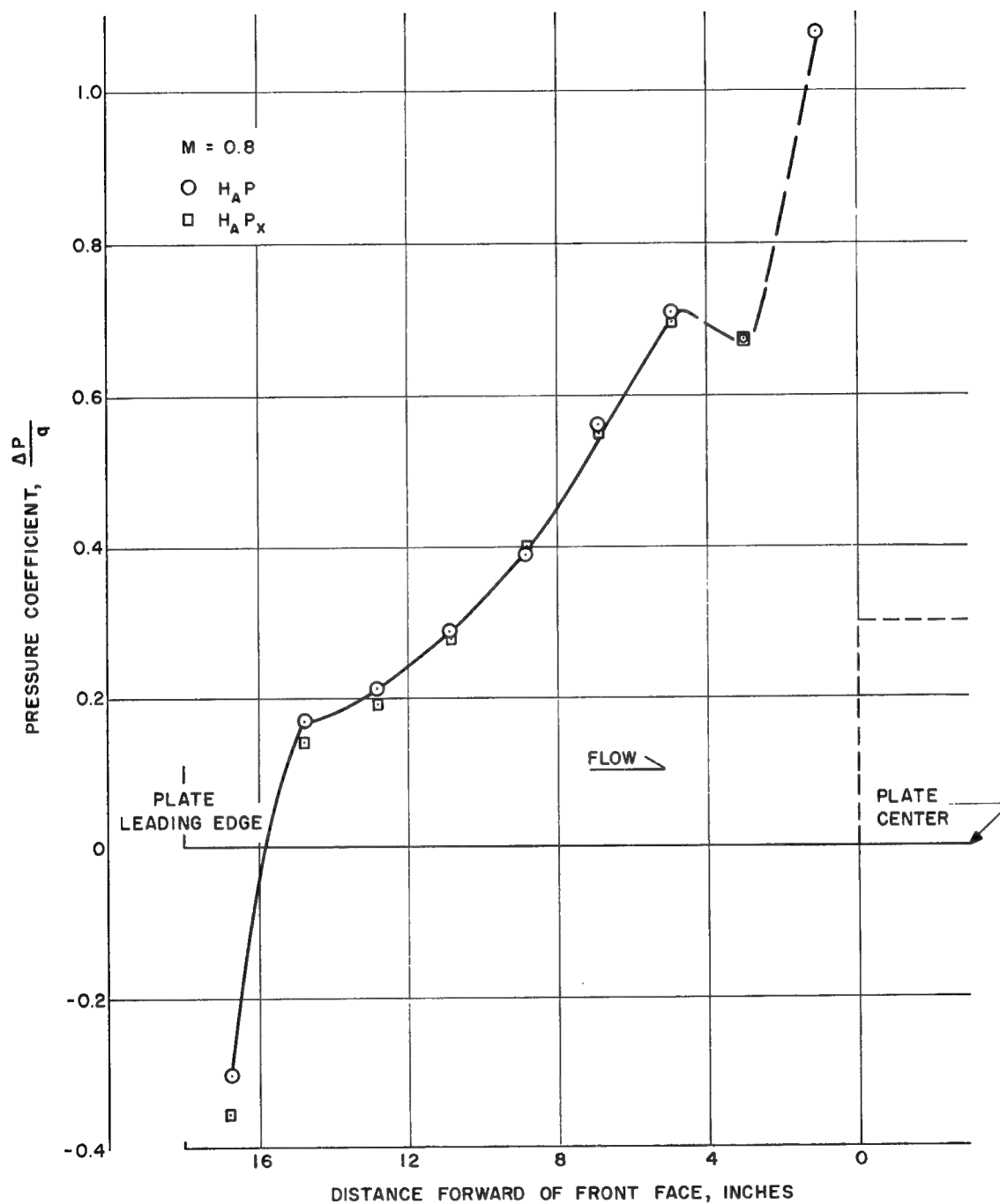


Fig. 66 -- Pressure distribution on mounting plate forward of  $H_A$  block in CWT test at  $M = 0.8$ , mounting as parameter

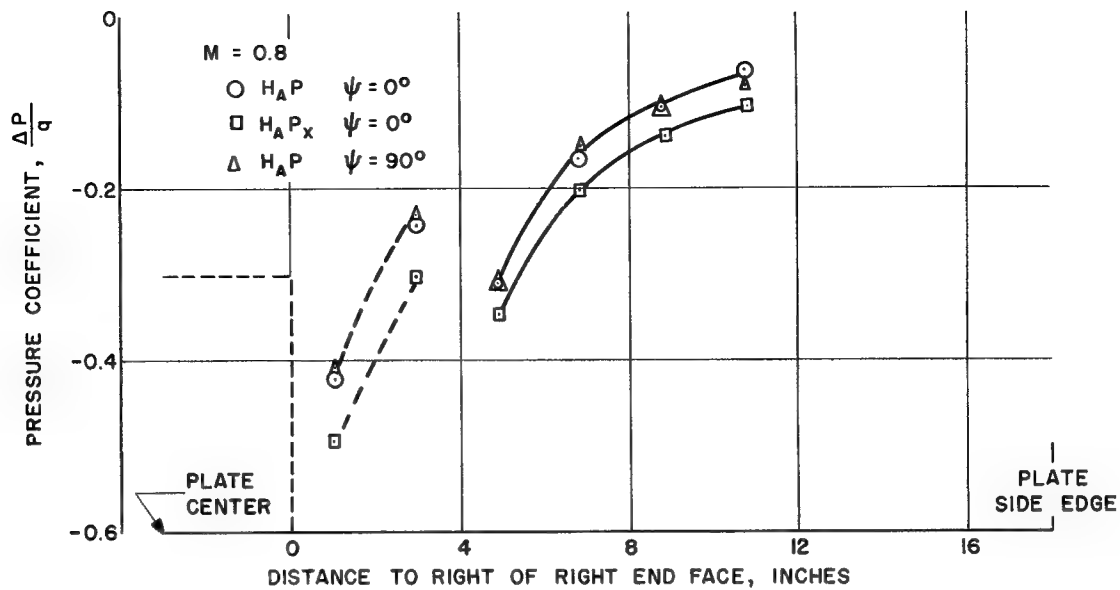


Fig. 67 -- Pressure distribution on mounting plate to right of  $H_A$  block in CWT tests at  $M = 0.8$ , mounting as parameter

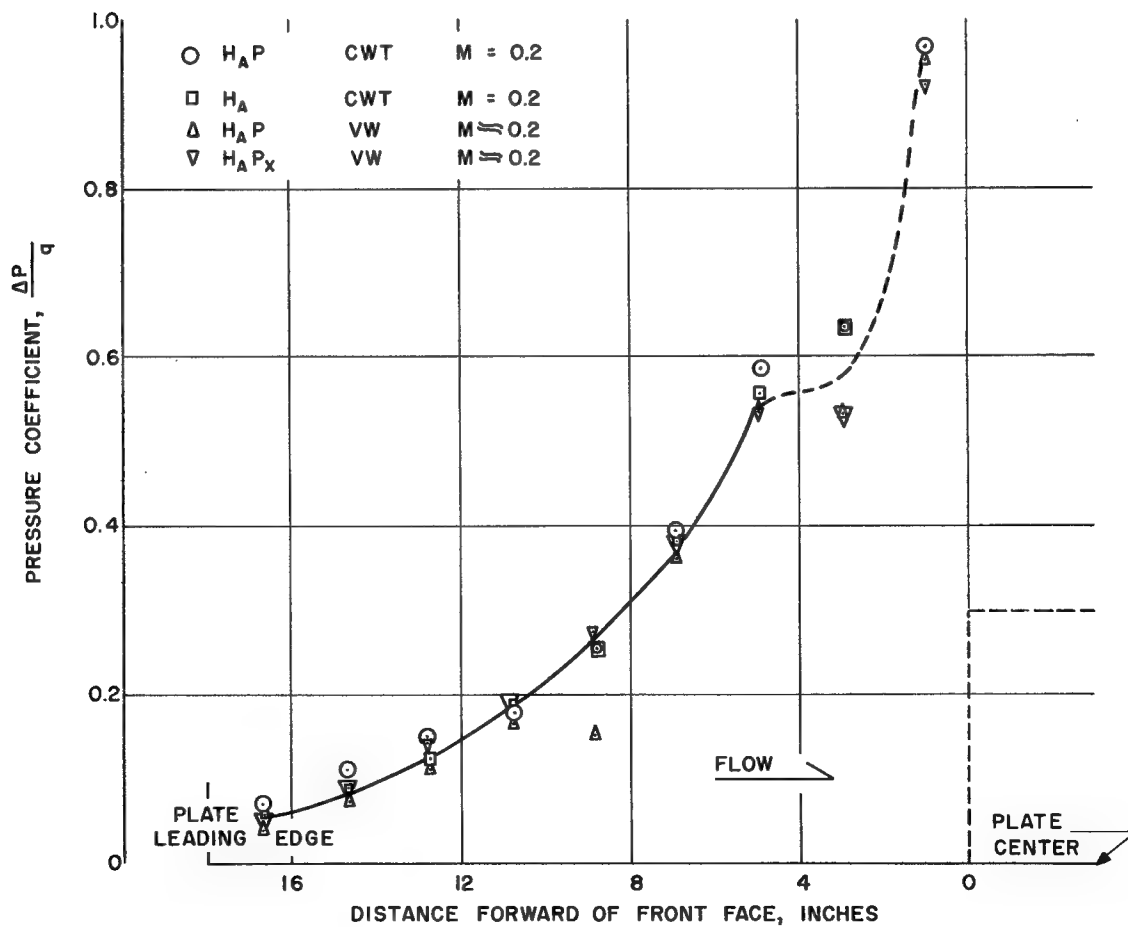


Fig. 68 -- Pressure distribution on mounting plate forward of  $H_A$  block in CWT and UW tunnel at  $M = 0.2$ , mounting as a parameter

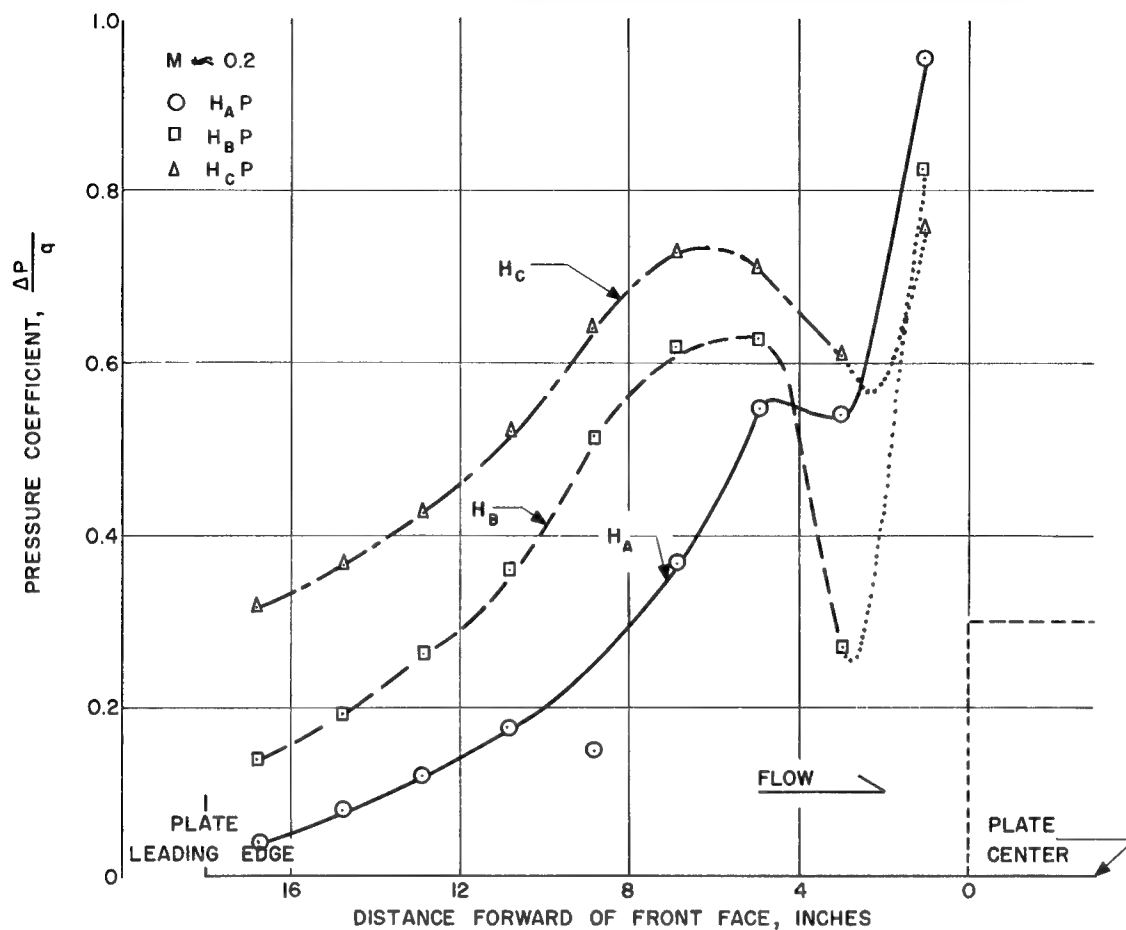


Fig. 69 -- Pressure distribution on mounting plate forward of block in UW tunnel at  $M \approx 0.2$ , block form as parameter

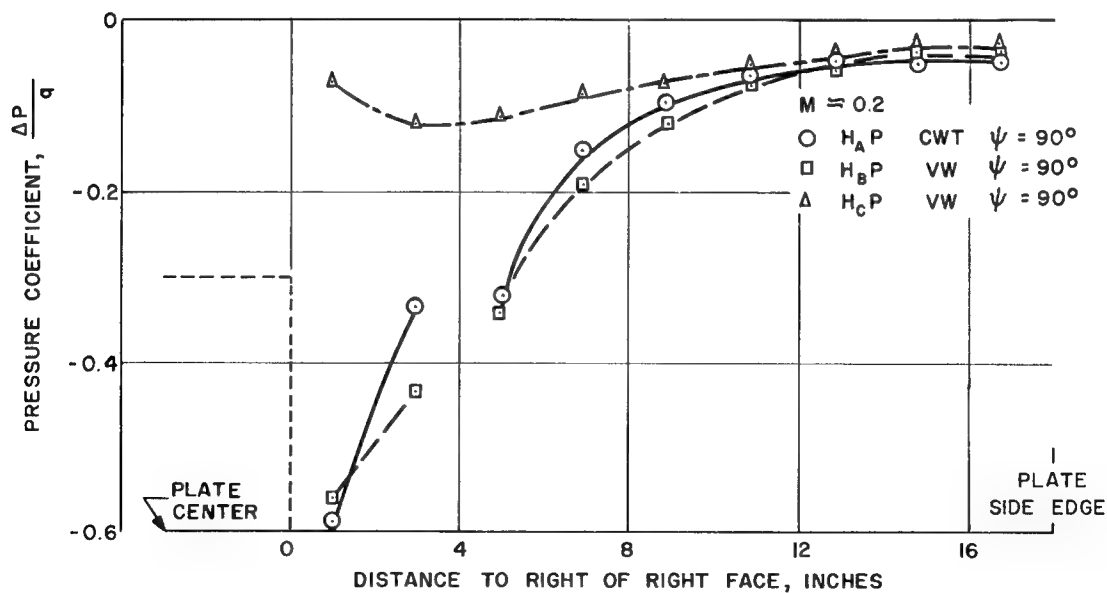


Fig. 70 -- Pressure distribution on mounting plate to right of block at  $M \approx 0.2$ ,  $\psi = 90^\circ$ , block form as parameter

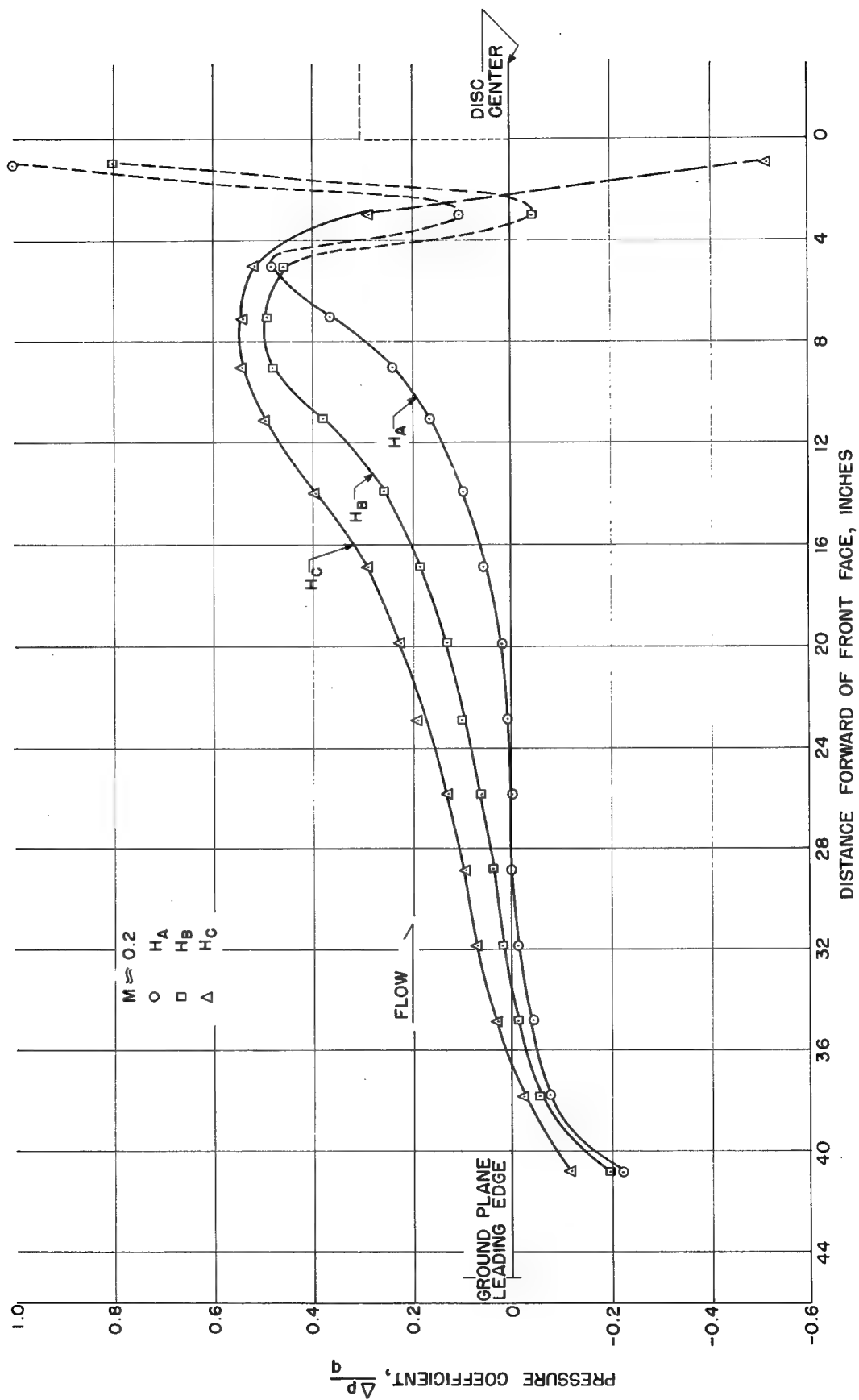


Fig. 71 -- Pressure distribution on ground plane forward of block in UW tunnel at  $M \approx 0.2$ , block form as parameter,  $\psi = 0^\circ$

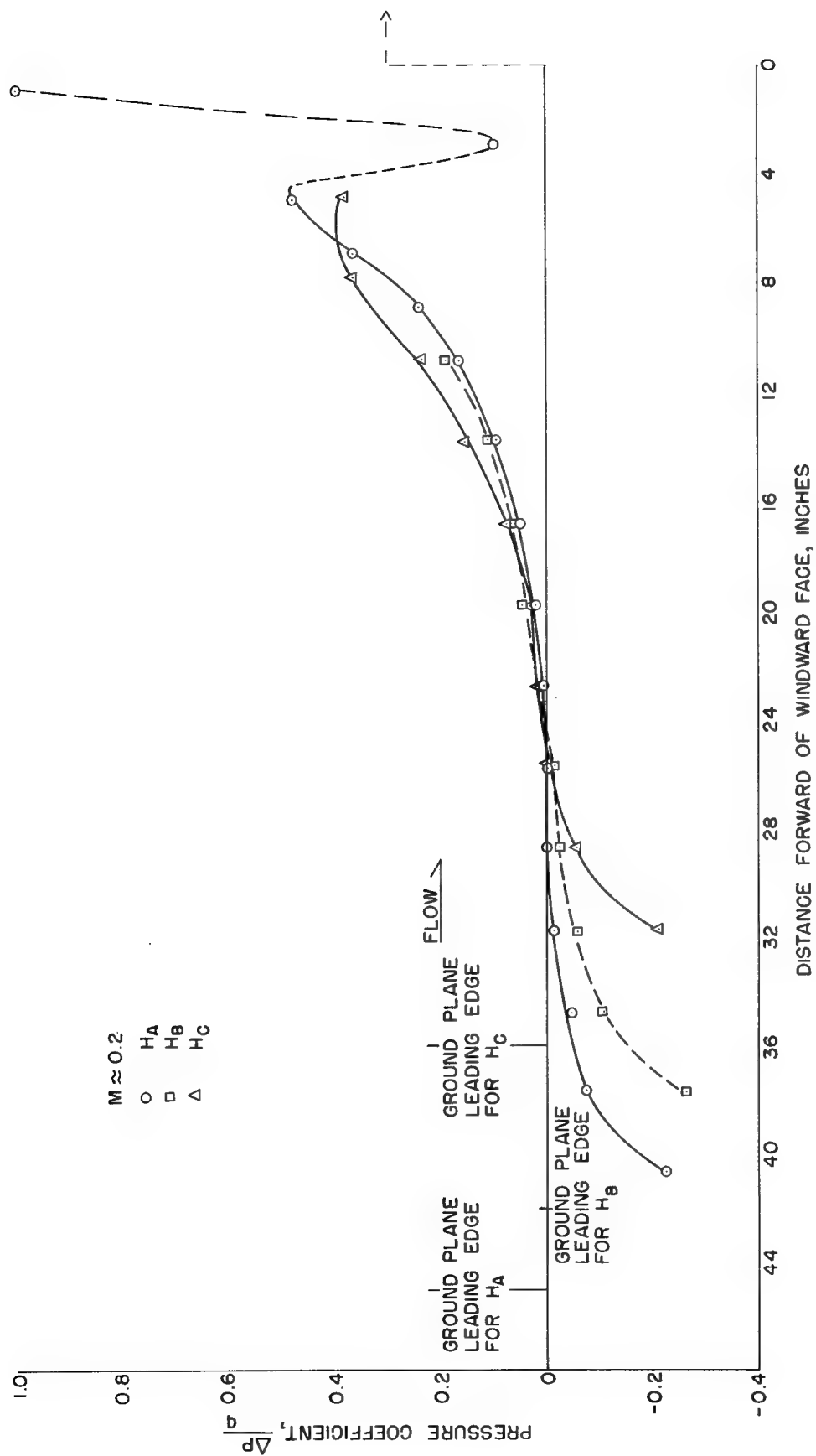


Fig. 72 -- Pressure distribution on ground plane forward of block in UW tunnel at  $M \approx 0.2$ , block form as parameter,  $\psi = 90^\circ$

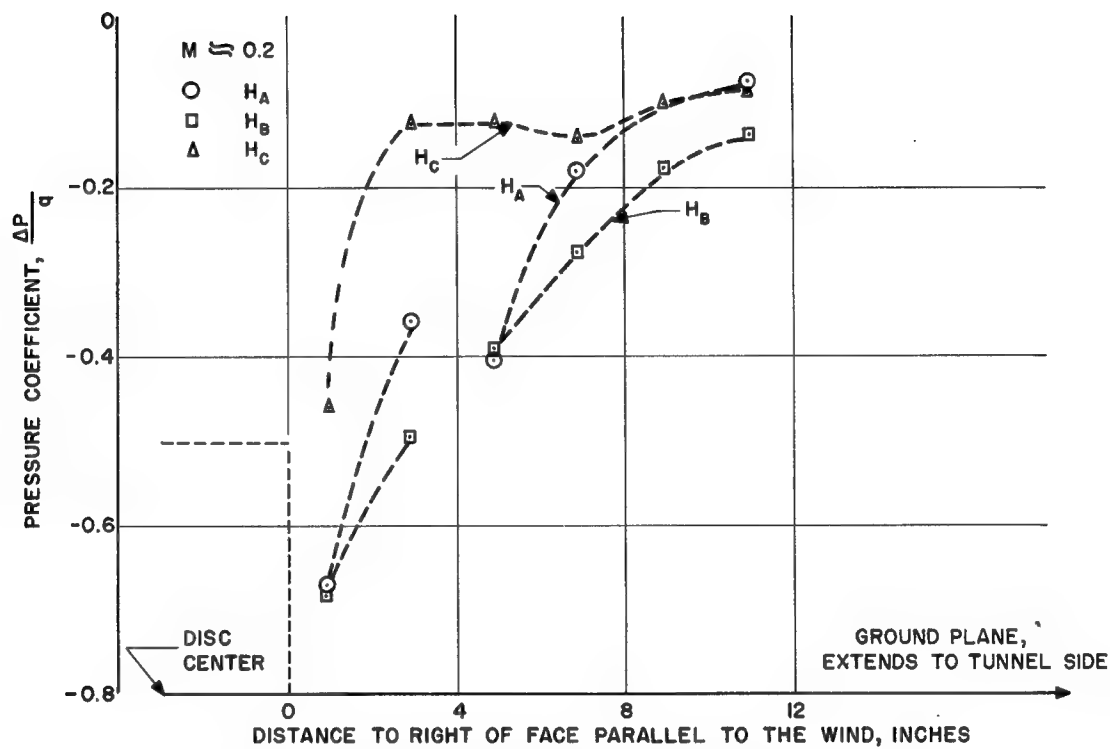


Fig. 73 -- Pressure distribution on ground plane to right of block in UW tunnel at  $M \approx 0.2$ , block form as parameter,  $\psi = 90^\circ$

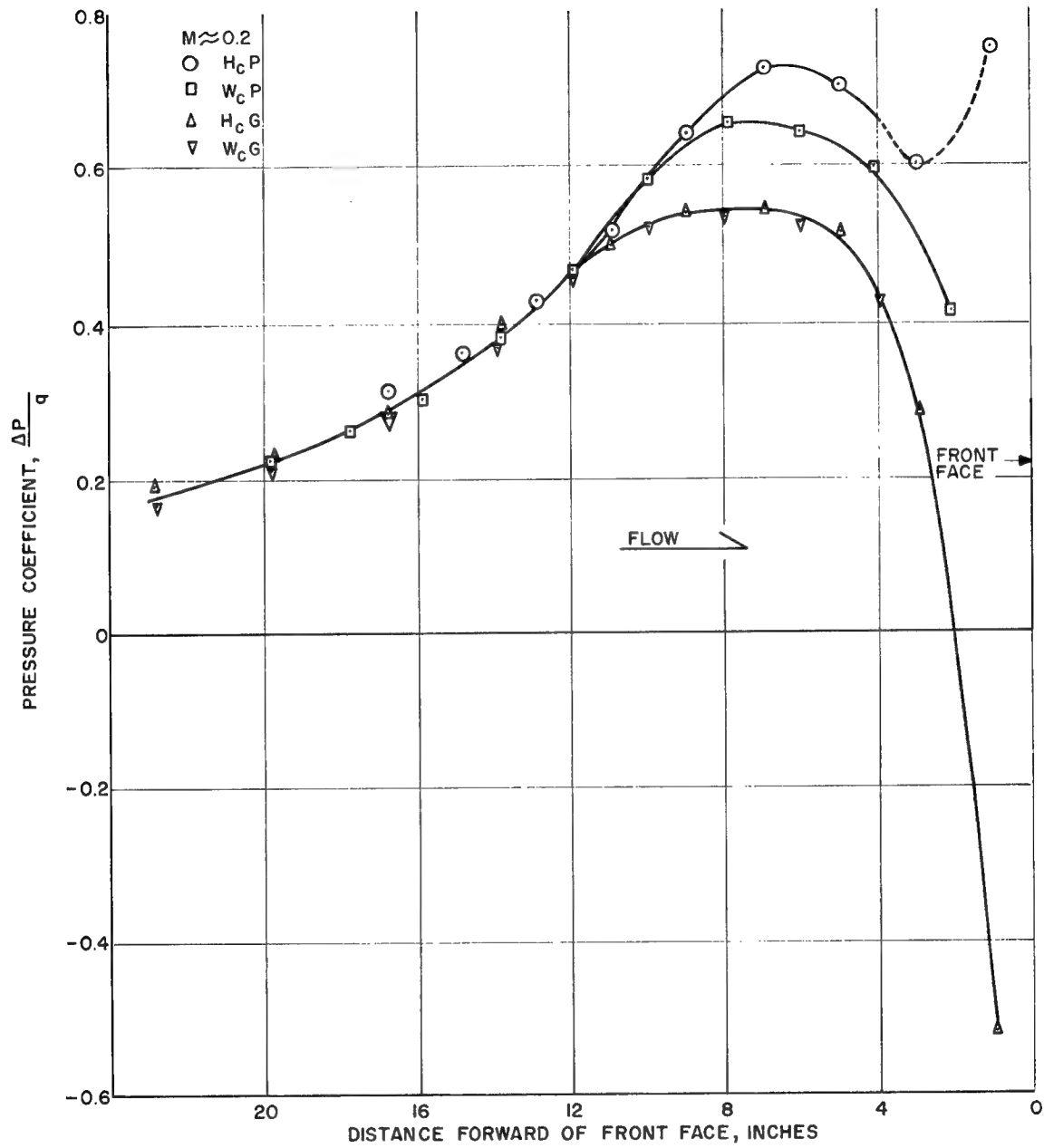


Fig. 74 -- Pressure distribution on mounting forward of  $H_c$  and  $W_c$  in UW tunnel at  $M \approx 0.2$ , model as parameter

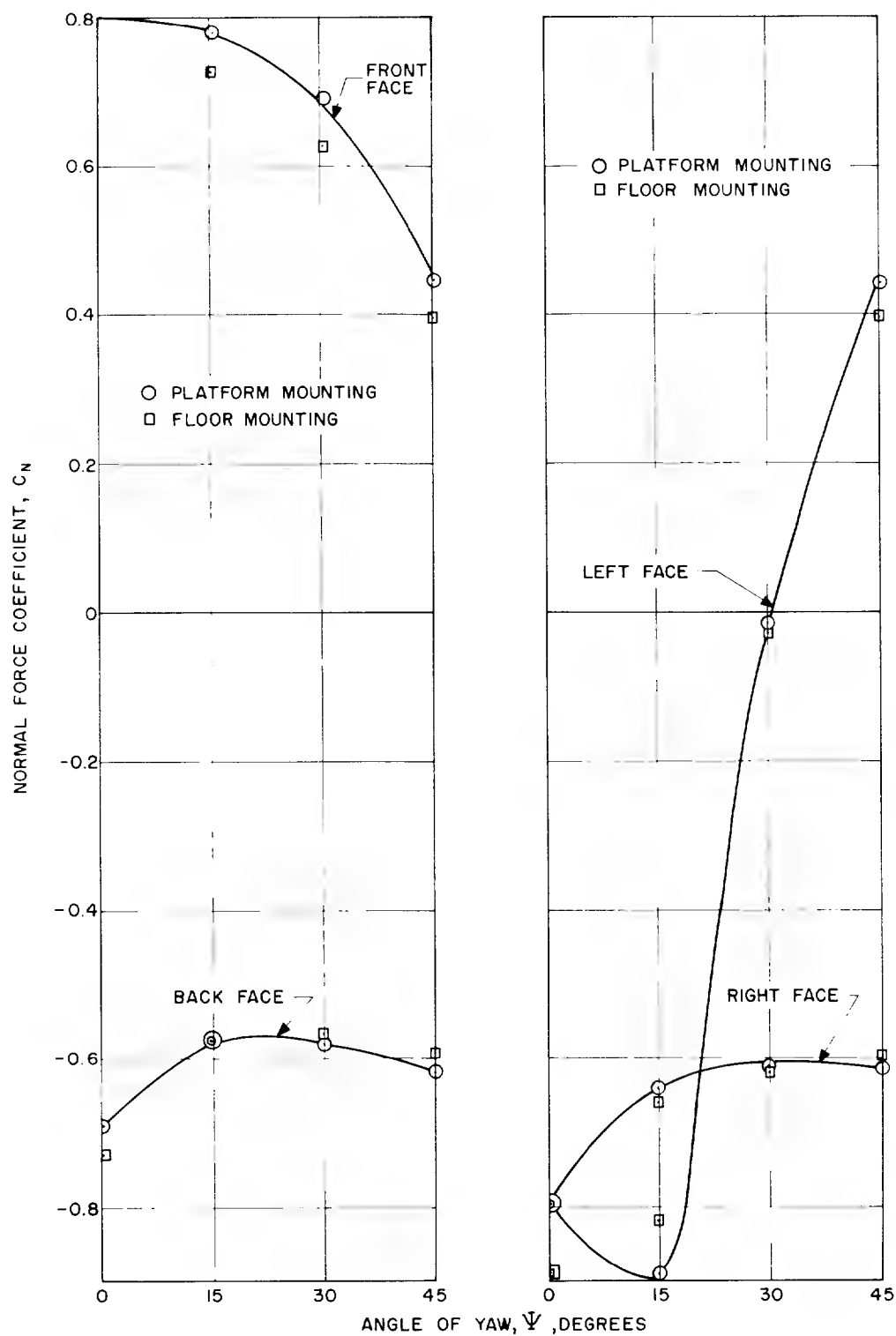


Fig. 75 -- Variation of panel normal force coefficient with yaw angle on square base prism (1:1:3.07) in NBS test, mounting as parameter (data from Reference 4).



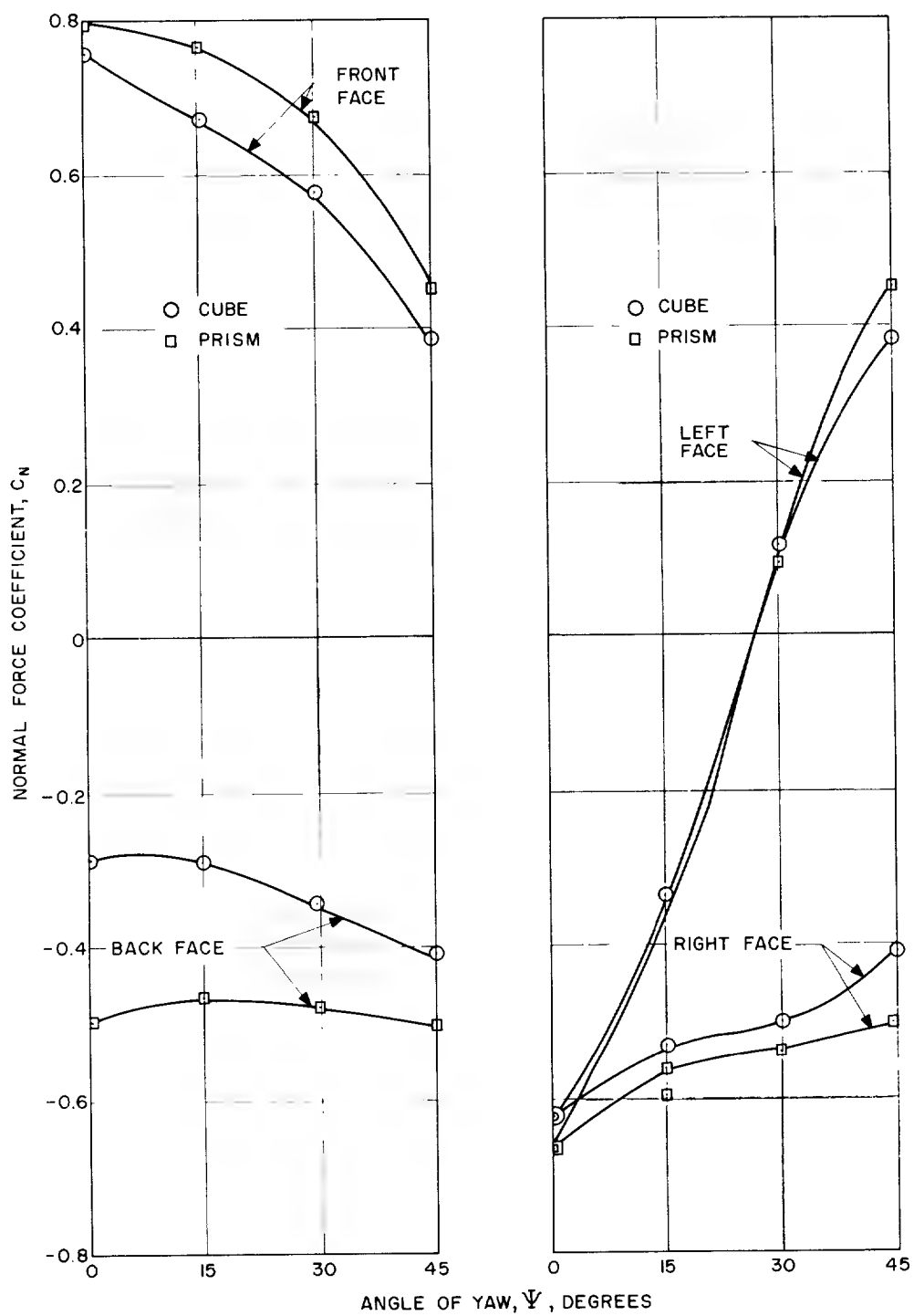


Fig. 76 -- Variation of panel normal force coefficient with yaw angle on cube and square base prism (1:1:2.47) in Denmark test (data from Reference 5).

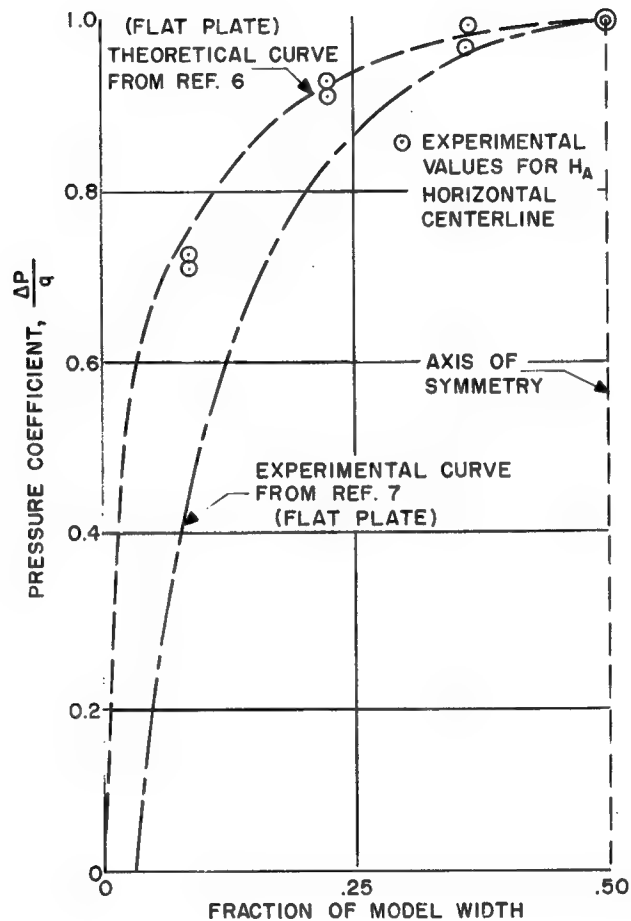


Fig. 77 -- Comparison of horizontal centerline pressure distribution on the mounted cube with the theoretical and experimental distributions for a flat plate.

## APPENDIX

A series of contour maps, indexed in Table A-I, show the variation of the complete pressure distribution on each block form with yaw angle at a constant Mach number and with Mach number at zero yaw. The center of pressure on each face has been located so that its movement may be followed.

Figure A-1 (a, b, and f) shows the variation of pressure contour with Mach number on the cube for the unyawed orientation. Figure A-1 (b to e) gives the variation of pressures as the cube is turned through an angle of 45 degrees at Mach number 0.4. Figure A-1 (b and g) shows the effect of the leeward extension plane.

Figure A-2 (a to f) gives the variation of pressure distribution with orientation of the 1:1:2 block form. Figure A-2 (a and g) shows the variation of pressure distribution with Mach number.

Figure A-3 (a and i) shows the Mach-number effects on pressure distribution on the 1:1:4 block. Figure A-3 (b to h) illustrates the pressure changes with respect to orientation of the block. Since plate-mounting data were unavailable for zero yaw at Reynolds and Mach numbers corresponding to those in Figure A-3 (c to h), data for the plate-plus-extension mounting have been included as Figure A-3b. Front-face contours should be similar for the two mountings. However, magnitudes of negative pressures are not necessarily the same.

TABLE A-I

Cross Index for Contour Maps

Model	Yaw Angle = 0°			Mach Number = 0.4							
	Mach Number			Yaw Angle							
	0.2	0.4	0.65	0°	15°	30°	45°	60°	75°	90°	
H <sub>A</sub> P	Fig. A-1a	Fig. A-1b	Fig. A-1f	Fig. A-1b	Fig. A-1c	Fig. A-1d	Fig. A-1e				
H <sub>A</sub> P <sub>X</sub>		Fig. A-1g		Fig. A-1g							
H <sub>B</sub> P		Fig. A-2a	Fig. A-2g	Fig. A-2a	Fig. A-2b	Fig. A-2c	Fig. A-2d		Fig. A-2e	Fig. A-2f	
H <sub>B</sub> P <sub>X</sub>											
H <sub>C</sub> P	Fig. A-3a		Fig. A-3c		Fig. A-3c	Fig. A-3d	Fig. A-3e	Fig. A-3f	Fig. A-3g	Fig. A-3h	
H <sub>C</sub> P <sub>X</sub>		Fig. A-3b		Fig. A-3b							

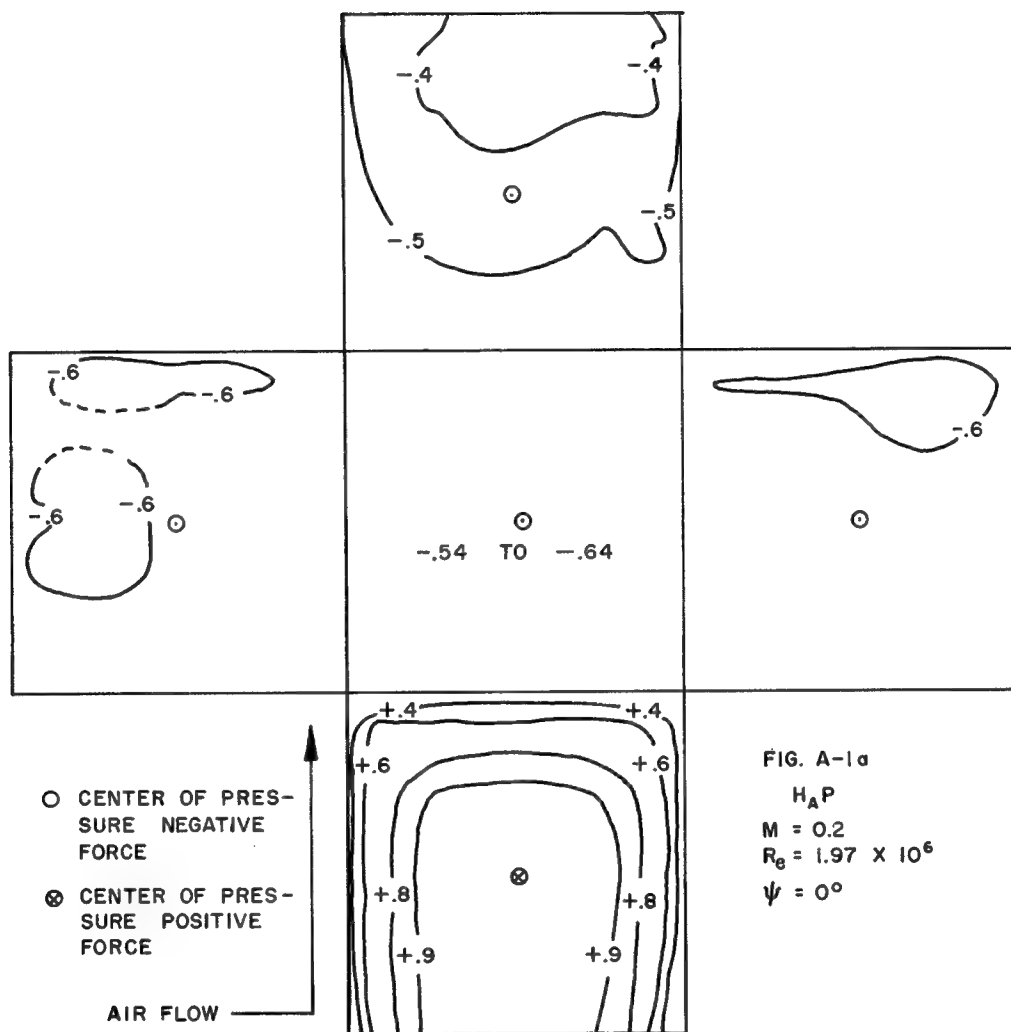


Fig. A.1 -- Pressure contours on 1:1:1 block form

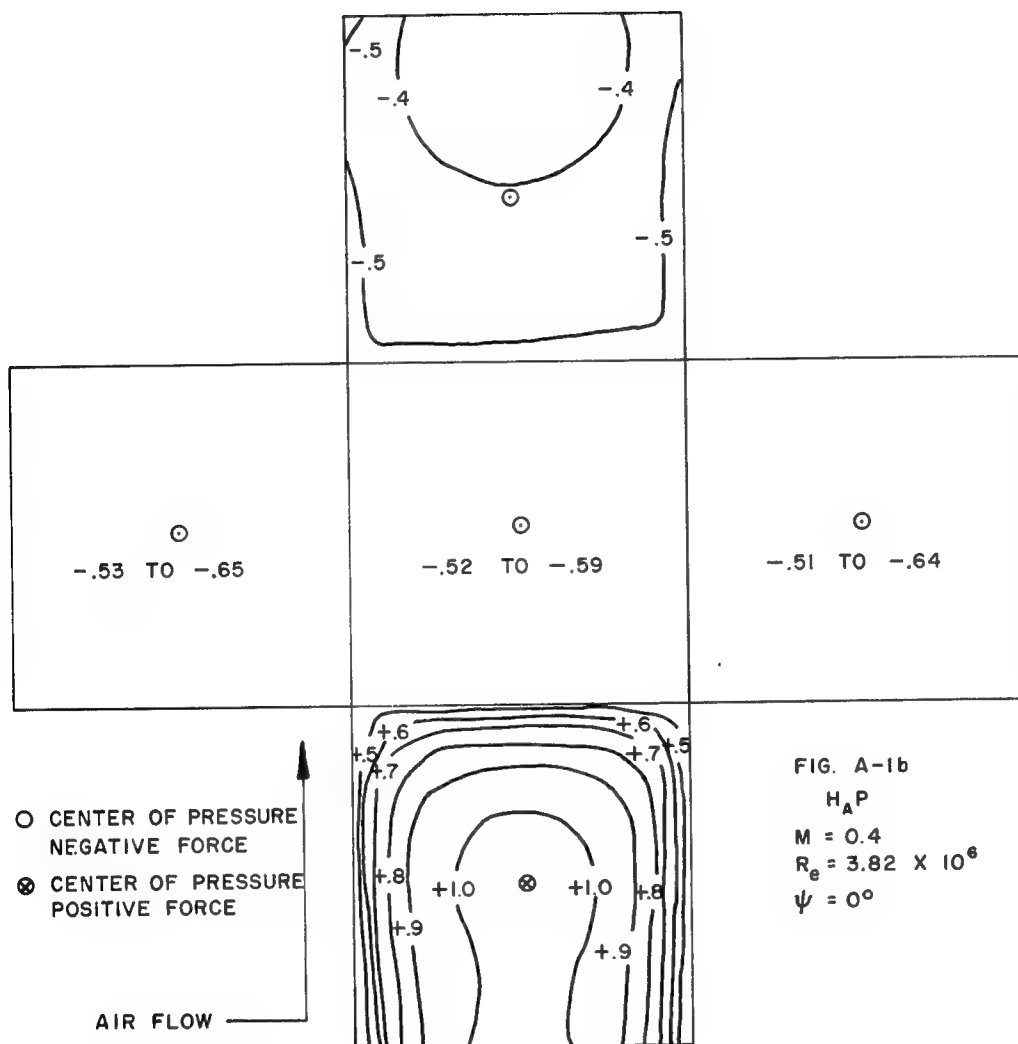


Fig. A.1 (continued)

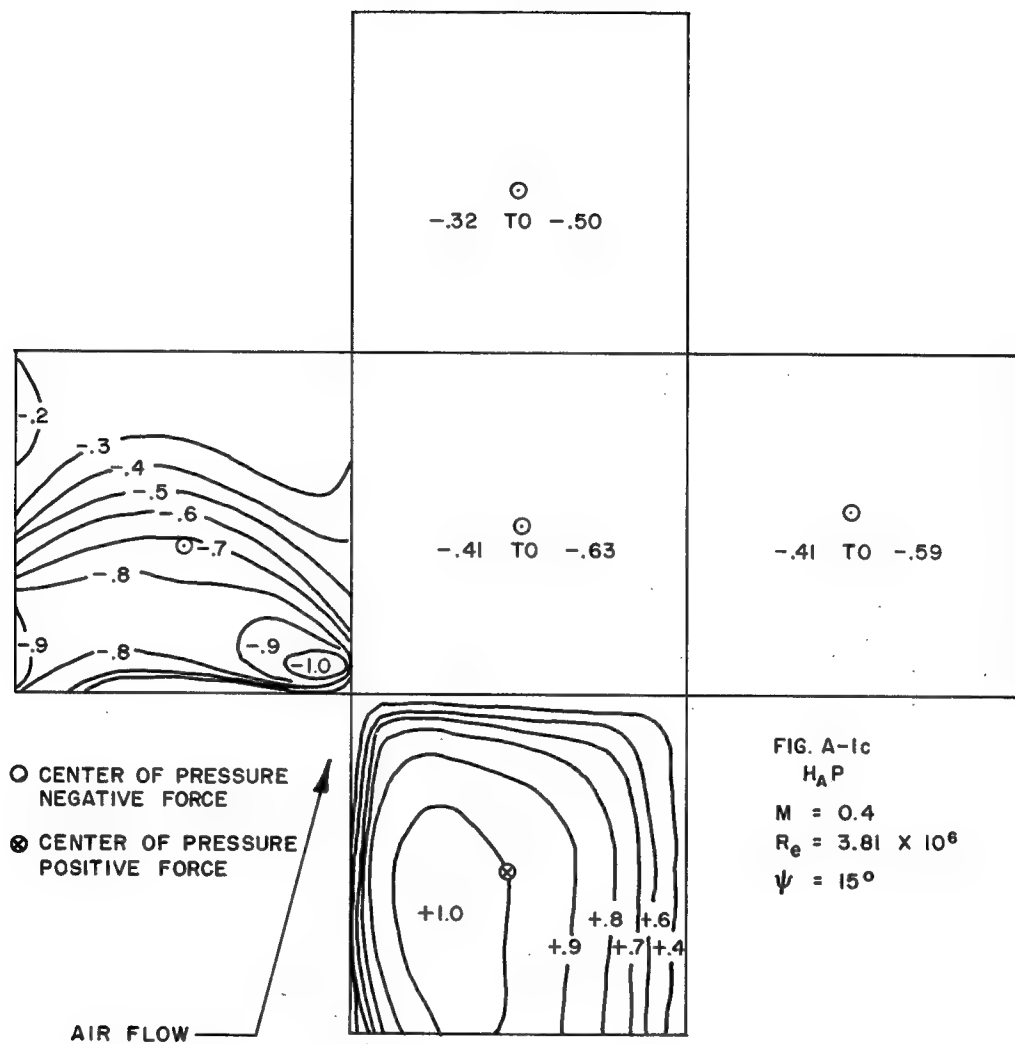


Fig. A.1 (continued)

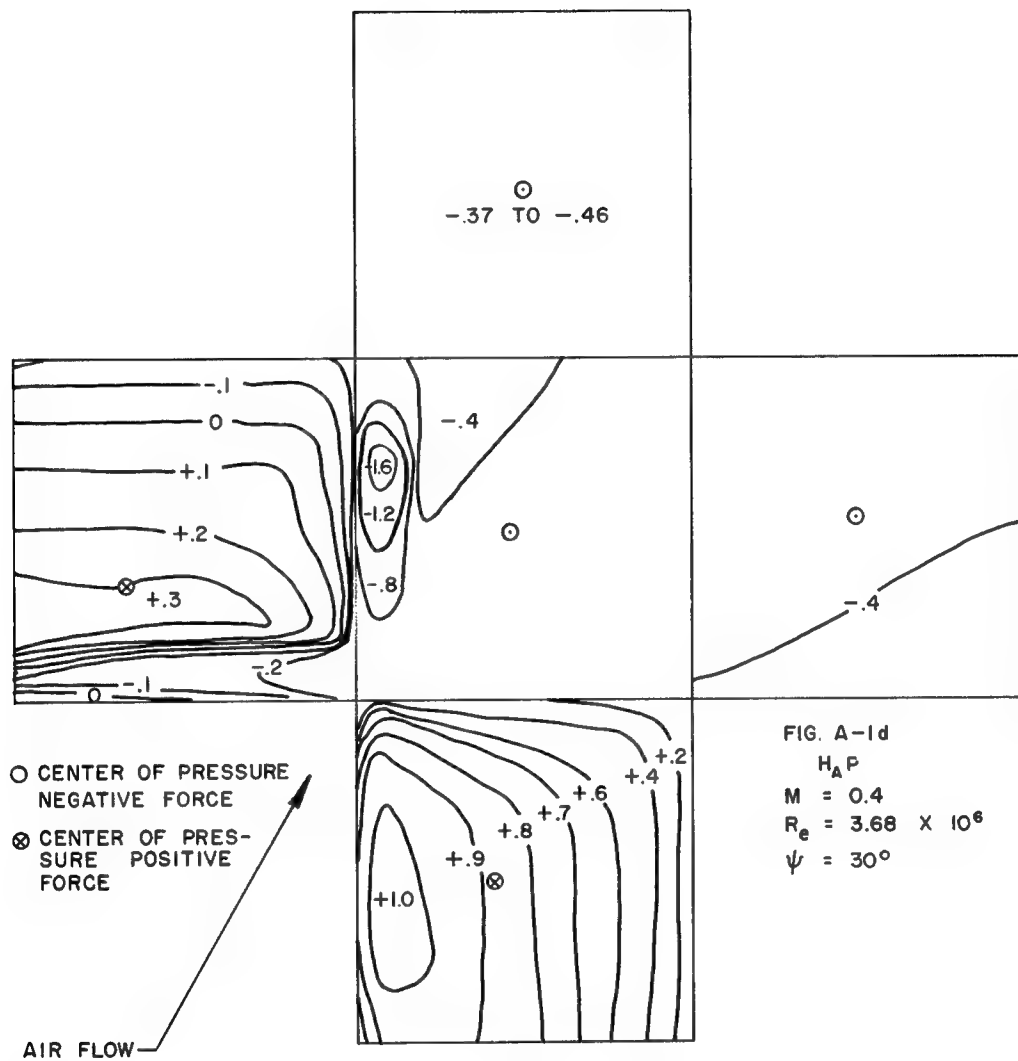


Fig. A.1 (continued)



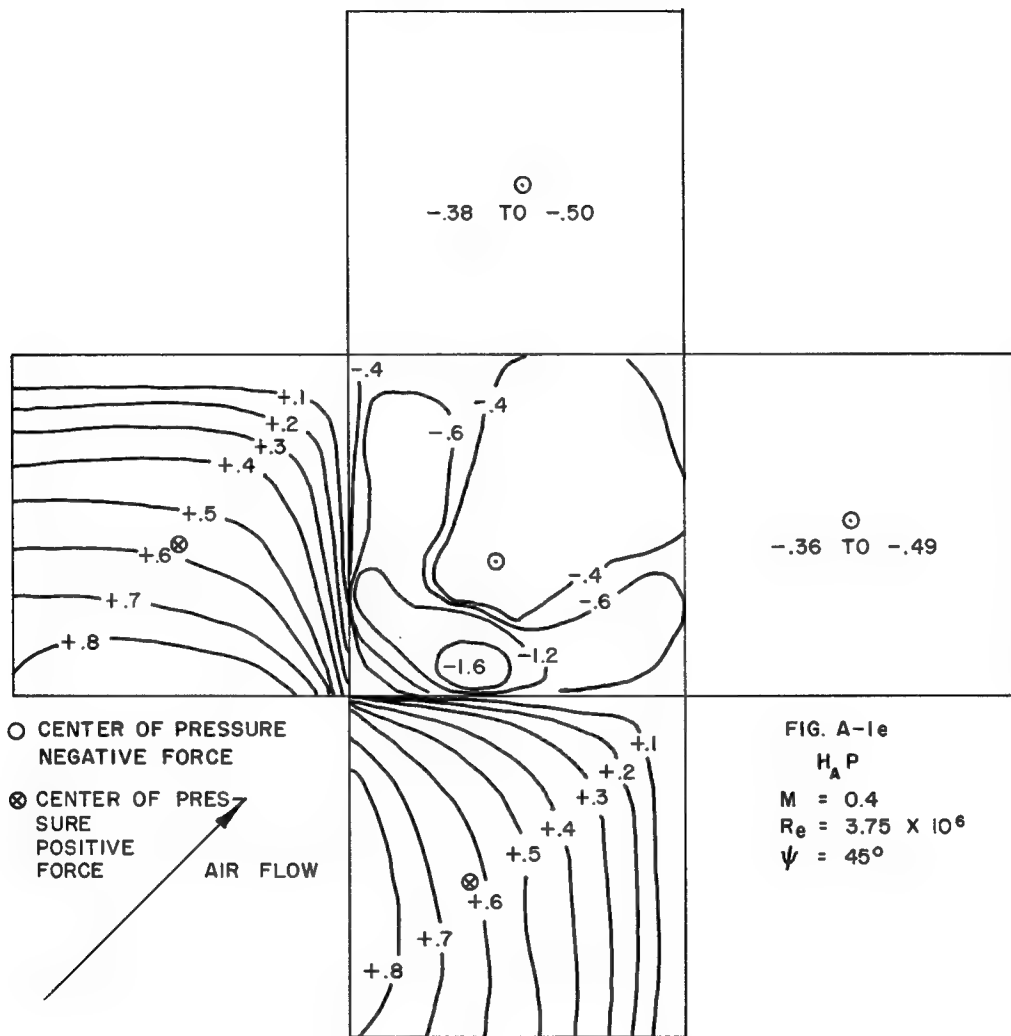


Fig. A. 1 (continued)

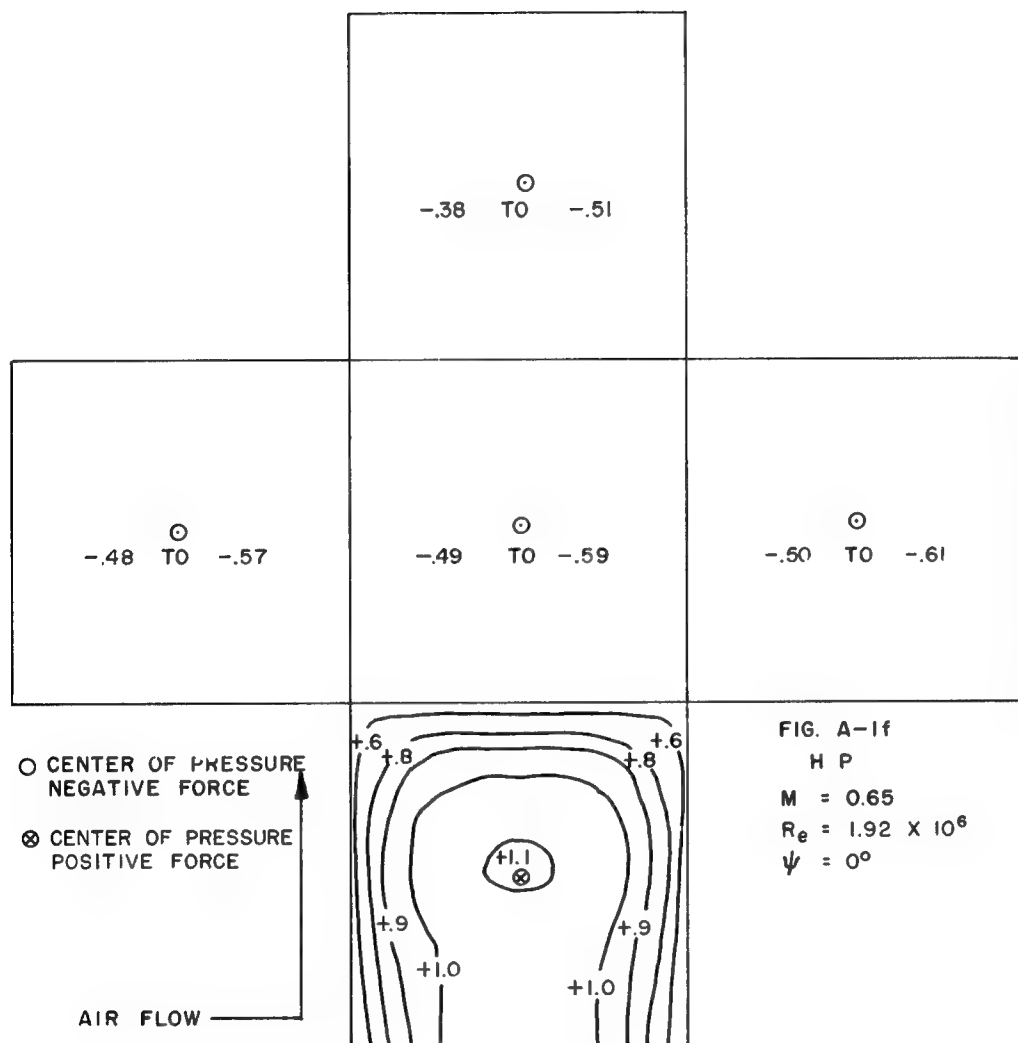


Fig. A. 1 (continued)

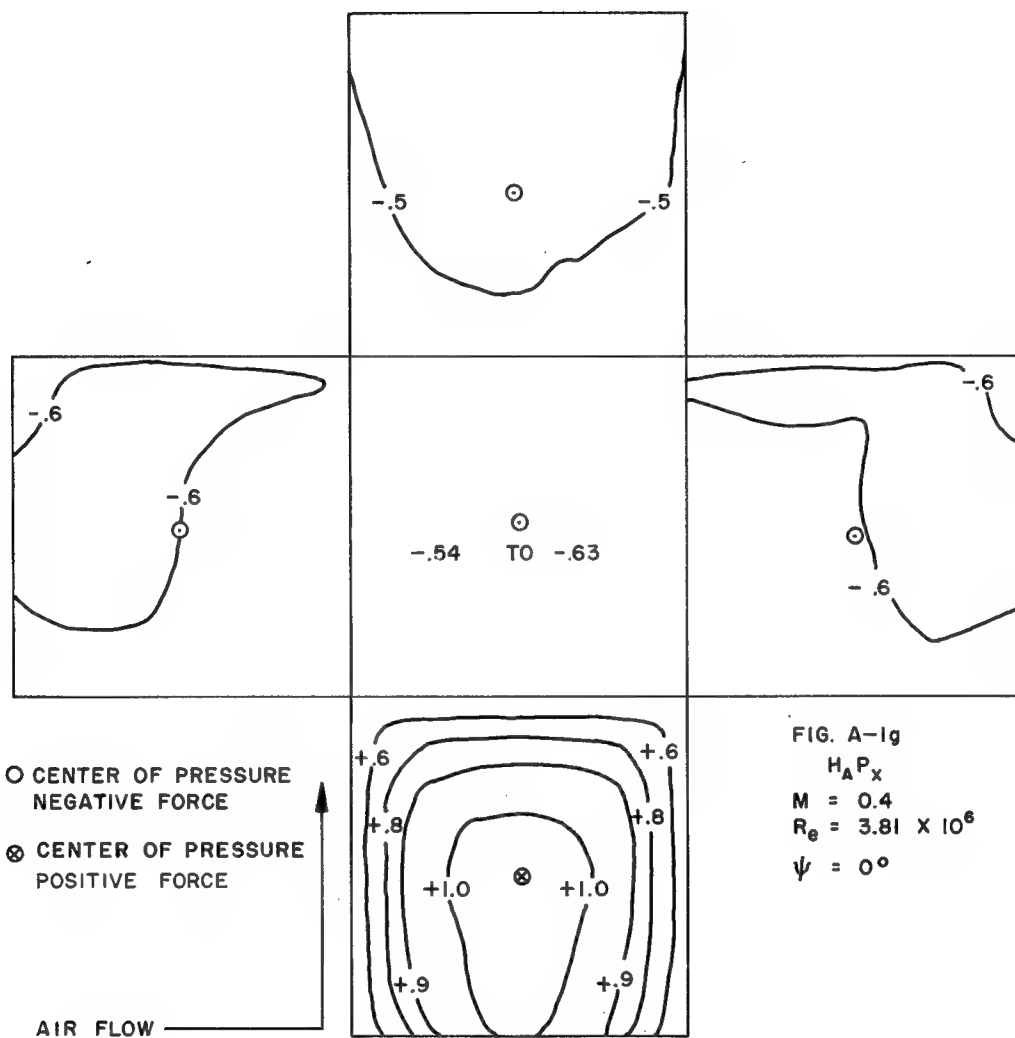


Fig. A. 1 (continued)



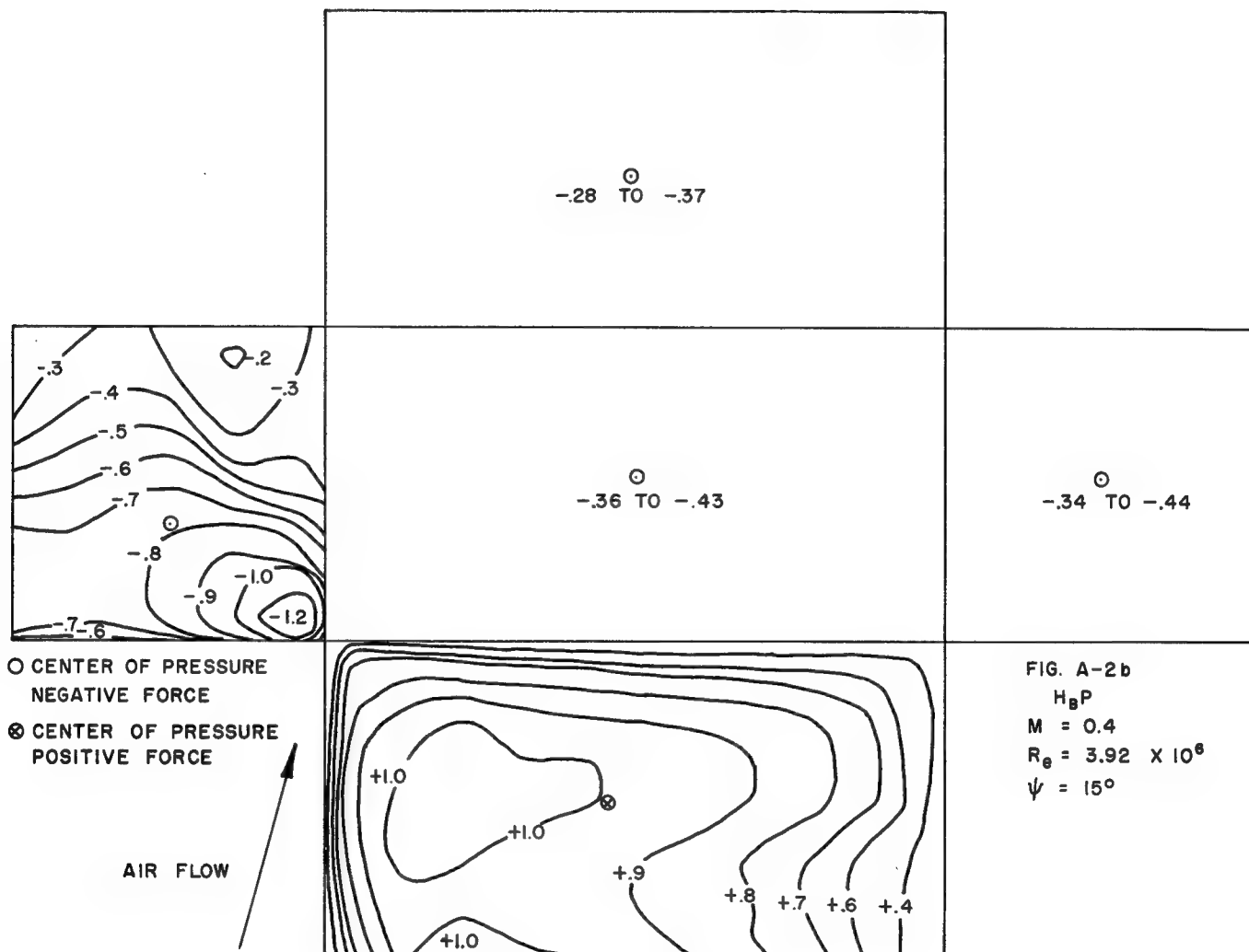


Fig. A.2 (continued)

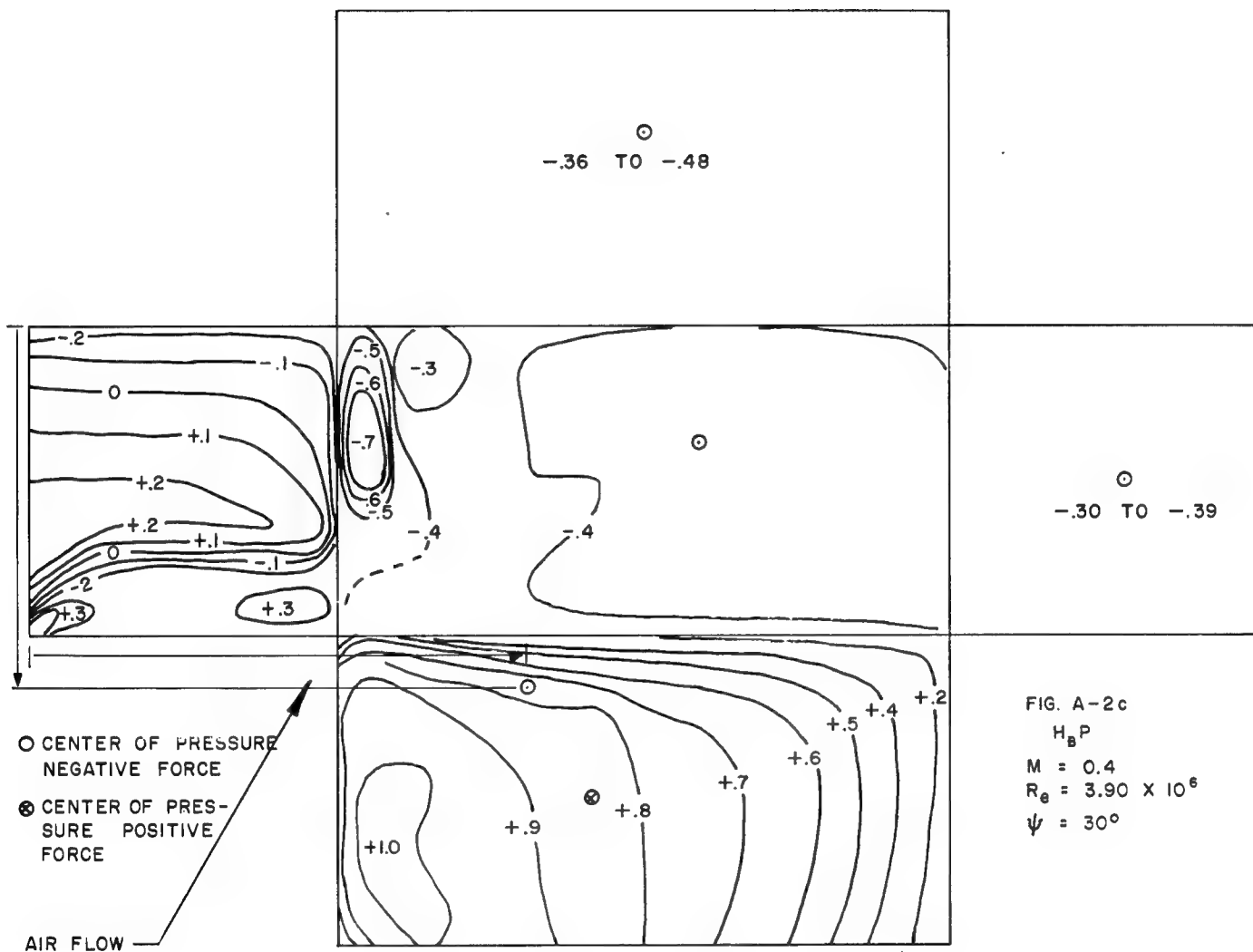


Fig. A.2 (continued)

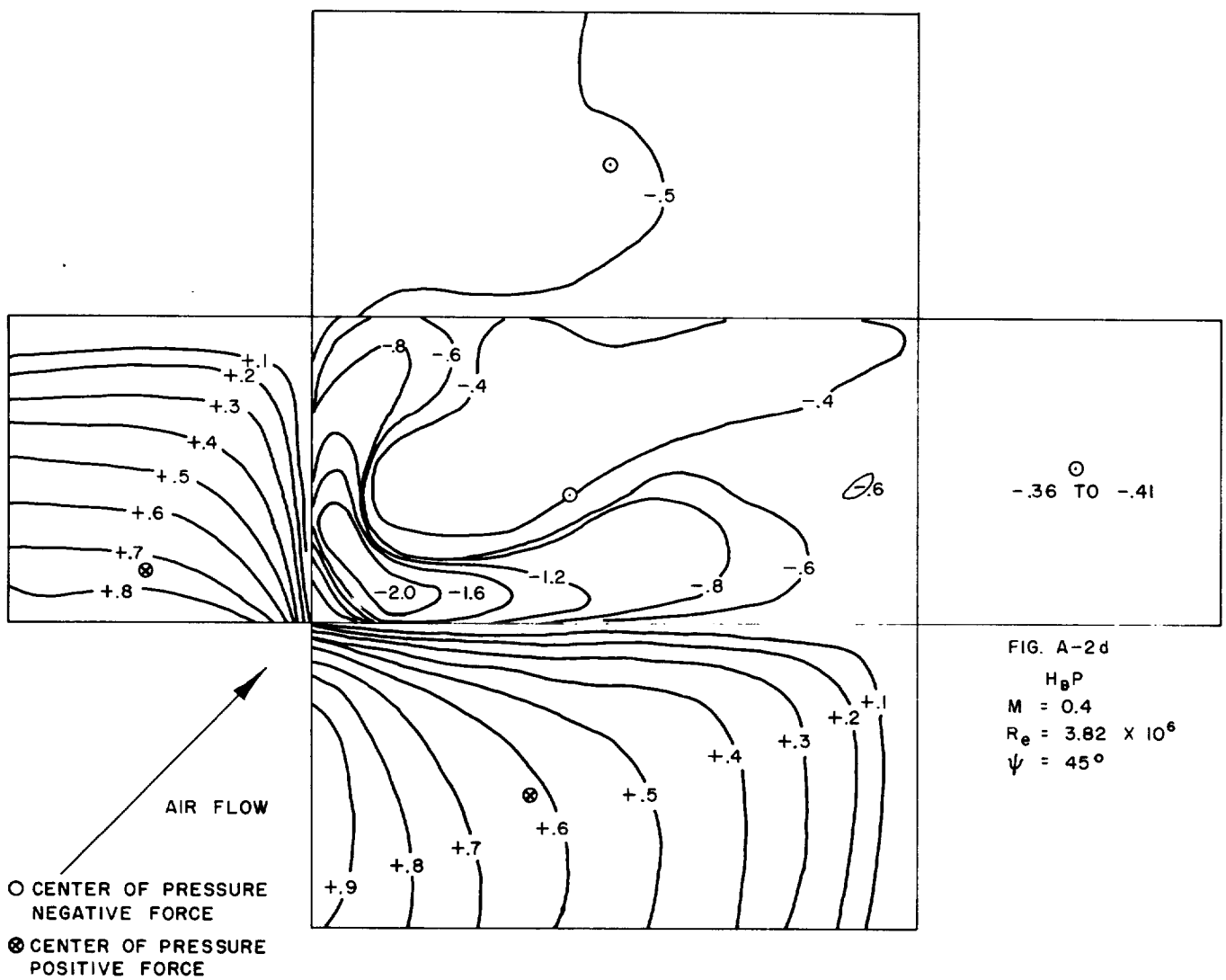


Fig. A.2 (continued)

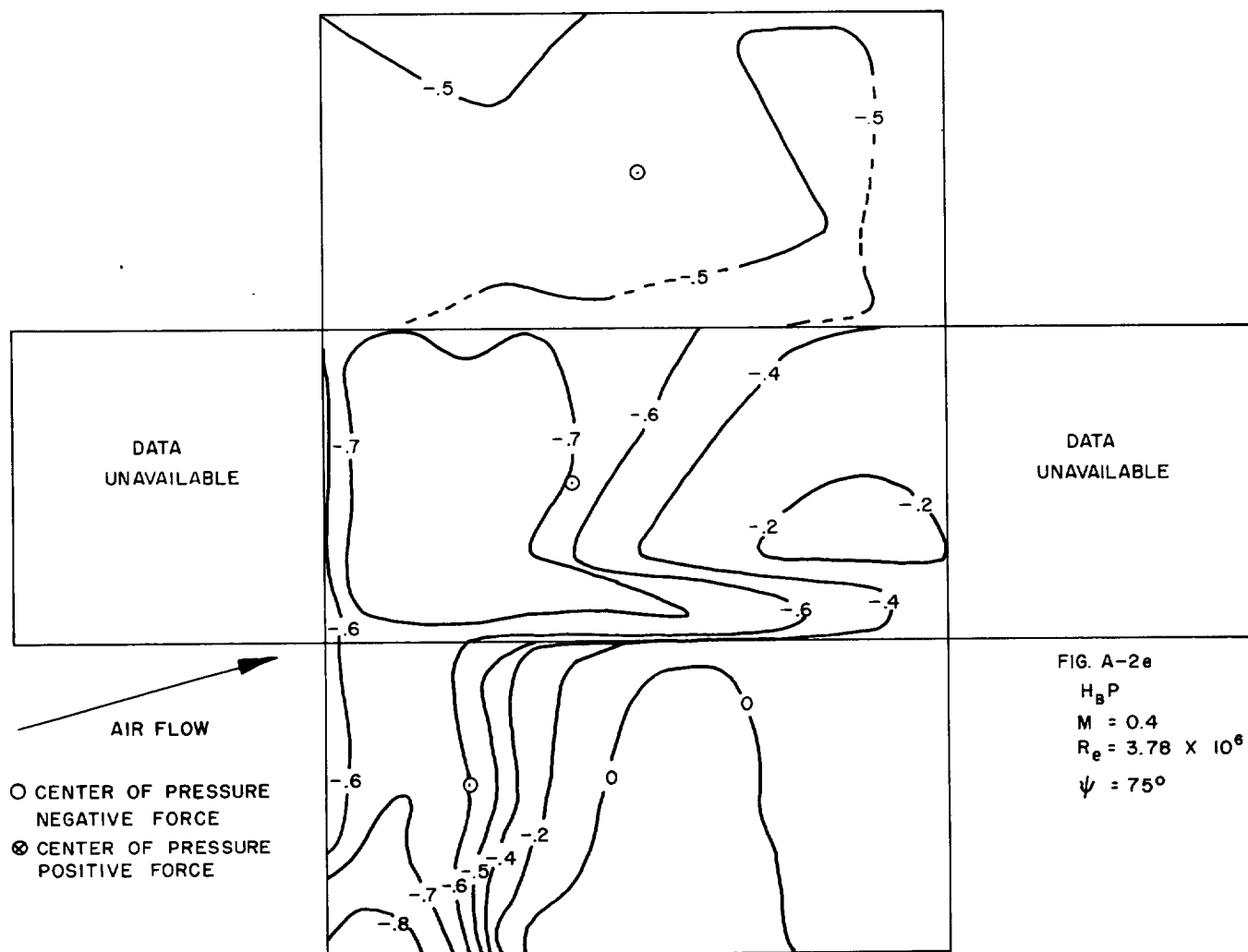


Fig. A.2 (continued)



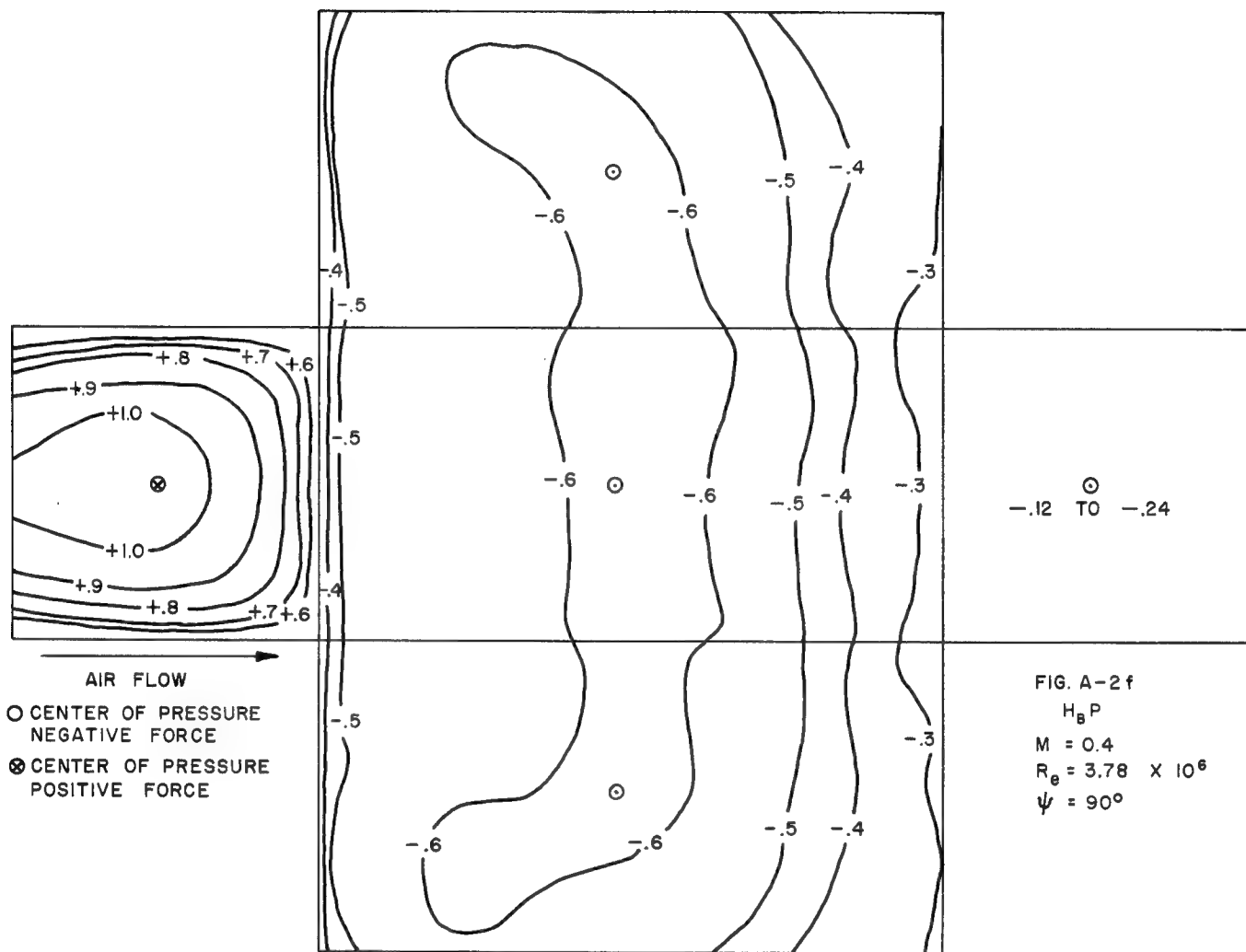


Fig. A.2 (continued)

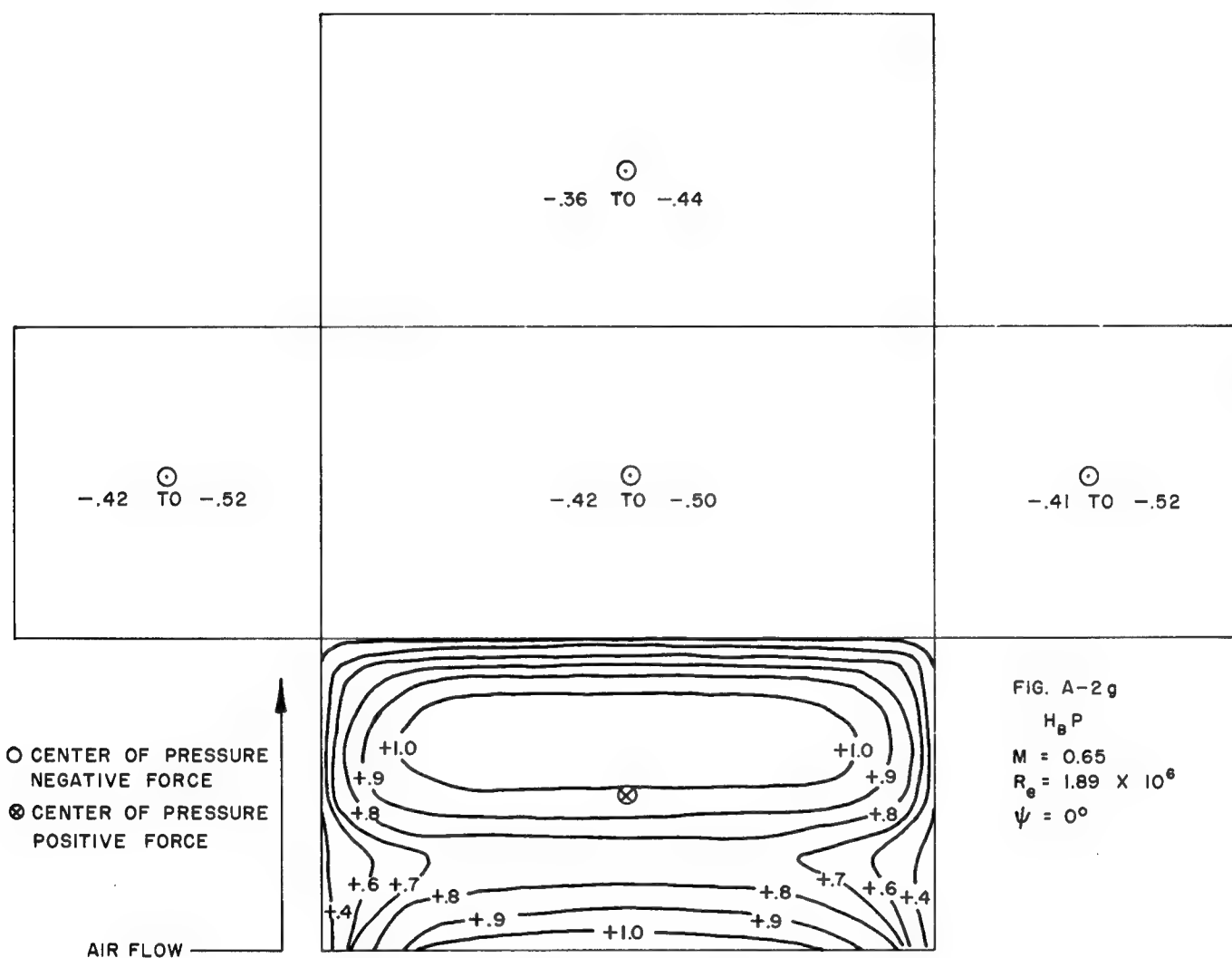


Fig. A. 2 (continued)

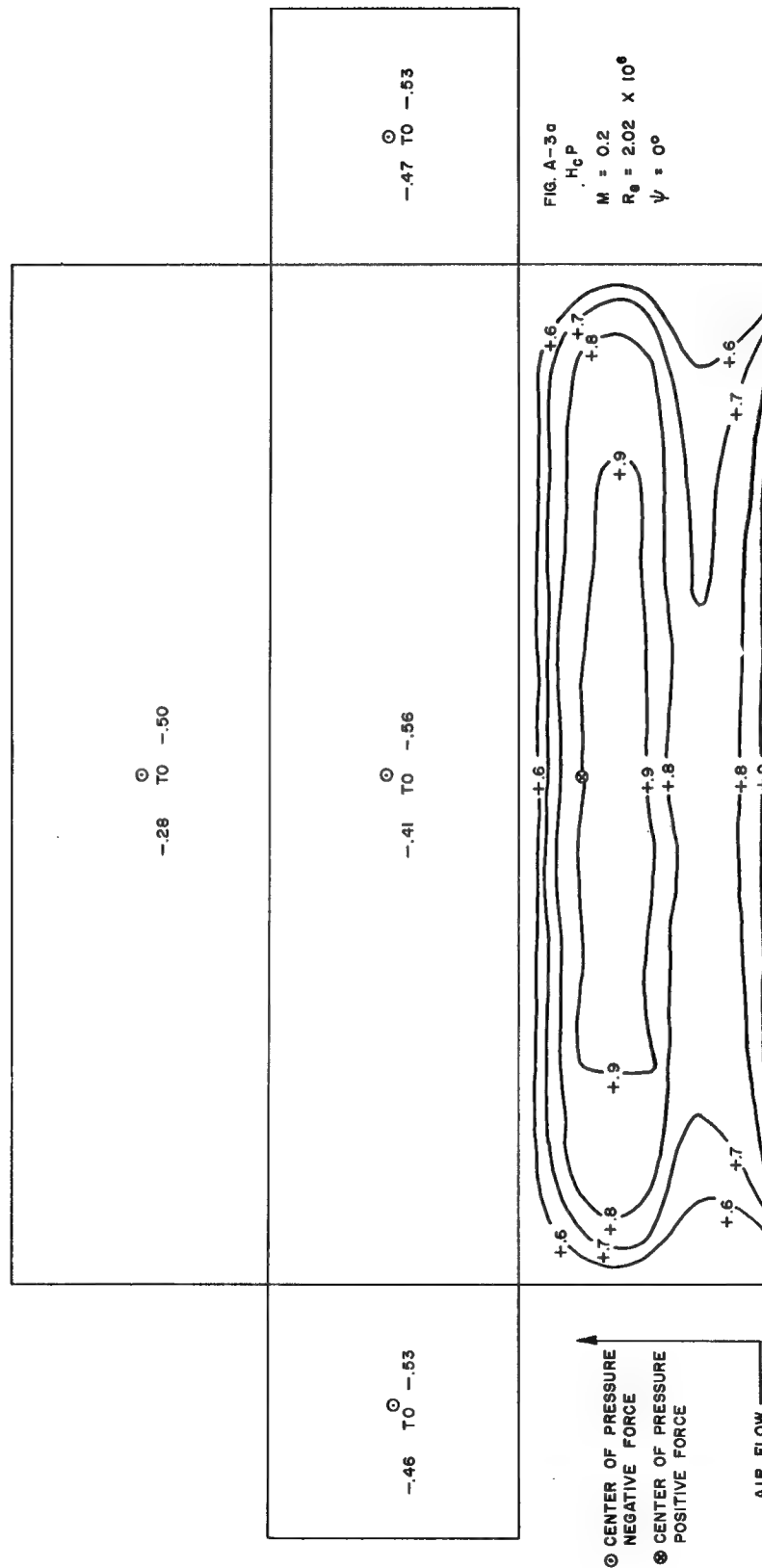


Fig. A.3 -- Pressure contours on 1:1:4 block form

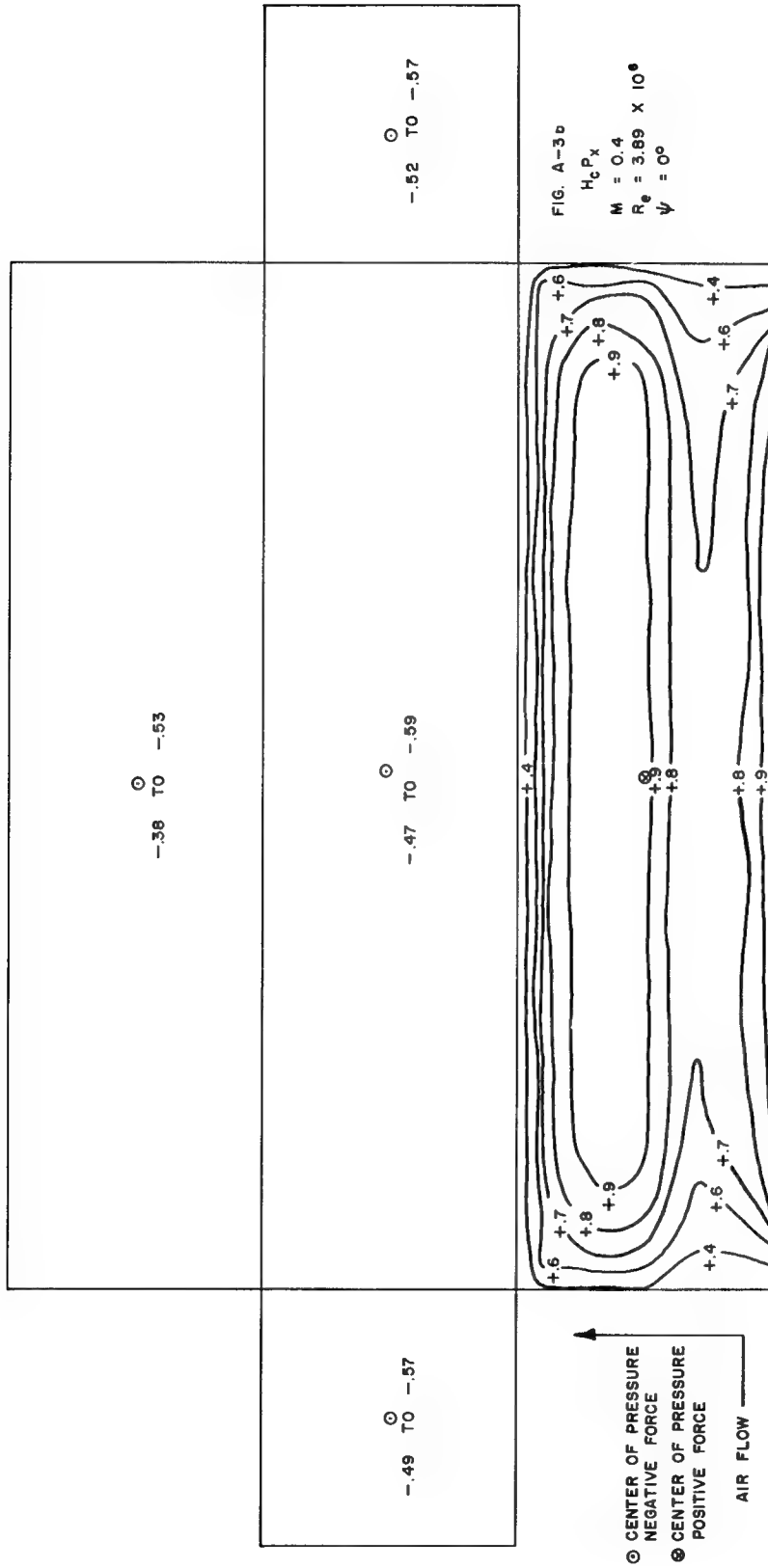


Fig. A.3 (continued)

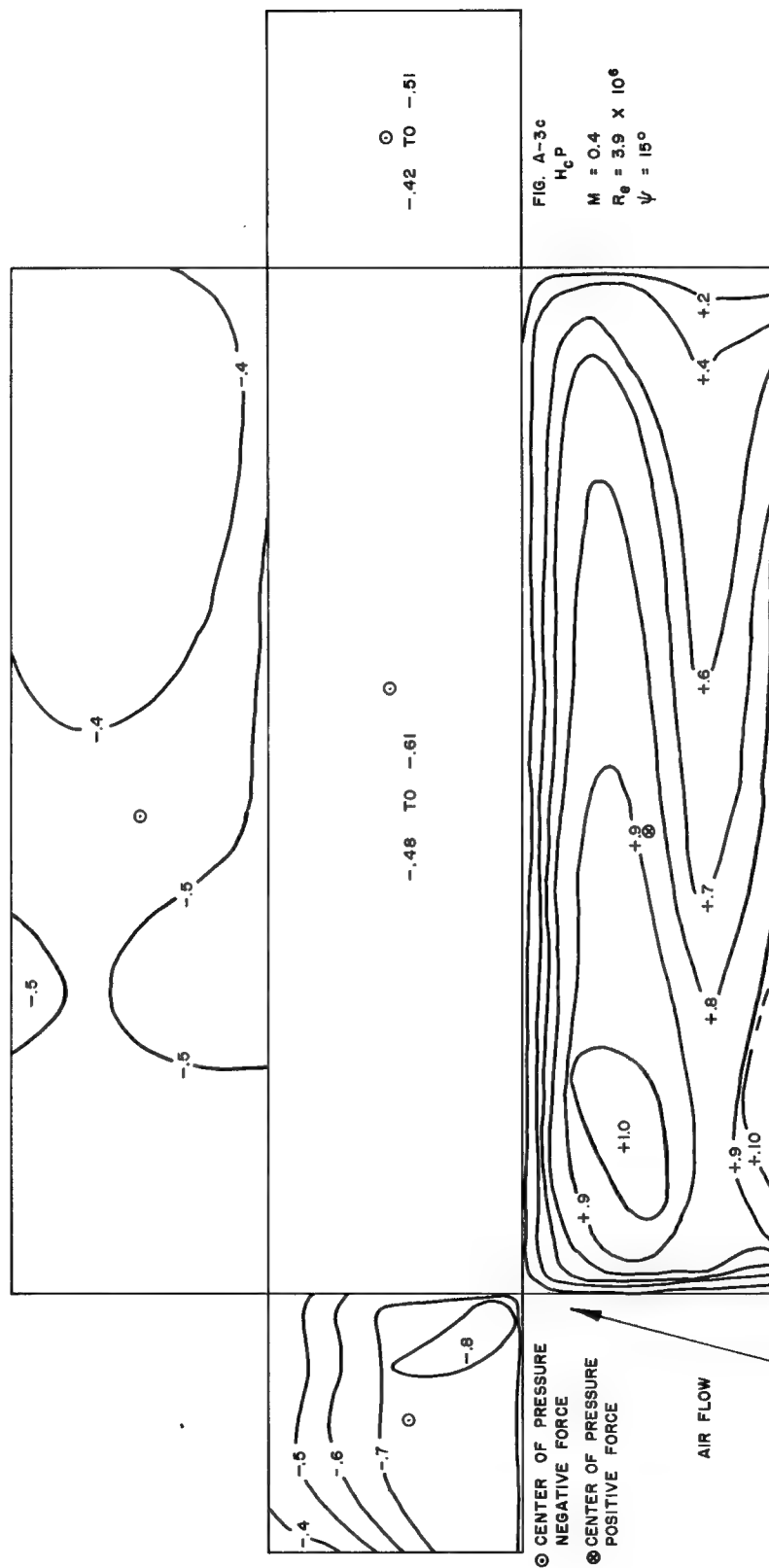


Fig. A. 3 (continued)





135



Fig. A. 3 (continued)





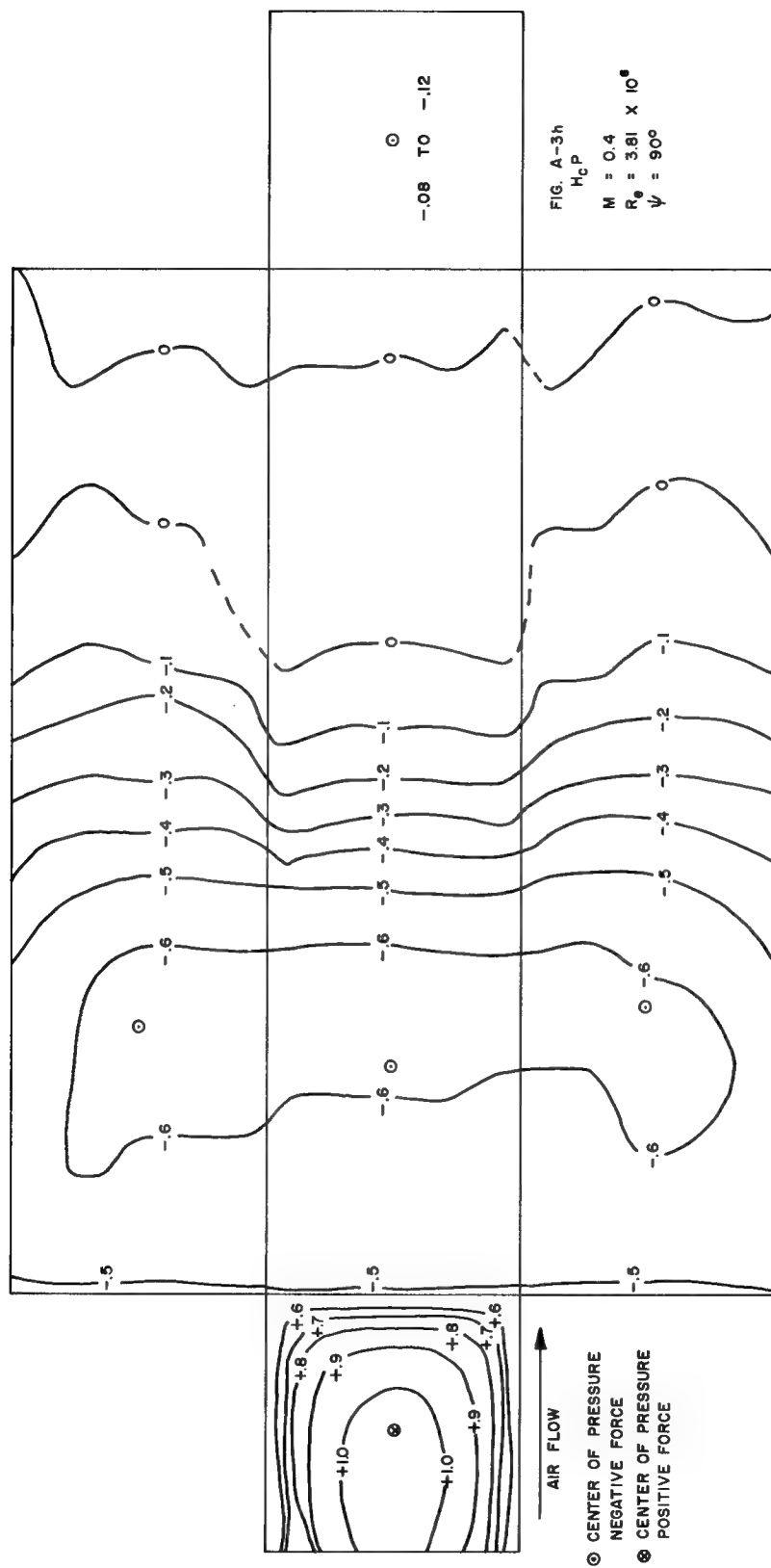


Fig. A. 3 (continued)

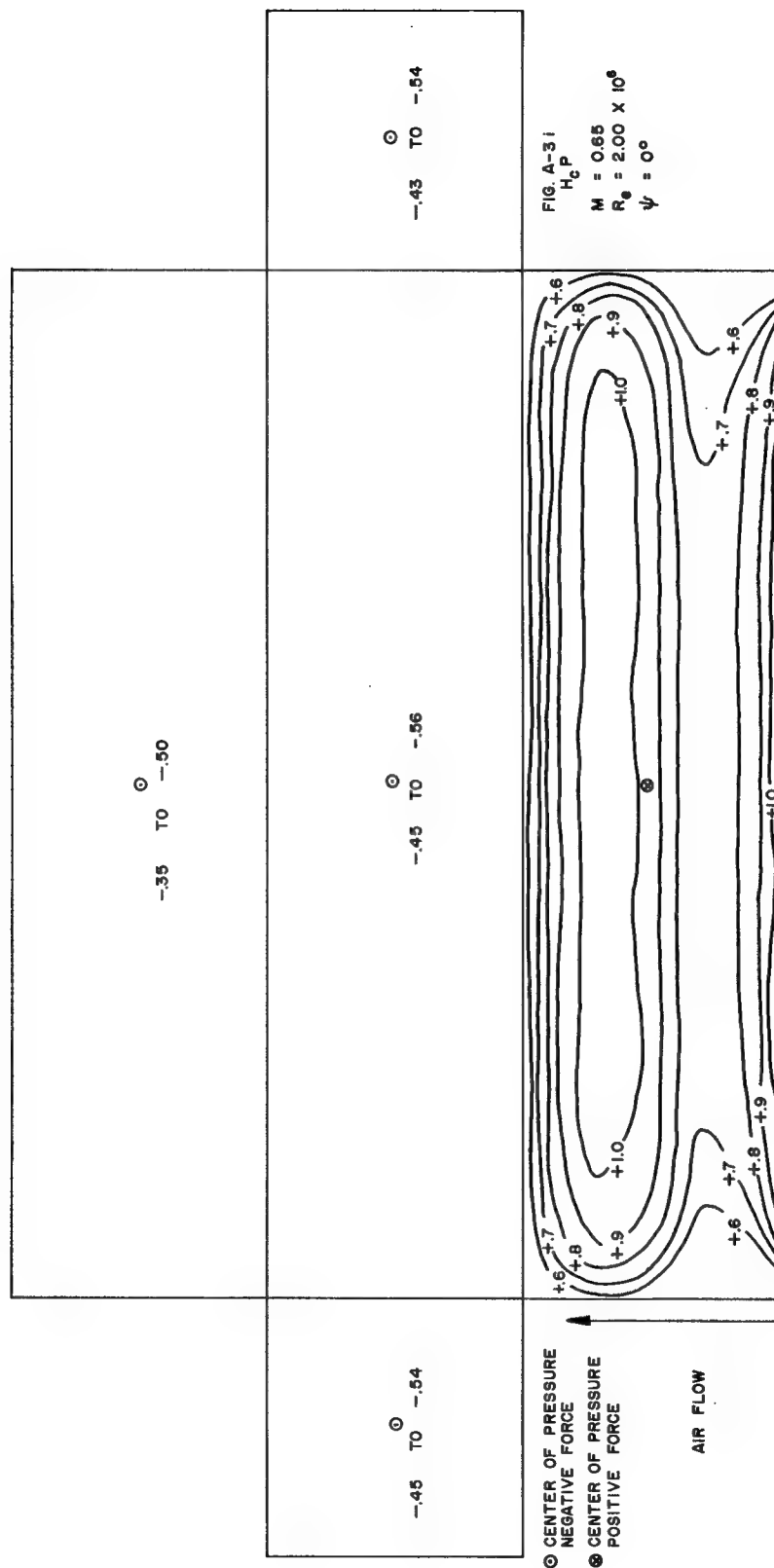


Fig. A. 3 (continued)

## INITIAL DISTRIBUTION

- 1 Walker Bleakney, Princeton University, Princeton, New Jersey
- 2 C. W. Lampson, BRL, Aberdeen, Maryland
- 3 G. K. Hartmann, NOL, White Oak, Silver Spring, Maryland
- 4 C. J. Aronson, NOL, White Oak, Silver Spring, Maryland
- 5 R. B. Vaile, Jr., Stanford Research Institute, Menlo Park, California
- 6 R. J. Hansen, MIT, Cambridge, Massachusetts
- 7 E. A. Witmer, MIT, Cambridge, Massachusetts
- 8 N. M. Newmark, University of Illinois, Urbana, Illinois
- 9 R. S. Stillwell, University of Illinois, Urbana, Illinois
- 10 J. S. McNown, University of Kansas, Lawrence, Kansas
- 11 B. G. Johnston, University of Michigan, Ann Arbor, Michigan
- 12 H. L. Bowman, Drexel Institute of Technology, Philadelphia, Pennsylvania
- 13 E. H. Smith, E. H. Smith Company, 901 Pershing Dr., Silver Spring, Maryland
- 14 UCRL, Livermore, Attn: Margaret Folden
- 15 P. Fine, DMA/AEC, Washington 25, D.C.
- 16 R. L. Corsbie, DBM/AEC, Washington 25, D.C.
- 17 C. Beck, Construction Division, USAEC, Washington 25, D.C.
- 18 R. W. Newman, J-6, LASL, Los Alamos, New Mexico
- 19 Thomas G. Morrison, American Machine and Foundry Company, Chicago 5, Illinois
- 20 Technical Information Service, USAEC, Attn: Jean M. O'Leary, Washington 25, D.C.
- 21 Director, National Bureau of Standards, Washington, D. C.
- 22 Dr. Merit P. White, Dept. of Engineering, University of Massachusetts, Amherst,  
Massachusetts
- 23 Professor Walter Vincenti, Stanford University, Palo Alto, California
- 24 Hunter Rouse, State University of Iowa, Iowa City, Iowa
- 25-28 Ira H. Abbott, National Advisory Committee for Aerodynamics, Washington, D.C.
- 29 Kenneth Razak, University of Wichita, Wichita, Kansas
- 30 Sherwood B. Smith, Holmes and Narver, Los Angeles 14, California
- 31 Theodore H. Schiffman, Armour Research Foundation, Chicago 16, Illinois
- 32-33 Eric Wang, WADC, Wright Patterson Air Force Base, Dayton Ohio, Attn: WCRN
- 34 Clayton S. White, Lovelace Foundation, Albuquerque, New Mexico
- 35 Benedict Cassen, University of California, Los Angeles Campus, School of Medicine,  
Atomic Energy Project, Los Angeles, California
- 36-40 AFSWP, Headquarters, Albuquerque, New Mexico
- 41-42 AFSWP/FC, Albuquerque, New Mexico
- 43 Paul Keller, Cooperative Wind Tunnel, Pasadena, California
- 44 Millard V. Barton, Ramo-Wooldridge, Los Angeles 45, California
- 45 B. L. Tucker, Rand Corporation, Santa Monica, California
- 46 Lydik S. Jacobsen, Stanford University, Palo Alto, California
- 47 J. P. Molnar, 1
- 48 G. A. Fowler, 5000

INITIAL DISTRIBUTION (cont)

49 C. F. Quate, 5100  
50 M. L. Merritt, 5110  
51-52 A. Y. Pope, 5140  
53-55 J. D. Shreve, 5112  
56 D. M. Hankins, 5112-1  
57 R. E. Dewhurst, 8233  
58 R. K. Smeltzer, 4721-3  
59 W. F. Carstens, 4723  
60-65 Document Room

Special Category - AERODYNAMICS TID-4500(14th Ed.)

3 Aberdeen Proving Ground  
1 ACF Industries, ERCO  
1 Aerojet-General Corporation  
1 Aerojet-General, San Ramon (I00-880)  
1 Air Force Ballistic Missile Division  
1 Air Force Cambridge Research Center  
1 Air Force Institute of Technology  
1 AFPR, Boeing, Seattle  
2 AFPR, Lockheed, Marietta  
1 AFPR, North American, Canoga Park  
2 Air Force Special Weapons Center  
1 Air Technical Intelligence Center  
1 Air University Library  
1 Albuquerque Operations Office  
1 ALCO Products, Inc.  
1 American University AT(40-1)-2387  
1 Armed Forces Special Weapons Project, Sandia  
1 Armed Forces Special Weapon Project, Washington  
5 Armed Services Technical Information Agency  
1 Army Ballistic Missile Agency  
1 Army Rocket and Guided Missile Agency  
1 Army Signal Research and Development Laboratory  
1 Assistant Secretary of the Air Force, Research and Development  
1 Atomic Bomb Casualty Commission  
1 AEC Scientific Representative, Argentina  
1 AEC Scientific Representative, France  
1 AEC Scientific Representative, Japan  
3 Atomic Energy Commission, Washington (TL)  
3 Atomics International  
4 Babcock and Wilcox Company (NYO-1940)  
2 Battelle Memorial Institute  
1 Bettis Plant  
1 Bureau of Aeronautics  
1 BAR, Aerojet-General, Azusa  
1 BAR, Goodyear Aircraft, Akron  
1 BAR, Grumman Aircraft, Bethpage  
1 Bureau of Ships (Code 1500)  
1 Bureau of Yards and Docks  
1 Carnegie Institute of Technology  
1 Chicago Operations Office  
1 Columbia University (SOO-187)  
1 Convair-General Dynamics Corporation, San Diego  
1 Cornell University (Wilson)  
1 Defence Research Member  
2 Department of the Army, G-2  
1 Dow Chemical Company (Rocky Flats)  
1 Du Pont Company, Wilmington  
1 Edgerton, Germeshausen and Grier, Inc., Boston

Special Category - AERODYNAMICS TID-4500(14th Ed.) (cont)

1	Edgerton, Germeshausen and Grier, Inc., Las Vegas
1	Frankford Arsenal
1	General Atomic Division
2	Goodyear Atomic Corporation
1	Jet Propulsion Laboratory
2	Los Alamos Scientific Laboratory
1	Lowry Air Force Base
1	Martin Company
1	Massachusetts Institute of Technology Hayden Library
1	Midwestern Universities Research Association
1	National Academy of Sciences
1	National Advisory Committee for Aeronautics, Cleveland
1	National Bureau of Standards (Library)
1	Naval Civil Engineering Research and Evaluation Laboratory
1	Naval Research Laboratory
1	New Brunswick Area Office
1	New York Operations Office
1	New York University (Richtmyer)
1	Oak Ridge Operations Office
1	Office of Atomic, Biological and Chemical Warfare
15	Office of Naval Research
1	Office of Naval Research (Code 422)
1	Office of Ordnance Research
1	Office of Quartermaster General
1	Office of Technical Services
1	Office of the Chief of Naval Operations
1	Ordnance Materials Research Office
1	Ordnance Tank-Automotive Command
1	Pennsylvania State University (Blanchard)
1	Picatinny Arsenal
3	Pratt and Whitney Aircraft Division
1	Princeton University (White)
1	Rensselaer Polytechnic Institute
1	San Francisco Operations Office
1	Stevens Institute of Technology
325	Technical Information Service Extension, Oak Ridge
1	USAF Project Rand
1	U.S. Naval Ordnance Laboratory
1	U.S. Naval Postgraduate School
1	U.S. Patent Office
4	University of California Radiation Laboratory, Livermore
1	University of Michigan
1	University of Rochester, Atomic Energy Project
2	University of Rochester (Marshak)
2	University of Washington (Geballe)
1	Watertown Arsenal
6	Wright Air Development Center
1	Yale University (Breit)